



UNIVERSITY OF  
LIVERPOOL

*Department of Engineering*

*PhD Thesis*

***Parallel diffractive multi-beam ultrafast laser  
micro-processing***

Thesis submitted in accordance with the requirements of The University of  
Liverpool for the degree of Doctor in Philosophy

By

***Zheng Kuang***

February 2010  
Laser Group  
Department of Engineering  
The University of Liverpool  
Brownlow Street  
Liverpool  
L69 3GH  
UK

## **Declaration**

I hereby declare that all of the work contained within this dissertation has not been submitted for any other qualification.

Signed:

Date:

## **Abstract**

During the last decade, ultrashort pulse lasers have been employed for high precision surface micro-structuring of materials such as metals, semi-conductors and dielectrics with little thermal damage. Due to the ultra high intensity of focussed femtosecond pulses ( $I > 10^{12} \text{W/cm}^2$ ), nonlinear absorption can be induced at the focus leading to highly localised material ablation or modification. This is now opening up applications ranging from integrated optics, through multi-photon induced refractive index engineering to precision surface modification for silicon scribing and solar cell fabrication.

To ensure non thermal material processing, the input fluence ( $F$ ) of the ultrashort pulse laser must be kept in the low regime ( $F \sim 1 \text{Jcm}^{-2}$ ), a few times above the well defined ablation threshold. Accordingly,  $\mu\text{J}$  ( $10^{-6} \text{J}$ ) level pulse energy input is often required for ultrashort pulse laser fine micro/nano-surface structuring. Running at one kilohertz repetition rate, many current ultrashort pulse laser systems can provide mJ ( $10^{-3} \text{J}$ ) level output pulse energy. Accordingly, significant attenuation of the laser output is required for many applications and hence causes a great deal of energy loss.

With this limitation in mind, holographic multiple beam ultrashort pulse laser processing, where the mJ pulse energy is split into many desired diffracted beams with arbitrary geometric arrangement, is proposed in this thesis. The multi-beam patterns are generated by phase modulation using computer generated holograms (CGHs) which are displayed on a Spatial Light Modulator (SLM). The ability to address these devices in real time and synchronize with scanning methods adds an additional flexibility to the processing. The results obtained in this thesis demonstrate high precision micro-fabrication of different kinds of materials with greatly increased processing efficiency and throughput, showing many potential industrial applications.

## List of Publications to Date by Author

### Peer-Reviewed Journal Publications:

Zheng Kuang, Walter Perrie, Dun Liu, S. P. Edwardson, Geoff Dearden, and K. G. Watkins, “*Uniformity study of diffractive multi-beam pattern applied for parallel ultrafast laser micro-structuring*” manuscript under preparation - **First and corresponding author**

Zheng Kuang, Dun Liu, Walter Perrie, Jian Cheng, Shuo Shang, S. P. Edwardson, E. Fearon, G. Dearden, K. G. Watkins, “*Diffractive Multi-beam Ultra-fast Laser Micro-processing Using a Spatial Light Modulator(Invited paper)*”, Chinese Journal of Lasers, Vol. 36, No. 12, pp. 3093 – 3115, (2009) - **First author**

Zheng Kuang, Walter Perrie, Dun Liu, Stuart Edwardson, Jian Cheng, Geoff Dearden and Ken G. Watkins “*Diffractive multi-beam surface micro-processing using 10 ps laser pulses*”, Applied Surface Science, Vol. 255, Issue 22, pp. 9040 – 9044 (2009) – **First and corresponding author**

Zheng Kuang, Dun Liu, Walter Perrie, Stuart Edwardson, Martin Sharp, Eamonn Fearon, Geoff Dearden and Ken G. Watkins, “*Fast parallel diffractive multi-beam femtosecond laser surface micro-structuring*” Applied Surface Science, Vol. 255, Issues 13-14, pp. 6582-6588, (2009) – **First and corresponding author**

Zheng Kuang, Walter Perrie, Jonathan Leach, Martin Sharp, Stuart P. Edwardson, Miles Padgett, Geoff Dearden and Ken. G. Watkins, “*High throughput diffractive multi-beam femtosecond laser processing using a spatial light modulator*”, Applied Surface Science, Volume 255, Issue 5, pp. 2284-2289, (2008) – **First and corresponding author**

**Conference Publications:**

Z. Kuang, D. Liu, W. Perrie, J. Cheng, S. P. Edwardson, G. Dearden, and K. G. Watkins, “*Fast parallel diffractive multi-beam laser surface micro-structuring*” Paper No: 1782 – 36<sup>th</sup> MATADOR Conference – **First author**

Z. Kuang, D. Liu, W. Perrie, J. Cheng, S. Shang, S. P. Edwardson, E. Fearon, G. Dearden, and K. G. Watkins, “*Multiple beam ultrafast laser microprocessing (Invited paper)*”, PICALO Congress Proceedings (M103), March 23 – 25, 2010 - **First author**

D. Liu, Z. Kuang, S. Shang, W. Perrie, D. Karnakis, A. Kearsley, M. Knowles, S. Edwardson, G. Dearden and K. G. Watkins, “*Ultrafast parallel laser processing of materials for high throughput manufacturing*” Proceeding of LAMP 2009 – The 5th International Congress on Laser Advanced Materials Processing – **Co-author**

Z. Kuang, W. Perrie, M. Sharp, S. P. Edwardson, G. Dearden and K. G. Watkins, “*Diffractive Multi-Beam Ultra Fast Laser Processing by Using a Spatial Light Modulator*”, IOP Photon08 Conference, 26-29 August 2008 – **First author/Presenter**

D. Liu, J. Cheng, W. Perrie, A. Baum, P. Scully, M. Sharp, S. P. Edwardson, Z. Kuang, N. G. Semaltianos, P. French, G. Dearden, L. Li, K. G. Watkins, “*Femtosecond Laser Micro-structuring of Material in the Nir and UV Regime*” ICALEO® 2007 Congress Proceedings, Laser Microprocessing Conference Paper M103 pp.12-18 - **Co-author**

## **Acknowledgements**

First of all, I hereby sincerely acknowledge my supervisors, Professor Ken Watkins and Dr Geoff Dearden at the Laser Group of the University of Liverpool, who offered support, guidance and encouragement throughout this research. Without their kind and solid dedication, this paper would not have been possible. I also owe much to Dr Walter Perrie, a senior researcher at our Laser Group, whose insights into ultrashort pulse laser material processing have helped me to accomplish this thesis successfully.

At the same time, I am also thankful for the professional instruction and effective assistance from other members in our research group: Dr Stuart Edwardson, Dr Martin Sharpe and Dr Eamonn Fearon, and appreciate all the kind help from my fellow students: Leigh Mellor, Olivier Allegre, Dun Liu, Jian Cheng and Spencer Shang, who always show me a good sample of working under any hard situation.

I also gratefully acknowledge Prof. Miles Padgett and Dr. Jonathan Leach at University of Glasgow for giving kind help on the hologram calculation used for this research.

Additionally, I would like to thank the Scholarship of Overseas Research Students Award Scheme (ORSAS) and the Scholarship of University of Liverpool Graduate Association (Hong Kong) for providing financial support for my PhD study at the University of Liverpool.

Last but not least, my love and thanks go to my beloved family, to my affectionate and brave father and mother, who, old and lonely as they are, have firmly supported me financially and always shown me the right way to go when I lose direction; to my beloved wife, Ying Ma, for all the pleasure and happiness she shared with me during my time in the UK.

# Table of Contents

Abstract	III
List of Publications to Date by Author	IV
Acknowledgements	VI
Table of Contents	VII
List of Figures	XII
List of Tables	XXII
List of Symbols	XXIII
List of Abbreviations	XXV

## **Chapter 1 – Introduction**

1.1 Background to research area .....	2
1.2 Motivation.....	3
1.3 Overview of the thesis .....	5

## **Chapter 2 – Literature Review**

2.1 Introduction.....	8
2.2 Ultrashort pulse laser systems and ultrashort pulse laser material processing .....	8
2.2.1 Ultrashort pulse laser systems .....	8
2.2.1.1 Emission spectrum of the active medium.....	8
2.2.1.2 Chirped pulse amplification (CPA).....	9
2.2.1.3 Simple and compact picosecond laser system.....	13
2.2.2 Ultrashort pulse laser ablation of material .....	15
2.2.2.1 Absorption of laser energy .....	16
2.2.2.2 Well defined ablation threshold with ultrashort pulses.....	17
2.2.2.3 ‘Thermal-free’ processing with ultrashort laser pulses.....	19

2.2.2.4 Material processing with picosecond laser pulses .....	22
2.2.3 The limitations of ultrashort pulse laser processing .....	25
2.3 Multiple beam parallel processing .....	27
2.3.1 Parallel microfabrication of periodic structures .....	28
2.3.2 Parallel microfabrication of arbitrary structures.....	32
2.4 The generation of multiple beams using a spatial light modulator (SLM).....	34
2.4.1 Introduction to SLM technology .....	34
2.4.2 Generation of multiple beams with an SLM .....	39
2.5 The calculation of Computer Generated Hologram (CGH) algorithms .....	41
2.5.1 CGH calculation algorithms summary.....	41
2.5.1.1. Algorithms for calculating Fourier Plane Holograms.....	41
2.5.1.2. Multiplexing Phase Fresnel Lenses (MPFL) algorithm for calculating Fresnel Plane Holograms .....	49
2.5.2 Calculation of CGHs with a LabVIEW program .....	52
2.6 Summary .....	54

### **Chapter 3 – Experimental Equipment and Techniques**

3.1 Introduction.....	57
3.2 Principal experimental apparatus used for the research .....	57
3.2.1 Ultrashort pulse laser systems .....	57
3.2.1.1 Clarke-MXR CPA2010 femtosecond laser system.....	57
3.2.1.2 High-Q picoseconds laser system.....	60
3.2.2 Spatial Light Modulators (SLM) .....	62
3.2.2.1 Boardband coated SLM – Holoeye.....	62
3.2.2.2 Dielectric coated SLM – Hamamatsu .....	63
3.2.2.3 High power tests on Spatial Light Modulators (SLM).....	64
3.2.3 Scanning galvanometer systems and multi-axis motion control systems.....	69
3.2.3.1 Scanning galvanometer systems .....	69
3.2.3.2 Multi-axis motion control system (Aerotech) .....	71
3.3 Methods to remove the zero order beam .....	72
3.3.1 Removal of the zero order beam with a 4f-imaging optical system.....	73
3.3.1.1 Zero order beam removed with 4f system.....	73

3.3.1.2 Modelling the 4f-imaging optical system with ZEMAX .....	75
3.3.2 Removal of the zero order beam by adding a Fresnel zone lens .....	78
3.3.2.1 Defocusing of the zero order beam at processing plane .....	78
3.3.2.2 Combination of the Fourier and Fresnel plane hologram .....	82
3.4 Experimental setup .....	82
3.4.1 Experimental setup without the 4f optical system.....	83
3.4.2 Experimental setup with 4f optical system .....	84
3.5 Summary .....	86

## **Chapter 4 - Diffractive multi-beam microprocessing using femtosecond laser pulses**

4.1 Introduction.....	88
4.2 Static CGH multiple laser beam micro-processing .....	88
4.2.1 Precision micro-drilling using diffractive $\mu\text{J}$ -level multiple beams .....	88
4.2.2 The distortion of beam shape caused by finite spectral bandwidth.....	94
4.2.2.1 The observation of distorted beam shape .....	94
4.2.2.2 Prediction of the eccentricity of beam shape by calculation .....	97
4.2.2.3 Effect of beam shape distortion on process stability.....	98
4.3 Laser microprocessing with dynamic diffracted beam patterns.....	99
4.3.1 Response time of the SLM .....	99
4.3.2 Micro-processing by real time playing CGHs.....	102
4.3.3 Synchronizing the action of hologram application with scanning techniques .....	105
4.4 Summary .....	107

## **Chapter 5 - Diffractive multiple beam microprocessing using picosecond laser pulses**

5.1 Introduction.....	109
-----------------------	-----

5.2 Experimental setup.....	109
5.3 Spectral bandwidth effect on diffracted beam shape.....	110
5.4 High power parallel processing with high repetition rate at $f = 20\text{kHz}$ .....	113
5.5 Summary.....	114

## **Chapter 6 - Uniformity study of diffractive laser beam patterns**

6.1 Introduction.....	117
6.2 Methodology of the uniformity study.....	118
6.2.1 Geometric design of the diffractive pattern .....	118
6.2.2 The uniformity measurement .....	119
6.3 Results of uniformity study.....	120
6.3.1 Diffraction efficiency and uniformity resulting from the geometric pattern design.....	120
6.3.2 Generating symmetric patterns by combination of several asymmetric pattern with good uniformity.....	123
6.4 Discussion.....	126
6.4.1 The degeneracy of the design pattern .....	126
6.4.2 Degeneracy avoided by adding a random phase .....	127
6.5 Summary.....	128

## **Chapter 7 - Investigations into potential applications of diffractive multiple beam laser microprocessing**

7.1 Introduction.....	130
7.2 High throughput surface micro-structuring of silicon.....	130
7.2.1 Diffractive multi-beam pattern design.....	131
7.2.2 Results of micro-structuring of silicon using the diffractive patterns .....	132
7.3 Laser patterning of organic light emitting diode (OLED) materials.....	134
7.3.1 Diffractive multi-beam patterning of cathode layers.....	135
7.3.2 Diffractive multi-beam patterning of Anode (ITO).....	136

7.4 Selective ablation of surface material (silicon wafer) by diffractive multi-beams .....	137
7.4.1 Selective ablation by modulating the focal height.....	137
7.4.2 Multi-beam scanning with different number of spots per line .....	140
7.5 Diffractive multi-beam internal structuring of volume gratings .....	141
7.5 Summary .....	144

## **Chapter 8 - Conclusions and recommendation for future work**

8.1 Conclusions.....	146
8.2 Recommendation for Future Work.....	148

<b>References .....</b>	<b>151</b>
-------------------------	------------

<b>Appendices (Selected publications) .....</b>	<b>169</b>
---	------------

# List of Figures

<u>Figure no.</u>	<u>Figure caption</u>	<u>Page</u>
<b>Fig. 1.1:</b>	<i>The craters generated by single ultrashort pulses (<math>\tau_p \sim 160\text{fs}</math>) on a sample of silicon wafer. The pulse energy was <math>\sim 0.3\text{mJ}</math> in (a), and <math>\sim 2\mu\text{J}</math> in (b). Surface melting is observed in (a), while the results in (b) shows a perfectly clean surface with much less thermal effects.</i>	<b>3</b>
<b>Fig. 1.2:</b>	<i>Split mJ level input single beam into many <math>\mu\text{J}</math> level diffracted beams for thermal-free precision ultrashort pulse laser micro-processing.</i>	<b>4</b>
<b>Fig. 2.2.1:</b>	<i>The principle of chirped-pulse amplification for high-power ultrashort pulse generation. The pulse duration manipulation is to overcome damage of optical materials by high-power laser pulses in the amplifier.</i>	<b>10</b>
<b>Fig. 2.2.2:</b>	<i>Grating-pair pulse stretcher (a) and compressor (b). The gratings in the stretcher are antiparallel and are parallel in the compressor.</i>	<b>11</b>
<b>Fig. 2.2.3:</b>	<i>Diagramatic scheme of chirped pulse amplification.</i>	<b>12</b>
<b>Fig. 2.2.4:</b>	<i>Schematic of the picosecond Nd:YVO<sub>4</sub> oscillator amplifier system.</i>	<b>14</b>
<b>Fig. 2.2.5:</b>	<i>Absorption of laser energy.</i>	<b>16</b>
<b>Fig. 2.2.6:</b>	<i>Single-shot plasma emission data of laser-induced breakdown in fused silica as function of incident laser fluence for laser pulse durations of (a) 7 ns and (b) 170 fs.</i>	<b>18</b>
<b>Fig. 2.2.7:</b>	<i>Long pulse induced material ablation.</i>	<b>20</b>
<b>Fig. 2.2.8:</b>	<i>Ultrashort pulse induced material ablation.</i>	<b>21</b>
<b>Fig. 2.2.9 (a):</b>	<i>Cross section profiles (left) and 3-D images (right) of single-pulse drilling of Au sample using a 10ps laser at a wavelength of 1064 nm under varied laser fluence under varied laser fluence: (a) <math>F = 1 \text{ J cm}^2</math>, (b) <math>F = 5 \text{ J cm}^2</math>, (c) <math>F = 20 \text{ J cm}^2</math>.</i>	<b>23</b>

<b>Fig. 2.2.9 (b):</b>	<i>Cross section profiles (left) and 3-D images (right) of single-pulse drilling of Au sample by using a 180 fs laser at a wavelength of 775 nm under varied laser fluence: (a) <math>F = 1 \text{ J cm}^{-2}</math>, (b) <math>F = 5 \text{ J cm}^{-2}</math>, (c) <math>F = 10 \text{ J cm}^{-2}</math>.</i>	<b>24</b>
<b>Fig. 2.2.10:</b>	<i>Single shot femtosecond ablation of polished aluminium, where <math>F \approx 14 \text{ J/cm}^2</math> (a), <math>F \approx 14 \text{ J/cm}^2</math> (b).</i>	<b>26</b>
<b>Fig. 2.3.1:</b>	<i>Experimental design of material parallel processing using the method of multi-beam interference.</i>	<b>28</b>
<b>Fig. 2.3.2:</b>	<i>Calculated intensity profiles of 2D periodic patterns.</i>	<b>29</b>
<b>Fig. 2.3.3:</b>	<i>Scanning electron microscopy (SEM) images of the structure fabricated by the multi-beam interference of ultrashort pulses. (a) Top view, (b) oblique view of the same sample, and (c) oblique view of another sample fabricated at larger exposure energy.</i>	<b>30</b>
<b>Fig. 2.3.4:</b>	<i>Basic scheme of optical setup. MLA: microlens array, LI: lens, DM: dichroic mirror, OL: objective lens. A is the plane where multiple foci are generated</i>	<b>31</b>
<b>Fig. 2.3.5:</b>	<i>An optical micrograph of the fabricated structure by MLA laser processing.</i>	<b>31</b>
<b>Fig. 2.3.6:</b>	<i>The results showing the microstructuring using a DOE generated arbitrary multi-beam pattern. (a) The designed focal shape of the pattern, (b) The modulated beam profile, (c) Surface view of ablation pattern observed by optical microscopy, (d) Processed area inside the glass observed by optical microscopy, left: top view, right: side view.</i>	<b>32</b>
<b>Fig. 2.3.7:</b>	<i>Experimental setup of the holographic femtosecond laser processing system.</i>	<b>33</b>
<b>Fig. 2.3.8:</b>	<i>(a) A target pattern for calculating a CGH, (b) the calculated CGH, (c) the computational reconstruction of the CGH, (d) the optical reconstruction of the CGH at the plane P, (e) a transmission microscope image, and (f) an Atomic Force Microscopy (AFM) image of the fabricated</i>	<b>34</b>

area. The vertical scale of the AFM profile is  $\pm 500$  nm.

<b>Fig. 2.4.1:</b>	<i>The sketches demonstrate different types of SLM, reflective (a) &amp; transmissive (b), and how they work.</i>	<b>35</b>
<b>Fig.2.4.2:</b>	<i>The basic structure of LCD.</i>	<b>36</b>
<b>Fig. 2.4.3:</b>	<i>The measured results from a Holoeye LC-R 2500 SLM with <math>\lambda = 632.8\text{nm}</math> linearly polarized laser input, showing a near linear increase of the phase modulation with increasing the grey level (from 0 to 255).</i>	<b>37</b>
<b>Fig. 2.4.4:</b>	<i>The setup for intensity modulation</i>	<b>38</b>
<b>Fig.2.4.5:</b>	<i>How an SLM works - modulate the phase/intensity of the light</i>	<b>38</b>
<b>Fig. 2.4.6 (a):</b>	<i>Creation of multiple beams with Fourier Plane Hologram.</i>	<b>39</b>
<b>Fig. 2.4.6 (b):</b>	<i>Creation of multiple beams with a Fresnel Plane Hologram</i>	<b>40</b>
<b>Fig. 2.4.6 (c):</b>	<i>Creation of multiple beams with the third type of hologram, of the Fourier and Fresnel plane hologram</i>	<b>41</b>
<b>Fig. 2.5.1:</b>	<i>Fourier relationship between the plane of the hologram and the image space of the focal lens.</i>	<b>43</b>
<b>Fig. 2.5.2:</b>	<i>The diagram graphically shows how to generate phase hologram with the GS Algorithm</i>	<b>45</b>
<b>Fig.2.5.3:</b>	<i>Phase required for lateral and axial shifts.</i>	<b>46</b>
<b>Fig. 2.5.4:</b>	<i>2D arbitrary multiple laser beam pattern generated by complex superposition of prism phases</i>	<b>47</b>
<b>Fig 2.5.5:</b>	<i>Fresnel (near field) diffraction and Fraunhofer (far field) diffraction</i>	<b>50</b>
<b>Fig. 2.5.6:</b>	<i>Comparison of the reconstructive plane of multiple foci using Fourier (a) and Fresnel (b) plane hologram</i>	<b>51</b>
<b>Fig.2.5.7:</b>	<i>The interface of the LabVIEW program generated by Leach et al.</i>	<b>53</b>
<b>Fig.2.5.8:</b>	<i>A CGH calculated by the program (a) and its computational reconstruction (b).</i>	<b>54</b>
<b>Fig. 3.2.1:</b>	<i>Clark-MXR CPA2010 femtosecond laser system</i>	<b>58</b>
<b>Fig. 3.2.2:</b>	<i>CPA-2010 laser head schematic layout</i>	<b>58</b>

<b>Fig. 3.2.3:</b>	<i>Schematic of the fibre oscillator. WP denotes waveplates and BRF denotes birefringent filter</i>	<b>59</b>
<b>Fig. 3.2.4:</b>	<i>High-Q IC-355-800ps picosecond laser system</i>	<b>60</b>
<b>Fig. 3.2.5:</b>	<i>The interface of High-Q IC-355-800ps control software</i>	<b>61</b>
<b>Fig. 3.2.6:</b>	<i>Commercial SLMs used for current research: (a )Holoeye LC-R 2500, (b) Hamamatsu X10468-03 (X10468-04 has the same appearance of X10468-03).</i>	<b>62</b>
<b>Fig. 3.2.7:</b>	<i>Experiment setup for high power laser beam test on the SLMs</i>	<b>65</b>
<b>Fig. 3.2.8:</b>	<i>Variation in intensity with grey level, detected when uniform images are displayed onto the X10468-03 Hamamatsu SLM.</i>	<b>67</b>
<b>Fig. 3.2.9:</b>	<i>The change of detected relative intensity, <math>I_n / I_{max}</math>, versus the time after the illumination. The blue data is from X10468-03 SLM with high reflectivity dielectric coating, while the red data is from LC-R 2500 absorbing more thermal energy due to its lower reflectivity.</i>	<b>68</b>
<b>Fig. 3.2.10:</b>	<i>The workings of the galvanometer driven laser beam scanning system, which consists of two galvanometer driven mirrors (X and Y), a flat field f-theta lens with focal length <math>f \approx 100\text{mm}</math>, and integrated driver electronics enclosed in a black cube-like metallic case.</i>	<b>70</b>
<b>Fig. 3.2.11:</b>	<i>The interface of the software used to control the scanning galvanometer system.</i>	<b>71</b>
<b>Fig. 3.2.12:</b>	<i>Four axis (a) and five axis (b) Aerotech motion control systems used for current research</i>	<b>72</b>
<b>Fig. 3.3.1:</b>	<i>An ‘LLEC’ pattern with 32 desired diffracted beams projected on a paper screen.</i>	<b>73</b>
<b>Fig. 3.3.2:</b>	<i>Schematic diagram for blocking the zero order beam at the Fourier plane P of the 4f optical system</i>	<b>74</b>
<b>Fig. 3.3.3:</b>	<i>3D layout of the modeled 4f optical system</i>	<b>76</b>
<b>Fig. 3.3.4:</b>	<i>Spot diagram showing each spot size on the mirror – The radius of the spots, <math>r</math>, is given beneath; the energy</i>	<b>77</b>

intensity,  $I$ , hence was easily calculated by  $I = \frac{E_p}{\pi r^2}$ , which was well below the damage threshold of the mirror coating.

<b>Fig. 3.3.5:</b>	<i>Demonstration of the enhancement of the +1 diffracted orders (LLEC pattern) combined with blocking the zero order beam using a small metallic target. The image shows intensity distribution on a paper screen taken with a digital camera.</i>	<b>78</b>
<b>Fig. 3.3.6:</b>	<i>Interface of the software developed by Holoeye, which can easily superimpose and adjust the phase of the PFL.</i>	<b>79</b>
<b>Fig. 3.3.7:</b>	<i>Schematic showing the method to separate the focal plane of diffracted beams from the zero order beam. The added PFL, lens 1, can work as either positive lens (upper) or negative lens (lower) to obtain the separation, <math>\Delta d</math>. The beam matrix equation describes the propagation of diffracted beam from LCoS surface (A) to its focal plane (B)</i>	<b>81</b>
<b>Fig. 3.3.8 (a):</b>	<i>A CGH calculated by GL algorithm to generate eight first order identical beams (left) and its computational reconstruction (right)</i>	<b>81</b>
<b>Fig. 3.3.8 (b):</b>	<i>The CGHs superimposed by PFLs with different <math>f_1</math> to adjust <math>\Delta d</math> (upper) and the machined results on Ti6Al4V (lower)</i>	<b>82</b>
<b>Fig. 3.4.1:</b>	<i>Experiment setup without the 4f optical system</i>	<b>83</b>
<b>Fig. 3.4.2:</b>	<i>The schematic of experiment setup for Clark-MXR CPA2010 with a 4f optical system</i>	<b>84</b>
<b>Fig. 4.2.1 (a):</b>	<i>'LLEC' pattern comprising 32 micro-sized holes</i>	<b>89</b>
<b>Fig. 4.2.1 (b):</b>	<i>Random spots pattern comprising 30 micro-sized holes</i>	<b>89</b>
<b>Fig. 4.2.2:</b>	<i>Hole size and eccentricity versus the distance from each diffracted spot to the zero order hole in both 'LLEC' and random spots patterns</i>	<b>91</b>
<b>Fig. 4.2.3:</b>	<i>The zero orders removed when micro-structuring a silicon substrate with the 'LLEC' and random spots patterns.</i>	<b>92</b>

<b>Fig. 4.2.4 (a):</b>	<i>Illustration of how the desired +1 diffractive beam retains a round shape when the input beam has a single wavelength i.e. <math>\Delta\lambda \rightarrow 0</math>.</i>	<b>94</b>
<b>Fig. 4.2.4 (b):</b>	<i>Illustration of how the shape of desired +1 diffractive beam is elongated towards zero order beam when the input beam has a measurable finite bandwidth, <math>\Delta\lambda \approx 5\text{nm}</math>.</i>	<b>95</b>
<b>Fig. 4.2.5 (a):</b>	<i>Observed growing eccentricity of micro-machined holes on a silicon substrate with increasing diffractive angle of +1 orders, showing a slight tilt of the major axis. The ablation debris is deposited non-uniformly due to the asymmetric expansion of the plasma. The zero order is marked.</i>	<b>96</b>
<b>Fig. 4.2.5 (b):</b>	<i>Improved result over figure 4.2.5 (a) in which the major axis of the elliptical structures aligns to the zero order. The debris has been simply removed using methanol.</i>	<b>96</b>
<b>Fig. 4.2.6:</b>	<i>Experimental and calculated eccentricity <math>a/b</math> of machined holes versus angle of diffraction showing excellent agreement. Eccentricity increases linearly with angle of diffraction.</i>	<b>98</b>
<b>Fig. 4.2.7:</b>	<i>A comparison of ablation depth on Ti6Al4V with angle of diffraction and pulse number, showing that the ablation depth drops at higher angles due to increasing distortion of the intensity profile.</i>	<b>99</b>
<b>Fig.4.3.1:</b>	<i>Optical micrograph of the machined pattern on a silicon wafer, where the CGH1 was fading out and CGH2 was building up during the scanning. The number of zero order beam machined holes between A and B was 27, and the period of time between two adjacent holes was 1ms; hence the response time was estimated at <math>\sim 27\text{ms}</math>.</i>	<b>101</b>
<b>Fig. 4.3.2:</b>	<i>Rise and fall times of SLM (LC-R 2500) given by Holoeye.</i>	<b>101</b>
<b>4.3.3 (a):</b>	<i>Pattern completed by real time playing 15 series of CGHs at 20 Hz refresh rate (50ms duration per CGH).</i>	<b>103</b>
<b>Fig. 4.3.3 (b):</b>	<i>The stages in formation of the pattern of figure 4.2.3 (a)</i>	<b>103</b>
<b>Fig. 4.3.4:</b>	<i>Micro-channels obtained by combining CGH real time</i>	<b>104</b>

control with Galvanometer scanning

<b>Fig. 4.3.5:</b>	<i>'OPTICS' pattern created by 7 CGHs applied at appropriate positions using the galvanometer scanner (shown together with zero order holes)</i>	<b>106</b>
<b>Fig. 4.3.6:</b>	<i>'OPTICS' pattern with zero order holes eliminated (The insert 3D pictures were measured using Wyko NT1100 optical surface profiler, illustrating the depth of the holes)</i>	<b>106</b>
<b>Fig. 5.2.1:</b>	<i>Schematic of experiment setup for High-Q IC-355-800ps with a 4f optical system</i>	<b>109</b>
<b>Fig. 5.3.1:</b>	<i>(a) A series holes drilled on a silicon sample when varying the diffractive angle. (b) The 2D (left) and 3D (right) micrographs with large magnification, showing the shape of the hole, fabricated by single 10ps pulse, when applying large diffractive angle, <math>\theta &gt; 1^\circ</math></i>	<b>111</b>
<b>Fig. 5.3.2:</b>	<i>The eccentricity <math>e</math> of hole shape drilled by 10ps when varying the angle of diffraction.</i>	<b>112</b>
<b>Fig. 5.3.3:</b>	<i>The variation of ablation depth using one thousand 10ps pulses (<math>E_p \approx 5\mu J</math>) when varying the angle of diffraction.</i>	<b>112</b>
<b>Fig. 5.4.1:</b>	<i>Schematic showing the design of the 25 beams pattern and the method of scanning (The vertical distance between two adjacent spots was <math>100\mu m</math>; by repeatedly scanning the pattern with <math>50\mu m</math> vertical offset each time, multiple micro-channels with <math>50\mu m</math> intervals can be obtained.)</i>	<b>113</b>
<b>Fig. 5.4.2:</b>	<i>Micrograph demonstrating the results of micro-channels covering a <math>10 \times 10mm</math> area machined by the 25 beams pattern on polished Ti6Al4V (upper), and micrographs showing the result with higher magnification (lower left) and 3D surface profile image by Wyko NT1100 optical surface profiler (lower right)</i>	<b>114</b>
<b>Fig. 6.2.1:</b>	<i>The periodic <math>5 \times 5</math> array with high degree of symmetry - the basic geometric design of a diffractive pattern</i>	<b>118</b>
<b>Fig. 6.2.2:</b>	<i>Schematic showing that by applying a freedom of asymmetry, <math>R</math>, the position of each desired diffractive</i>	<b>119</b>

peaks is no longer fixed, but randomly located within a circle area.

<b>Fig. 6.3.1:</b>	<i>The optical micrographs demonstrating the machining results on a polished Ti6Al4V substrate using LG algorithm when the freedom of asymmetry was set to be: <math>R = 2 \mu\text{m}</math>, <math>20 \mu\text{m}</math>, <math>50 \mu\text{m}</math>. Clearly, the pattern with high degree of symmetry, shows poor uniformity, e.g. When <math>R = 2 \mu\text{m}</math>, <math>V \approx 41.2\%</math>, while more asymmetrically designed pattern has good uniformity, e.g. When <math>R = 50 \mu\text{m}</math>, <math>V \approx 5.6\%</math></i>	<b>121</b>
<b>Fig. 6.3.2 (a):</b>	<i>The diffractive efficiency of the multi-beam pattern versus the freedom of asymmetry, <math>R</math></i>	<b>122</b>
<b>Fig. 6.3.2 (b):</b>	<i>The uniformity of the machined holes on a Ti6Al4V substrate (described by the Percentage of Variation) versus the freedom of asymmetry, <math>R</math></i>	<b>122</b>
<b>Fig. 6.3.3 (a):</b>	<i>The design of a <math>10 \times 4</math> hole array pattern formed by four asymmetric patterns.</i>	<b>123</b>
<b>Fig. 6.3.3 (b):</b>	<i>The processing results of <math>10 \times 4</math> holes array pattern with (left) and without (right) zero order holes</i>	<b>124</b>
<b>Fig. 6.3.3 (c):</b>	<i>The result produced by repeating the patterns with the galvanometer system to create large area processing.</i>	<b>125</b>
<b>Fig. 6.3.3 (d) and (e):</b>	<i>Schematic showing the combination of the four asymmetric patterns used to generate 3D chessboard-like structure (d), and the micro-machined 3D chessboard structure (e)</i>	<b>125</b>
<b>Fig. 6.4.1:</b>	<i>A digital camera photograph showing a diffractive pattern reconstructed on a paper screen – Only the four brighter spots marked by a blue triangle are the desired diffractive orders, all the other weaker spots appearing on the dark background are the ghosts. The red dashed line marks a series of spots generated by a phase grating, where only the +1 order is desired.</i>	<b>126</b>
<b>Fig. 6.4.2:</b>	<i><math>N \times M</math> beams array</i>	<b>127</b>
<b>Fig. 7.2.1:</b>	<i>Multi-beam pattern design for surface micro-structuring of</i>	<b>131</b>

silicon – generating a  $10 \times 4$  beam array

<b>Fig. 7.2.2:</b>	Scanning patterns for six concentric circles. (a) $d = 0.3\text{mm}$ ; no interference among the scanned circles, (b) $d = 0.2\text{mm}$ ; partial interference among the scanned circles, (d) $d = 0.15$ , total interference among the scanned circles.	<b>132</b>
<b>Fig. 7.2.3:</b>	Change of the contact angle versus the surface morphology (controlled by $d$ ) and chemistry (before and after the oxidised layer removed)	<b>134</b>
<b>Fig. 7.3.1:</b>	The layered structure of OLED material.	<b>135</b>
<b>Fig. 7.3.2:</b>	Parallel processing of OLED. Optical micrographs (Upper), cross-sectional profile of a single line (bottom)	<b>136</b>
<b>Fig. 7.3.3:</b>	Parallel processing of ITO thin film sample using a diffractive multi- beam. Top: Optical micrographs; Bottom: Cross-sectional profile of a single scribe	<b>137</b>
<b>Fig. 7.4.1:</b>	(a) The CGH, calculated by 3D Gershberg-Saxton algorithm, which can create a ‘NWDA’ diffracted beam pattern with 39 multiple beams focused at two different planes. (b) Schematic showing the computationally reconstructed ‘NWDA’ pattern.	<b>138</b>
<b>Fig. 7.4.2:</b>	Processing result for the ‘NWDA’ pattern applied to a polished Ti6Al4V sample	<b>139</b>
<b>Fig. 7.4.3:</b>	Schematic demonstrating the size of hole adjusted by precisely modulating the focal height difference of each diffractive order, $\Delta d$ . (a) The diffractive beam is precisely focused on the sample surface hence fabricating a larger sized hole; (b) the diffractive beam is slightly out of focus by a distance ( $\Delta d$ ), hence fabricating smaller sized hole.	<b>140</b>
<b>Fig. 7.4.4 (a):</b>	Schematic of selective ablation using different number of spots per line to produce different ablation depth.	<b>140</b>
<b>Fig. 7.4.4 (b):</b>	Micrograph of 10 beams selective ablation on silicon. The red circles represent the positions of the 10 beams.	<b>140</b>
<b>Fig. 7.4.4 (c):</b>	Cross-sectional surface profile of the 10 beams selective ablation on silicon. The scribe line 1, 2, 3 and 4 are	<b>141</b>

consistent with those labeled in Fig. 7.2.4 (b)

<b>Figure 7.5.1:</b>	<i>Schematic showing internal volume grating fabrication by applying parallel processing of diffractive multi-beam.</i>	<b>142</b>
<b>Fig. 7.5.2:</b>	<i>Top: digital camera picture showing a series of volume gratings written inside a PMMA slab. Bottom: high magnification micrograph showing the fabricated grating with period, <math>T \approx 19\mu\text{m}</math>.</i>	<b>142</b>
<b>Figure 7.5.3:</b>	<i>Schematic showing the diffracted pattern of 21 desired beams, as applied to fabricate a volume grating at a scanning at a speed of 1mm/s</i>	<b>143</b>
<b>Fig. 8.2.1:</b>	<i>Selective ablation of multi-layer structured material using a diffractive multi-beam pattern</i>	<b>149</b>

## List of Tables

<b><u>Table no.</u></b>	<b><u>Table caption</u></b>	<b><u>Page</u></b>
<b>Table 3.1:</b>	<i>Specifications of SLMs employed for present research</i>	<b>64</b>
<b>Table 3.2:</b>	<i>The details of lens chosen for building up the 4-f optical system</i>	<b>75</b>
<b>Table 3.3:</b>	<i>Optimized value of distance between each optical element to minimize the wavefront distortion</i>	<b>77</b>
<b>Table 4.1:</b>	<i>The calibrated series of drilled holes diameter using a single beam of varying pulse energy</i>	<b>90</b>
<b>Table 7.1:</b>	<i>The results of micro-structuring of silicon using the diffractive multi-beam patterns</i>	<b>133</b>

## List of Symbols

<b><u>Symbol</u></b>	<b><u>Unit</u></b>	<b><u>Description</u></b>
$a$	$(\mu\text{m})$	Major semiaxis of ellipse
$A$	$n/a$	Amplitude of complex field
$b$	$(\mu\text{m})$	Minor semiaxis of ellipse
$C_e$	$(\text{J}\cdot\text{kg}^{-1}\cdot\text{K}^{-1})$	Specific heat capacity of electron
$C_l$	$(\text{J}\cdot\text{kg}^{-1}\cdot\text{K}^{-1})$	Specific heat capacity of lattice
$D$	$n/a$	Heat diffusion coefficient
$e$	$n/a$	Eccentricity of the hole shape
$E(t), E(r)$	$n/a$	Electric field
$E_p$	$(\mu\text{J})$	Pulse energy
$f$	$(\text{mm})$	Focal length
$F$	$(\text{J}\cdot\text{cm}^{-2})$	Laser fluence
$FT$	$n/a$	Fourier transform
$g$	$(\text{W}\cdot\text{m}^{-3}\cdot\text{K}^{-1})$	Electron-phonon coupling constant
$G$	$n/a$	Gain factor
$I$	$(\text{W}\cdot\text{cm}^{-2})$	Intensity
$k$	$n/a$	Wave number
$L$	$(\mu\text{m})$	Ablation depth per pulse
$l_d$	$(\mu\text{m})$	Heat diffusion length
$l_s$	$(\mu\text{m})$	Optical penetration skin depth
$n$	$n/a$	Refractive index
$NA$	$n/a$	Numerical aperture
$R$	$(\text{Hz})$	Repetition rate
$t$	$\text{K}$	Temperature
$T_e$	$\text{K}$	Temperatures of electrons
$T_l$	$\text{K}$	Temperatures of lattice
$X$	$(\mu\text{m})$	Distance of the beam from the axis
$\alpha$	$n/a$	Absorption coefficient

<b><u>Symbol</u></b>	<b><u>Unit</u></b>	<b><u>Description</u></b>
$\Delta d$	(mm)	Separation of focal planes
$\Delta l$	( $\mu m$ )	Elongation of the hole shape
$\Delta n$	n/a	Refractive index change
$\Delta \lambda$	(nm)	Spectral bandwidth
$\delta$	n/a	Optical path difference
$\eta$	n/a	Diffraction efficiency
$\theta_i$	( $^\circ$ )	Incident angle
$\theta_m$	( $^\circ$ )	m-th order diffractive angle
$\kappa_e$	( $W \cdot K^{-1} \cdot m^{-1}$ )	Electron thermal conductivity
$\lambda$	(nm)	Wavelength
$\Lambda$	( $\mu m$ )	Grating period
$\nu$	(Hz)	frequency
$\tau_p$	(fs or ps)	Pulse duration (pulsewidth)
$\varphi$	n/a	Phase of complex field
$\Phi$	( $\mu m$ )	Hole diameter
$\psi$	a/n	Complex field representing the laser beam
$\omega_0$	( $\mu m$ )	Beam waist

## List of Abbreviations

<b><u>Abbreviations</u></b>	<b><u>Full names</u></b>
<i>3D</i>	<i>Three dimension</i>
<i>AR. coating</i>	<i>Anti-reflection coating</i>
<i>BBO crystal</i>	<i>Beta-barium borate crystal</i>
<i>CCD</i>	<i>Charge-coupled device</i>
<i>CGH</i>	<i>Computer generated hologram</i>
<i>CPA</i>	<i>Chirped pulse amplification</i>
<i>DVI</i>	<i>Digital visual interface</i>
<i>ER-SLM</i>	<i>Electrically addressed reflective SLM</i>
<i>FWHM</i>	<i>Full-width at half-maximum</i>
<i>GS algorithm</i>	<i>Gerchberg-Saxton algorithm</i>
<i>IR</i>	<i>Infrared</i>
<i>ITO</i>	<i>Indium tin oxide</i>
<i>LC</i>	<i>Liquid crystal</i>
<i>LCoS</i>	<i>Liquid crystal on silicon</i>
<i>LG algorithm</i>	<i>Lenses and gratings algorithm</i>
<i>LLEC</i>	<i>Lairside laser engineering centre</i>
<i>MEMs</i>	<i>Microelectromechanical systems</i>
<i>MPFL algorithm</i>	<i>Multiplexing phase fresnel lenses algorithm</i>
<i>NIR</i>	<i>Near Infrared</i>
<i>NWDA</i>	<i>Northwest regional development agency</i>
<i>OLED</i>	<i>Organic light emitting diode</i>
<i>PFL</i>	<i>Phase Fresnel lens</i>
<i>PMMA</i>	<i>Poly(methyl methacrylate)</i>
<i>SLM</i>	<i>Spatial light modulator</i>
<i>UV</i>	<i>Ultra-violet</i>
<i>XGA</i>	<i>Extended graphics array</i>

# **Chapter 1**

## **Introduction**

## 1.1 Background to research area

During the last decade, ultrashort pulse lasers have been employed for high precision surface micro-structuring of materials such as metals, semi-conductors and dielectrics with little thermal damage. Due to the ultra high intensity of focussed femtosecond pulses ( $I > 10^{12} \text{W/cm}^2$ ), nonlinear absorption can be induced at the focus leading to highly localised material ablation or modification. This is now opening up applications ranging from integrated optics, through multi-photon induced refractive index engineering to precision surface modification for silicon scribing and solar cell fabrication.

However, experimental results have demonstrated that significant thermal effects still occur during material processing with the ultrashort pulses when high pulse energy is applied. To ensure non thermal material processing, the input fluence,  $F$ , must be kept in the low regime ( $F \sim 1 \text{Jcm}^{-2}$ ), a few times above the well defined ablation threshold. Accordingly,  $\mu\text{J}$  ( $10^{-6}\text{J}$ ) level pulse energy input is often required for ultrashort pulse laser fine micro/nano-surface structuring.

Figure 1.1 (a) and (b) show the single pulse ( $\tau_p \sim 160\text{fs}$ ) machined craters with  $300\mu\text{J/pulse}$  ( $F \sim 10.6\text{Jcm}^{-2}$ ) and  $2\mu\text{J/pulse}$  ( $F \sim 0.63\text{Jcm}^{-2}$ ) input pulse energy ( $E_p$ ) respectively. Thermal effects, with surface melting and melt expulsion are evident in the crater machined at  $E_p \approx 300\mu\text{J}$ , while the crater machined by  $E_p \approx 2\mu\text{J}$  with diameter  $< 10\mu\text{m}$  and depth  $< 100\text{nm}$  shows a perfectly clean surface with negligible thermal effects.

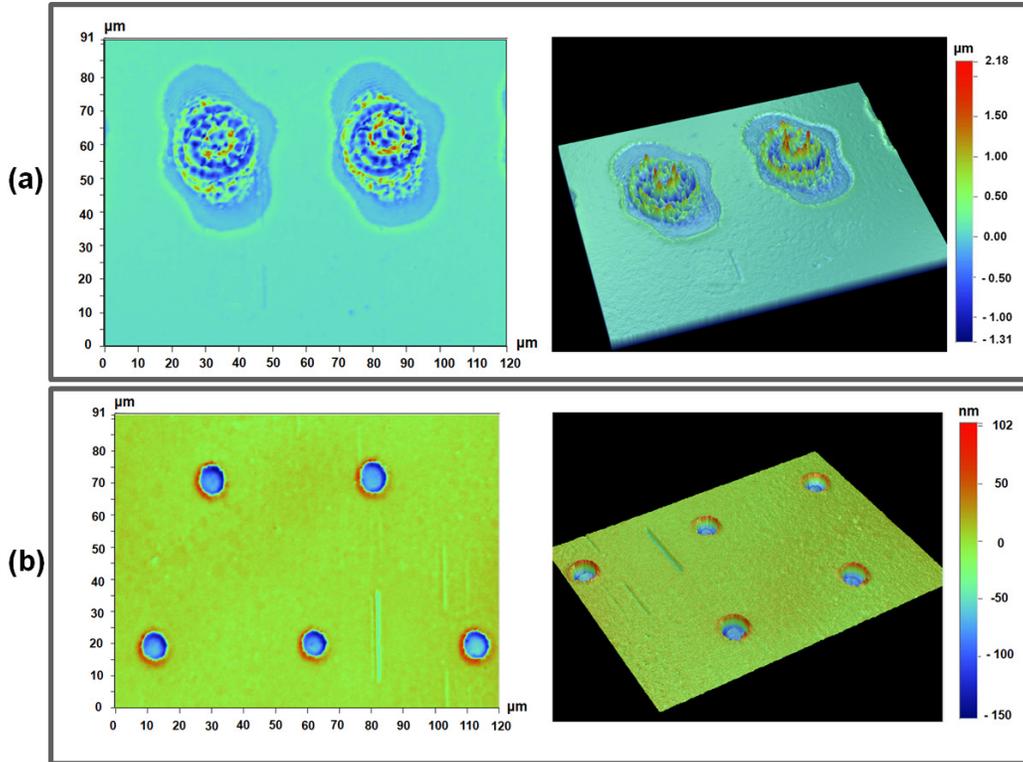


**Fig. 1.1:** The craters generated by single ultrashort pulses ( $\tau_p \sim 160\text{fs}$ ) on a sample of silicon wafer. The pulse energy was  $\sim 0.3\text{mJ}$  in (a), and  $\sim 2\mu\text{J}$  in (b). Surface melting is observed in (a), while the results in (b) shows a perfectly clean surface with much less thermal effects.

## 1.2 Motivation

Running at one kilohertz repetition rate, many current ultrashort pulse laser systems can provide mJ ( $10^{-3}\text{J}$ ) level output pulse energy. Accordingly, significant attenuation of the laser output is required for many applications and hence causes a great deal of energy loss.

Increasing the repetition rate of ultrashort pulse laser is a method to improve the processing efficiency and throughput; however, a system optimised for 1kHz operation is not easily re-configured for higher frequencies. Ultrashort pulse laser

systems operating at much higher frequencies, above 100kHz can hit speed limitations on scanners while much more care is required in terms of pulse gating and synchronisation.

Generating multiple beams, spatially splitting a mJ level energy laser pulse into many  $\mu\text{J}$  laser pulses required for high quality non-thermal micro-machining, is another method to increase the efficiency and throughput of ultrashort pulse laser processing. From multiple-beam interference to micro-lens arrays, previous studies have demonstrated many approaches to create multiple beams to improve ultrashort pulse laser micro-fabrication. In order to generate arbitrary multiple beam patterns, being able to attempt parallel processing flexibly and variably, the Spatial Light Modulator (SLM) which is a powerful device of dynamic diffractive optical elements (DOE) has been employed for multiple beam generation, as shown in figure 1.2. However, due to the complicated experimental alignment, the processing is not sufficiently flexible to reach industrial requirement. Additionally, the uniformity of multiple beams is problematic, which can significantly degrade the machining quality.

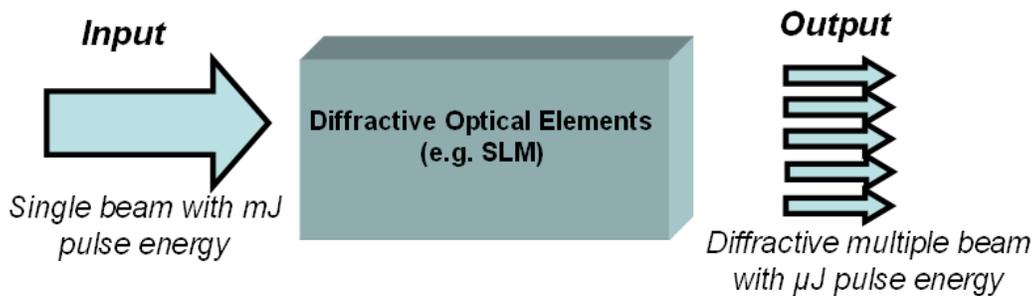


**Fig. 1.2:** Split mJ level input single beam into many  $\mu\text{J}$  level diffracted beams for thermal-free precision ultrashort pulse laser micro-processing.

With these limitations in mind, the present study uses an SLM allowing mJ pulse energy input to variably create > 30 uniform multiple beams with the demonstration of addressing CGHs in real time and synchronizing with a scanning method, which adds a great flexibility for material micro-processing. Furthermore, the uniformity of multiple beams is studied in this thesis, which gives some solutions of generating multi-beam patterns with a high uniformity.

With the high throughput gain and the great processing flexibility, the result shows many potential applications, such as fabrication of hydrophobic biomimetic surfaces with a self-cleaning ability, surface micro-structuring of metals or silicon wafers (the materials for Microelectromechanical systems (MEMS) manufacturing), and laser patterning of multi-layer structured materials, e.g. Organic Light Emitting Diode (OLED) and thin film solar cells.

### **1.3 Overview of the thesis**

The thesis consists of eight chapters. The current chapter (Chapter 1) is the main introduction of the thesis.

Chapter 2 is the literature review. The relevant background knowledge, ranging from a brief introduction of ultrashort pulse laser systems, ultrashort pulse induced material processing to a review of the diffractive multi-beam generation method using an SLM, is reviewed in this chapter.

Chapter 3 is the experimental basis of the thesis, where the main equipment employed for the research is introduced in detail and the experimental setup is demonstrated.

Chapters 4 to 7 are the results and discussion section of the thesis. First of all, Chapter 4 focuses on the diffractive multi-beam microprocessing using femtosecond laser pulses, where the results demonstrate great gains in processing throughput and flexible surface structuring by applying holograms in real time while synchronising the scanning galvanometer. However, chromatic distortion of the beam shape is observed due to the broad spectral bandwidth of the laser source. Accordingly, picosecond laser pulses with much narrower bandwidth are employed for parallel processing as described in Chapter 5. The results not only demonstrate negligible chromatic distortion, but also faster processing speed with higher repetition rate. Then, Chapter 6 describes a study of diffractive pattern uniformity, which significantly affects the reproducibility of processing. Finally, potential applications are demonstrated in Chapter 7. Finally, Chapter 8, Conclusions and future work, is the last part of the thesis.

As shown in the *List of Publications* (page IV), some of the results demonstrated in this thesis have been published. I made the major contributions (including giving original ideas, carrying out experiments, analysing results and writing articles) to those listed publications where I was the first author, while the other co-authors provided some helpful assistance, such as preparing samples, booking equipment, and commenting on my writing.

# **Chapter 2**

## **Literature Review**

## 2.1 Introduction

This chapter will review the background knowledge of current research. Ultrashort pulse laser systems and ultrashort pulse laser microprocessing of materials will be introduced. One of the main drawbacks of ultrashort pulse laser material processing is the low processing efficiency and throughput. Overcoming this limitation of ultrashort pulse laser processing by creating multiple beams with a Spatial Light Modulator (SLM) is the main purpose of this research. In the following sections of this chapter, different methods of generating multiple beams will be discussed by reviewing the relevant literature.

## 2.2 Ultrashort pulse laser systems and ultrashort pulse laser material processing

### 2.2.1 Ultrashort pulse laser systems

#### 2.2.1.1 Emission spectrum of the active medium

In order to generate an ultrashort pulse in a laser oscillator, the laser active medium, the fundamental requirement for an ultrashort pulse laser, must have a broad, continuous emission spectrum. This is due to the principle that the Fourier-transform-limited laser pulse duration is inversely proportional to its spectral width,

$$\tau_p \cdot \Delta\nu = \text{constant} \quad (2.2.1)$$

where  $\tau_p$  is the pulse duration and  $\Delta\nu$  is the pulse frequency spectrum, both measured at Full-Width at Half-Maximum (FWHM) [2-4]. For a Gaussian pulse, whose electrical field amplitude is given by:

$$E(t) = E_0 \exp(-2\pi\nu_0 t) \exp(-2 \ln 2 \frac{t^2}{\tau_p^2}) \quad (2.2.2)$$

The spectral amplitude is the Fourier transform:

$$E(\nu) = \text{FT}\{E(t)\} = E_0 \exp\left[-2 \ln 2 \frac{(\nu - \nu_0)^2}{\Delta\nu^2}\right] \quad (2.2.3)$$

and:

$$\tau_p \cdot \Delta\nu = \frac{2 \ln 2}{\pi} \approx 0.44 \quad (2.2.4)$$

To meet this fundamental requirement, Ti:sapphire, which has an emission spectrum that can support pulses down to  $\sim 6$ fs, has been widely chosen by researchers and commercial ultrashort pulse laser manufacturers to be the ultrashort pulse laser active medium. Other ultrashort pulse laser active media include: dyes, Cr:LiSAF, Nd:glass, Yb:glass, Yb:YAG, and Cr:YAG.

With a suitable laser active medium, ultrashort pulses are generated in a mode-locked oscillator, which can be accomplished either by Kerr-lens mode locking [5], additive pulse mode locking [6], or a special solid-state passive saturable absorber [7, 8]. Furthermore, dispersion in the optical materials (i.e. different frequency components of the pulse travel at different speeds) may stretch out the short pulse with broad spectral bandwidth,  $\Delta\nu$ , in the active medium and other optical elements in the cavity, termed pulse spreading. Therefore, in addition to mode locking, the ultrafast oscillator has to compensate pulse spreading by inserting an optical component with dispersion opposite to the optical active medium into the oscillator. This component is usually made of a prism pair [9, 10] or specially designed chirped mirrors [11, 12].

### 2.2.1.2 Chirped pulse amplification (CPA)

The ultrashort pulse laser oscillator usually operates at a pulse repetition rate of approximately 100 MHz, giving the pulse energy,  $E_p$ , in the range of nanojoules (nJ). However, for many applications, including micromachining, this level is insufficient;

hence amplification to the millijoule (mJ) level is necessary. The pulses cannot be amplified directly, as the optical components inside the amplifier will be damaged by the high intensity level of the short pulses; furthermore, the effect of self-focusing associated with high-intensity pulses can make the situation worse.

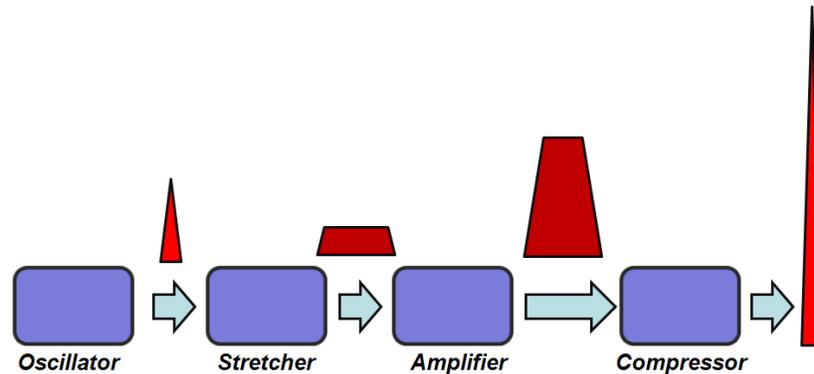


**Fig. 2.2.1:** The principle of chirped-pulse amplification for high-power ultrashort pulse generation. The pulse duration manipulation is to overcome damage of optical materials by high-power laser pulses in the amplifier.

Accordingly, the technique of chirped-pulse amplification (CPA) has been developed to overcome this limitation [13]. As illustrated in figure 2.2.1, which schematically shows the principle of CPA, there is a pulse stretcher between the oscillator and amplifier, increasing the pulse duration by a factor of  $10^3$ – $10^4$  times, and hence reducing the peak power to avoid damage. Then, the stretched pulse can be safely amplified, neatly avoiding non-linear effects which would otherwise lead to component damage. Finally, in the compressor, the amplified long pulse can be recompressed back to its original pulse duration with  $\sim$  mJ pulse energy.

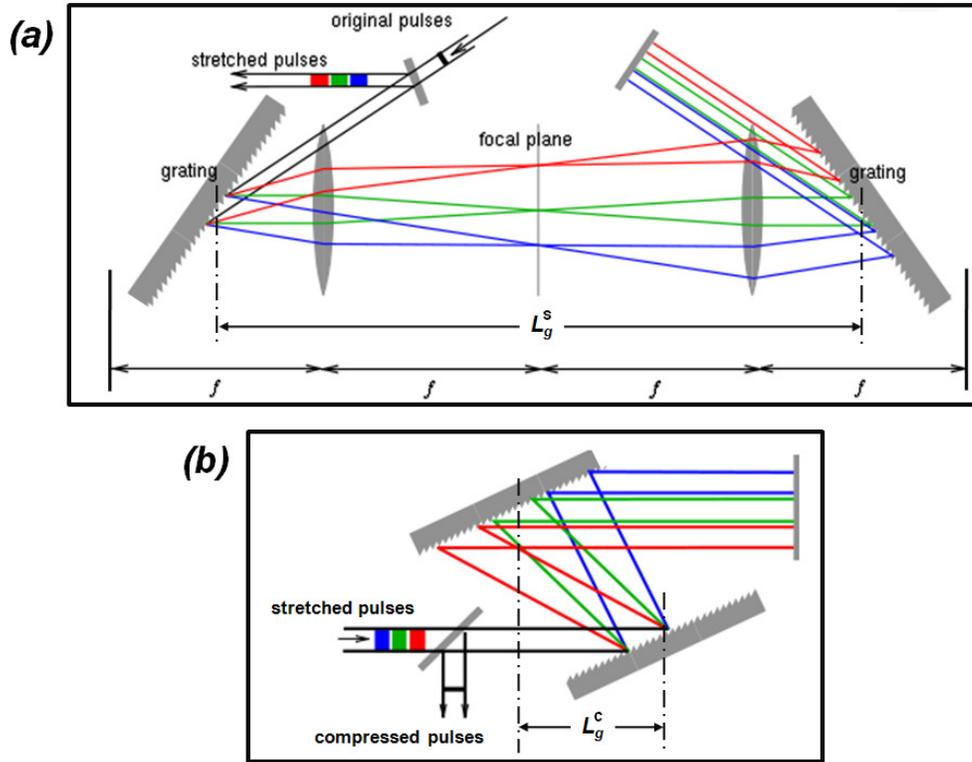


**Fig. 2.2.2:** Grating-pair pulse stretcher (a) and compressor (b). The gratings in the stretcher are antiparallel and are parallel in the compressor. [16]

The pulse stretcher and compressor are normally made of a pair of optical gratings [14]. Figure 2.2.2 (a) demonstrates one implementation of the grating stretcher [15, 16]. The dispersive properties of the gratings are exploited to change the pulse duration of an ultrashort pulse having broad frequency spectral bandwidth,  $\Delta\nu$ , and the pulse is stretched while travelling between the pair of optical gratings. Different frequency components in the pulse are dispersed into different directions each time reflected on the gratings; hence they have different optical path lengths. Consequently, the frequency component that has a shorter optical path length will come out earlier than the frequency component that travels a longer path, hence the pulse is stretched. The amount of stretching is determined by the distance,  $L_s = 4f - L_g^s$ , where  $L_g^s$  is the separation of the stretcher grating-pair.

The compressor, demonstrated in Figure 2.2.2 (b), is also made of a pair of gratings, but the dispersion is arranged in the opposite way as the stretcher. The amount of compression is simply determined by the separation of the grating-pair,  $L_c = L_g^c$ . To obtain the shortest compressed pulse, the compressor and the stretcher must match so that  $L_c = L_s$ . Pulse duration other than the shortest can be easily obtained by simply misaligning the compressor to the stretcher by varying the grating separation. Figure 2.2.3 schematically shows a chirped pulse amplification system with grating-pair pulse stretcher and compressor.

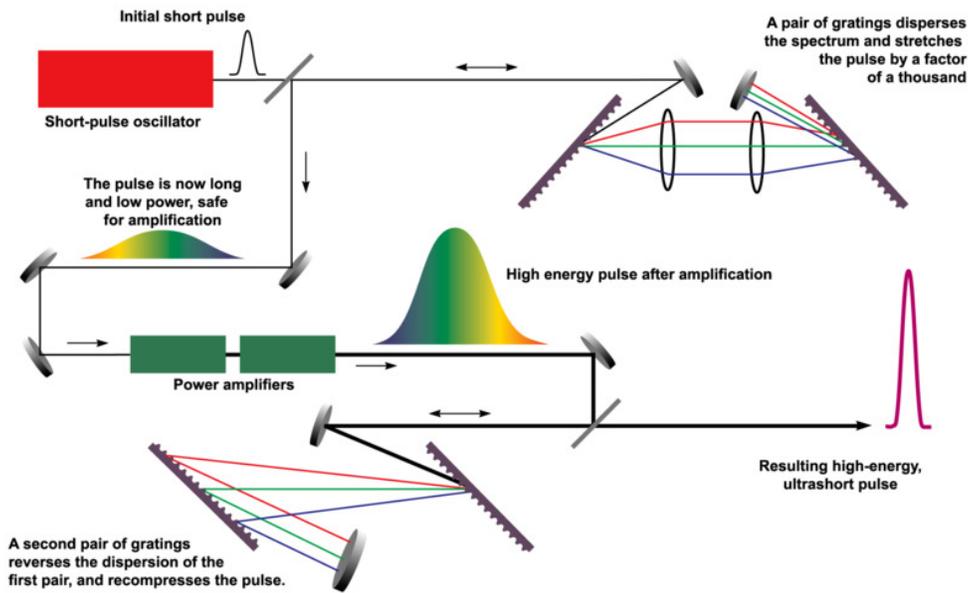


*Fig. 2.2.3: Diagrammatic scheme of chirped pulse amplification [16]*

Some experiments in this research are based on the use of a turnkey Ti:sapphire CPA femtosecond laser, a Clarke-MXR 2010 system, which delivers maximum pulse energy  $E_p \approx 1$  mJ at 1 kHz repetition rate, 775 nm fundamental wavelength ( $\lambda$ ), 180 femtosecond pulse duration and observed bandwidth  $\Delta\lambda = 1/\Delta\nu \approx 5.5$  nm. Additional, a picosecond laser system, High-Q IC-355-800ps, which generates ultra

short laser pulses at 10ps with much narrower bandwidth ( $\Delta\lambda \approx 0.1$  nm) is also employed for current research. More details about these lasers will be introduced in Chapter 3.

### **2.2.1.3 Simple and compact picosecond laser system**

The successful generation of ultrashort pulses with mJ level pulse energy and kilohertz repetition rate, mode locking (e.g. Kerr-lens) in solid-state (e.g. Ti:Sapphire) lasers [17-21] with chirped pulse amplification [21-25] has been an important achievement in the development of powerful ultrashort pulse laser sources. However, as can be seen from the above description, the CPA technique based ultrashort pulse laser system is considerably more complex than a long-pulse laser system that does not involve pulse duration manipulation. To operate and maintain such a laser system, specialized laser technical know-how and competence are needed. Considering a Ti:Sapphire CPA laser, the pump laser for the ultrafast oscillator and the amplifier are large-frame argon lasers or flashlamped-pumped frequency-doubled Nd:YAG lasers, which bring size, stability, and reliability problems to the system. Additionally, to ensure pulse duration and beam quality, the tolerances of alignment of stretcher and compressor are stringent. All these are impractical for such a laser system to be used in an industrial manufacturing environment.

Since recent investigations demonstrated that pulse duration in the range of several picoseconds are well suited for the precise machining of metals [26, 27], picosecond laser systems, which are much simpler and more cost effective, have been reported [28-33] and manufactured [34, 35]. As the active medium used to generate picosecond laser pulses is based on neodymium-doped crystals (e.g. Nd:YAG or Nd:YVO<sub>4</sub>),

which allow for direct diode pumping, the whole system is much more compact, stable and reliable. Moreover, CPA is not required for picosecond laser systems due to the longer pulse duration, where the pulse intensity is not sufficiently high to cause any damage to optical components inside the amplifier.

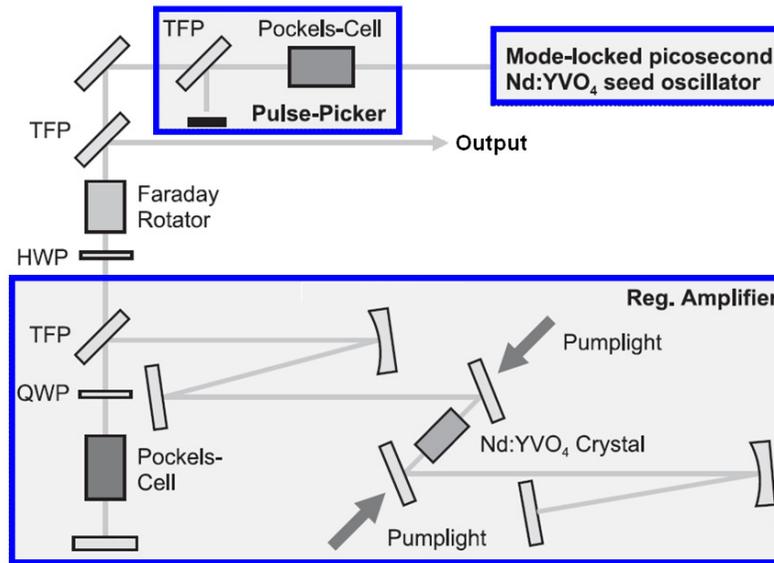


**Fig.2.2.4:** Schematic of the picosecond Nd:YVO<sub>4</sub> oscillator amplifier system

Figure 2.2.4 shows the schematic of a Nd:YVO<sub>4</sub> oscillator amplifier system, which consists of a mode-locked picosecond oscillator, a pulse picker and a regenerative amplifier [34]. Pumped with a diode laser, the mode locked picosecond Nd:YVO<sub>4</sub> seed oscillator generates picosecond pulses with MHz level repetition rate. Then, single pulses are selected from the train of picosecond laser pulses by a pulse picker, which consists of a thin-film polarizer (TFP) and a Pockels-cell. The selected pulses are then injected into the regenerative amplifier through a combination of a Faraday rotator and a half-wave plate (HWP). The main components of the regenerative amplifier are the optical resonator formed by a series of high-reflective mirrors, Nd:YVO<sub>4</sub> crystal pumped by a diode laser and an electro-optical modulator (Pockels cell). In combination with a thin-film polarizer (TFP) and a quarter-wave plate (QWP),

the Pockels cell allows the injecting the laser pulses selected by the pulse picker into the cavity of the amplifier. Finally, after several round trips, the amplified pulses with mJ level energy can be ejected from the resonator by the same optical elements.

Nowadays, commercial picosecond lasers based on this Nd:YVO<sub>4</sub> oscillator amplifier system can generate 10ps laser pulses with maximum  $E_p \approx 1\text{mJ}$ , e.g. High-Q IC-355-800ps, the picosecond laser system employed for current research (which will be discussed in more detail in Chapter 3). The output repetition rate of the pulses, up to several hundreds kHz, is tuneable by a function generator sending a signal to control the Pockels-cell. Moreover, the fundamental output wavelength of 1064nm can be frequency-doubled and tripled by properly adjusting the relevant half wave plate, generating 532nm and 355nm output, respectively [34].

### **2.2.2 Ultrashort pulse laser ablation of material**

In micromachining with lasers, especially drilling and cutting, material removal takes place through the ablation process where the target material under laser irradiation absorbs energy and transforms into either a liquid or a vapour. The melted liquid is expelled from the interaction region by the recoil action, while the vapour removes itself directly from the focus. Additionally, other processes, e.g. heat conduction, radiation, and plasma expansion, are associated with the laser-material interaction.

In contrast with long pulse laser processing, the ultrashort laser pulse induced ablation of material, demonstrates unique characteristics and potential advantages for high precision micromachining, indicating different physical mechanisms involved at ultrashort pulse duration. In this section, the characteristics of ultrashort pulse laser

material ablation and the difference with long pulse laser ablation are briefly introduced.

### 2.2.2.1 Absorption of laser energy

The first step in laser ablation is the absorption of laser energy by the target material. In the case of metals, laser energy is absorbed by free electrons due to inverse Bremsstrahlung. The absorption is followed by fast energy relaxation within the electronic subsystem, thermal diffusion, and energy transfer to the lattice due to electron–phonon coupling. Accordingly, the procedure of the energy transferring from laser pulses to the target material can be described by the following three stages [36-38] and is schematically shown in fig 2.2.5:

- (i) light absorption
- (ii) electron thermal diffusion
- (iii) electron-lattice relaxation.

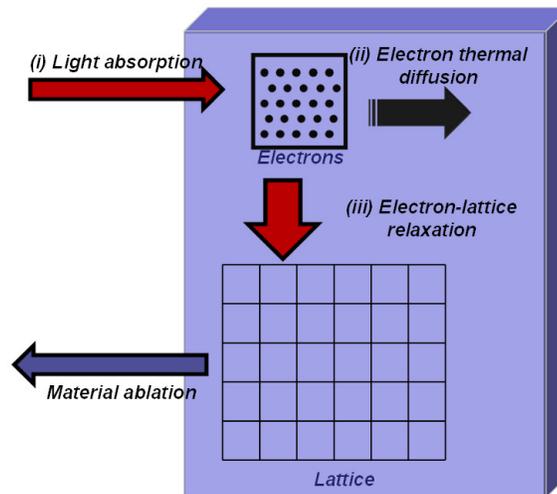


*Fig.2.2.5: Absorption of laser energy*

This energy transformation is often described in the frame of the one-dimensional two-temperature model shown below [36-38]:

$$C_e(T_e) \frac{\partial T_e}{\partial t} = \frac{\partial}{\partial x} (\kappa_e \frac{\partial T_e}{\partial x}) - g(T_e - T_l) + Q \quad (2.2.5)$$

$$C_l(T_l) \frac{\partial T_l}{\partial t} = g(T_e - T_l) \quad (2.2.6)$$

$T_e$  and  $T_l$  are the temperatures of electrons and the lattice, respectively,  $C_e$  and  $C_l$  are corresponding temperature dependent specific heat capacities,  $\kappa_e$  is the electron thermal conductivity,  $g$  is the electron-phonon coupling constant describing the energy exchange rate between electron and phonon subsystems, and  $Q$  is the laser power absorbed. Basically, the first equation 2.2.5 describes stages (i) and (ii), while the second equation 2.2.6 relates to stage (iii).

For most metallic materials, the time for electron-phonon coupling is from 1 to 100 picoseconds. For long laser pulses, e.g. nanosecond, where the pulse duration is much longer than lattice heating time, thermalization between the electron subsystem and the lattice takes place during the laser pulse. In this case the electrons and the lattice can be characterized by a common temperature  $T = T_e = T_l$ . However, in the case of ultrashort pulse lasers, the ultra-short pulse duration ( $< 10$ ps), is comparable to or shorter than the time for energy electron-phonon coupling, and the ultra-high instantaneous intensity involved causes the electron temperature to be significantly higher than the lattice temperature during all the stages. Hence, the energy absorption takes place under the extreme non-equilibrium temperature difference between the electrons and the lattice.

### 2.2.2.2 Well defined ablation threshold with ultrashort pulses

The ablation of material takes place after the target material absorbs energy from laser pulses with sufficient intensity, which is called the ablation threshold. Being different

from the long pulse induced threshold of material ablation, which has a large spread, the threshold at ultrashort pulse durations become more deterministic and precise [2].

Figure 2.2.6 shows a data for single-shot plasma emission generated by laser-induced ablation in fuse silica as a function of incident laser fluence for laser pulse duration of (a) 7ns and (b) 170fs [2]. As clearly shown in figure 2.2.6 (a), for long pulses the threshold has a large uncertainty. Some pulses with fluence considerably below the threshold value (the dash-line marked in the graph) caused plasma emission, indicating that material ablation was taking place, while some pulses with fluence far above the threshold did not cause ablation since no plasma emission was observed. However, the situation changes drastically when ultrashort laser pulses were used: the deviation in ablation threshold was well-defined in a very narrow range, as shown in figure 2.2.6 (b).

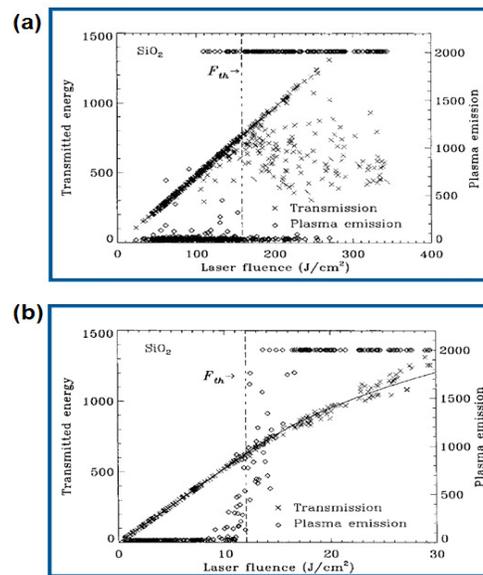


**Fig.2.2.6:** Single-shot plasma emission data of laser-induced breakdown in fused silica as function of incident laser fluence for laser pulse durations of (a) 7 ns and (b) 170 fs. [2]

Due to the well-defined ablation threshold, the ablation of material can be precisely controlled by the input fluence of the ultrashort pulse laser, which shows one of the potential advantages for high precision micromachining.

### 2.2.2.3 ‘Thermal-free’ processing with ultrashort laser pulses

When the laser energy is deposited in a surface layer, the thickness of the layer is given by the optical penetration skin depth:

$$l_s = \frac{1}{\alpha} \quad (2.2.7)$$

where  $\alpha$  is the absorption coefficient. There is another characteristic length, which is the heat diffusion length during the laser pulse, giving the heat penetration depth due to thermal conduction. This diffusion length is given by:

$$l_d = \sqrt{D\tau_p} \quad (2.2.8)$$

where  $D$  is the heat diffusion coefficient and  $\tau_p$  is the laser pulse duration. For long pulses,  $l_d > l_s$ , a great volume of the material can be heated by the laser pulse, hence the temperature is determined by the heat diffusion length during the laser pulse. However, in the case of ultrashort pulses, as the laser pulse duration decreases to a value  $\tau_p$  such that  $l_d = \sqrt{D\tau_p} < l_s$ , the skin depth determines the heated volume during the laser pulse, not the heat penetration depth. [39, 40]

As shown in figure 2.2.7, for long pulses where the heat diffusion length is larger than the skin depth, a large volume is heated and melted; the ablation and material removal is accomplished through melt expulsion mainly driven by the vapour pressure. The processing can be very unstable due to the complicated fluid dynamics of the fluid phase. The heat diffusion is sometimes associated with the formation of surface shock

waves. These shock waves can damage nearby device structures or delaminate multilayer materials. While the amplitude of the shock waves varies with the material being processed, it is generally true that the more energy is deposited in the micromachining process, the stronger the associated shock waves. Additionally, after ablation, the resolidification of the melt can lead to irregular shapes of the crater, and different mechanical properties from the original material.

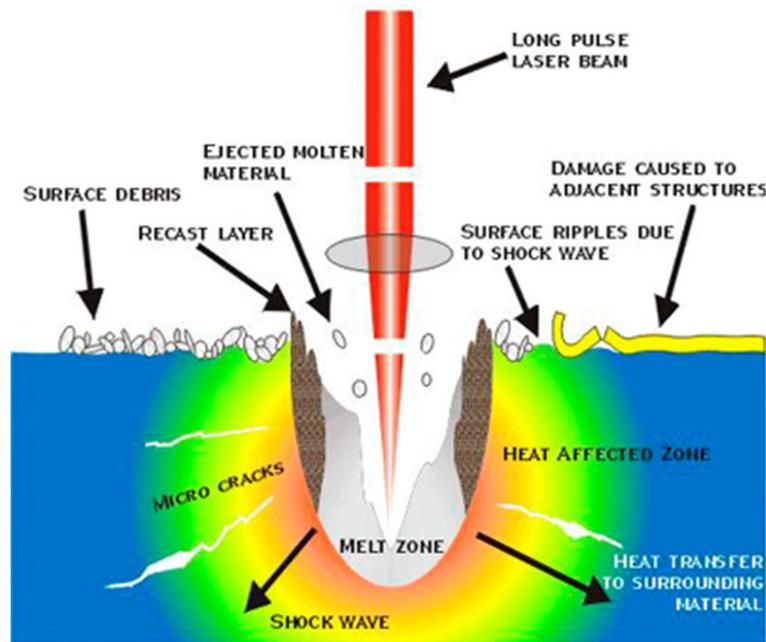


*Fig.2.2.7: Long pulse induced laser material ablation. [41]*

On the other hand, as shown in figure 2.2.8, for ultrashort pulses, the deposited laser energy is limited in a layer with a thickness of  $l_s$ . The localized energy heats the material very quickly past the liquid phase to the vapour phase with high kinetic energy (greatly above the vaporization temperature). The material removal is by direct vaporization away from the surface (into vacuum or air). Most of this is accomplished after the laser pulse irradiation is finished. Although the material may be still heated by the heat diffusion over a longer time scale, the resulting melt layer thickness can still be small because most of the heated material reaches vaporization temperature,

and there is rapid cooling due to the steep temperature gradient. The heating of the material by heat diffusion is further reduced by the fact that a large amount of the absorbed laser energy is carried away by the direct vaporization. Because there is little liquid involved, ablation and material removal become highly precise, in contrast to the long pulse case.

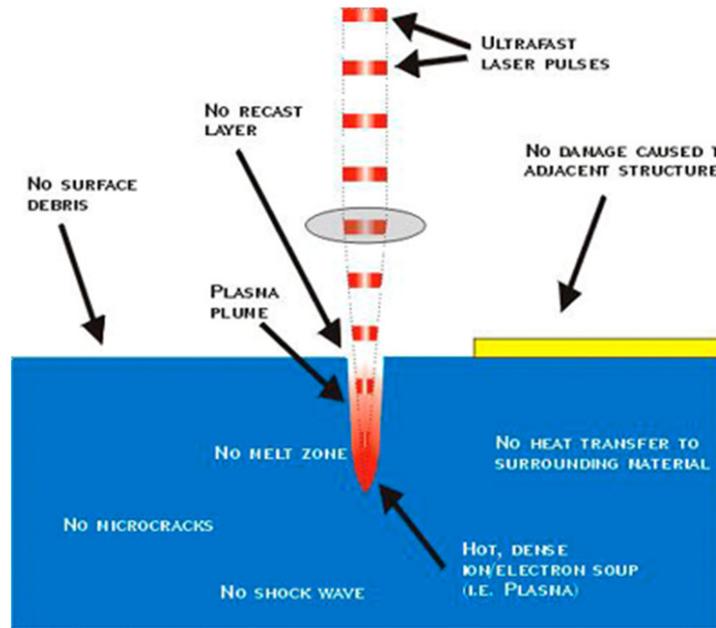


*Fig.2.2.8: Ultrashort pulse induced laser material ablation. [41]*

All in all, ultrashort pulse laser micro-processing of material, in contrast with long pulse lasers, has been called ‘cold processing’ with greatly reduced thermal effects such as melting and micro-cracking. These advantages have shown the great potential of ultrashort pulse lasers applied to precision micromachining of various materials. However, it has to be pointed out that figure 2.2.7 and figure 2.2.8 are ‘idealised’ pictures of both cases. Not all the problems with long laser pulses could benefit from the use of ultrashort pulses in every case. Dausinger reported that when machining metals, using the laser with femtosecond level pulse duration does not guarantee the

absence of recast and beam deformation. This is due to nonlinear effects which can significantly degrade the machining quality in the case of metal ablation [42].

#### **2.2.2.4 Material processing with picosecond laser pulses**

From a laser-materials interaction point of view, Dausinger [42] argued that the mere reduction of pulse duration does not guarantee good machining quality and suggested that a pulse duration of 5 to 10 ps appears to be optimal for micromachining, especially for metals. A number of research groups have shown that picosecond laser micromachining can produce high machining quality combined with efficiency [43-47].

According to the one-dimensional two-temperature model [36-38], metals with different electron–phonon coupling constants should have their own corresponding coupling time ranges. Hence, for micro-structuring a metal with a coupling time,  $\tau_{e-p}$ , in the ps regime, which is the timescale required for the lattice to reach thermal equilibrium, the temporal pulse width, whether fs or ps, should play only a minor role. Recently, co-workers in the Liverpool Laser Group, have published a single pulse drilling study on metals using a picosecond laser, demonstrating similar machining results on Au ( $\tau_{e-p} > 119\text{ps}$ ) using a 10 ps pulse, compared to an 180fs pulse [46], as shown in figure 2.2.9.

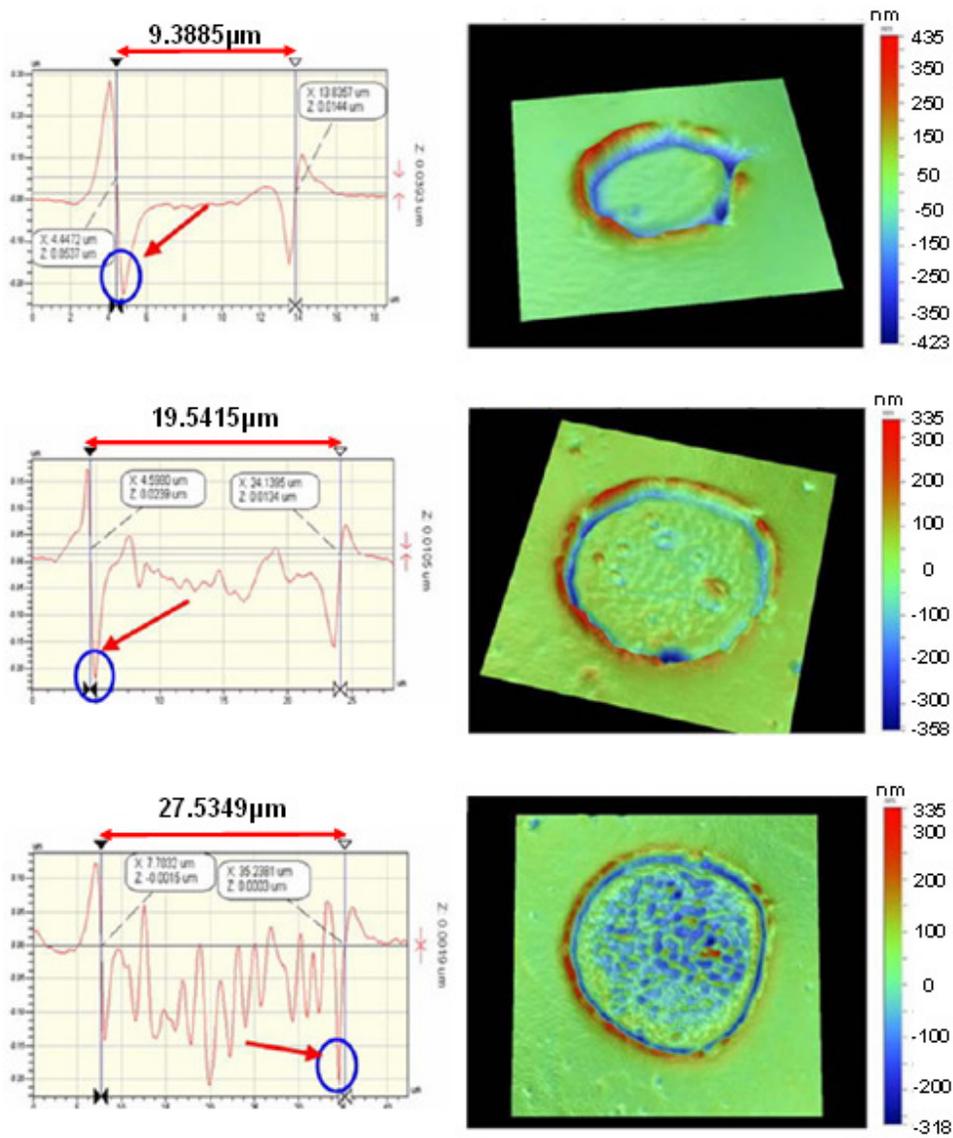


**Fig.2.2.9 (a):** Cross section profiles (left) and 3-D images (right) of single-pulse drilling of Au sample using a 10ps laser at a wavelength of 1064 nm under varied laser fluence under varied laser fluence: (a)  $F = 1 \text{ Jcm}^{-2}$ , (b)  $F = 5 \text{ Jcm}^{-2}$ , (c)  $F = 20 \text{ J cm}^{-2}$ . [46]

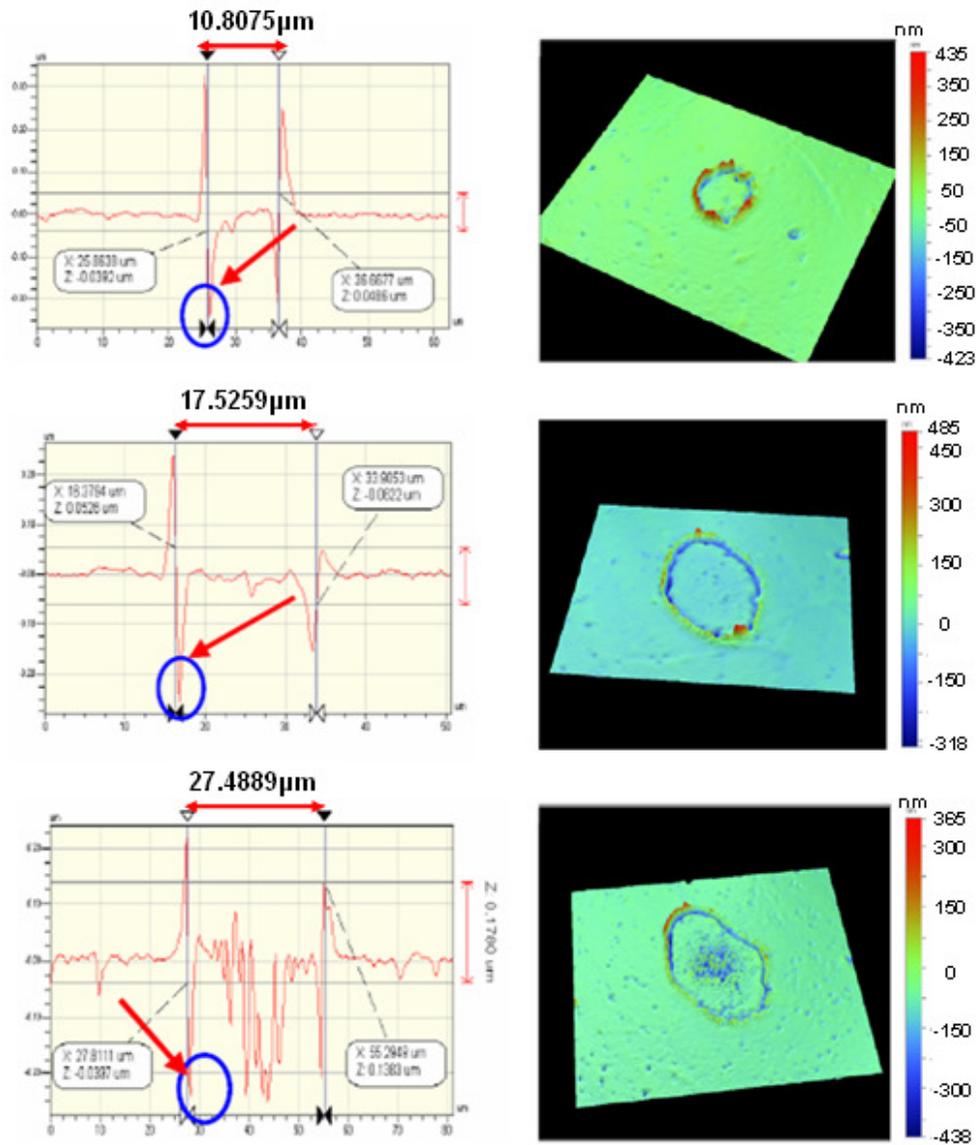


**Fig.2.2.9 (b):** Cross section profiles (left) and 3-D images (right) of single-pulse drilling of Au sample by using a 180 fs laser at a wavelength of 775 nm under varied laser fluence: (a)  $F = 1\ \text{J cm}^{-2}$ , (b)  $F = 5\ \text{J cm}^{-2}$ , (c)  $F = 10\ \text{J cm}^{-2}$ . [46]

### 2.2.3 The limitations of ultrashort pulse laser processing

It has been demonstrated that there are two separate ablation regimes for ultrashort pulse laser ablation of material [48, 49]. For low laser fluences ( $F < 1 \text{ J/cm}^2$ ), the ablation depth per pulse,  $L$ , can be described by the following expression [50, 51]:

$$L \approx \alpha^{-1} \ln(F / F_{th-l}) \quad (2.2.9)$$

where  $\alpha^{-1}$  is the optical penetration skin depth and  $F_{th-l}$  is the ablation threshold for the low fluence regime. At low laser fluence, the density of hot electrons is lower and the rate of electronic heat conduction is also lower. The electrons and lattice reach thermal equilibrium faster because of the smaller difference in electronic and lattice temperatures, thus allowing less time for electron thermal diffusion. Therefore the amount of energy transferring out of the optical skin depth is negligible and the ablation is characterized by the optical penetration skin depth.

At higher laser fluence ( $F > 1 \text{ J/cm}^2$ ), the expression is changed to:

$$L \approx l_d \ln(F / F_{th-h}) \quad (2.2.10)$$

where  $l_d$  is the electron heat diffusion length, and  $F_{th-h}$  is the ablation threshold for this regime. In this case, due to the high incident laser fluence, the temperature reached by the electrons is higher and the rate of electronic heat conduction is greater. Therefore, thermal equilibrium between the electrons and lattice takes a longer time, hence allowing more time for electron thermal diffusion. Thus, the ablation is characterized by the electron heat diffusion length,  $l_d$ , at higher fluences.

Previous studies have shown that in the low fluence regime, where  $F$  is  $0.1 - 1 \text{ J/cm}^2$ , thermal diffusion is almost absent during the ablation of material, leaving a smooth machined surface; however, in the high fluence regime, where  $F > 10 \text{ J/cm}^2$ , due to

the strong plasma effects, shock waves and increased heat conduction losses, the ablation rate is saturated and thermal effects occur, strongly affecting the microprocessing efficiency and negating the advantages of ultrashort pulse laser processing [51-53].

The SEM pictures in figure 2.2.10 demonstrate the results of single pulse ablation of a polished aluminium sample with 150fs pulse length at low (a) and high (b) fluence [52]. Clearly, the result with low fluence,  $F \approx 1.4\text{J}/\text{cm}^2$ , shows negligible melt and fine scratches observed at the centre of the ablated region, while, at higher fluence,  $F \approx 14\text{J}/\text{cm}^2$ , significant surface melting is observed in the crater with a recast ring around. The results confirm that significant thermal effects can still take place with ultrashort laser pulses and suggest that to minimize unwanted thermal effects, low pulse fluence is desirable.

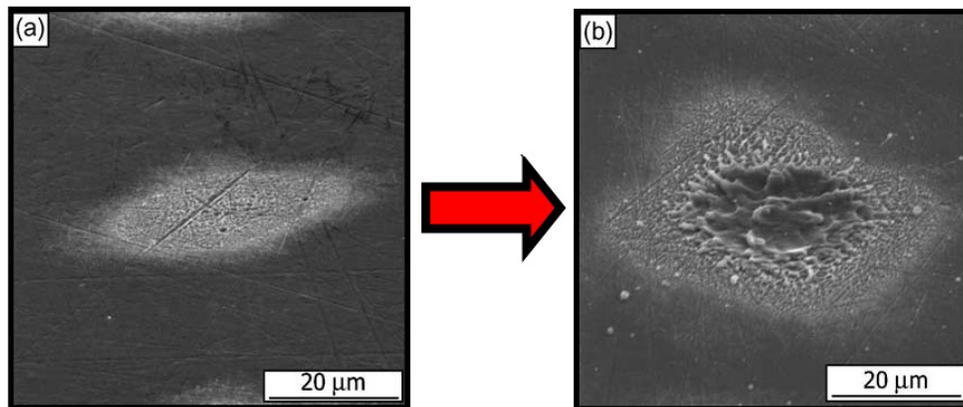


**Fig. 2.2.10:** Single shot femtosecond ablation of polished aluminium, where  $F \approx 1.4\text{J}/\text{cm}^2$  (a),  $F \approx 14\text{J}/\text{cm}^2$  (b). [52]

Accordingly, for the many applications of micro/nano-machining requiring high precision and quality, a pulse energy  $E_p < 10\ \mu\text{J}$  of the ultrashort pulse laser is required to ensure that ablation is taking place at the low fluence regime where

thermal effects are minimized. Nevertheless, current ultrashort pulse laser systems (which are able to provide maximum output at the mJ level of pulse energy running at kilohertz repetition rate) have to severely attenuate their output making the processing significantly slow and inefficient. For instance, a Clarke-MXR 2010 system based on chirped pulse amplification, one of the ultrashort pulse laser systems used for the current research, can generate 180fs laser pulses ( $\lambda = 775\text{nm}$ ) with maximum pulse energy  $E_p = 1\text{mJ}$  at 1kHz repetition rate. However, to ensure high quality, only less than 0.01mJ can be used for micro-machining with processing efficiency  $< 1\%$ ! This restriction may be one of the reasons why industrial uptake of kHz femtosecond systems has been limited.

### **2.3 Multiple beam parallel processing**

Generating multiple beams, spatially splitting a mJ level energy laser pulse into many  $\mu\text{J}$  laser pulses required for high quality non-thermal micro-machining, is a novel and straightforward method to increase the efficiency and throughput of ultrashort pulse laser processing. From multiple-beam interference [54-72] to micro-lens arrays [73-79], previous studies have demonstrated many approaches to create multiple beams to improve ultrashort pulse laser micro-fabrication. In order to generate arbitrary multiple beam patterns, being able to attempt parallel processing flexibly and variably, the Spatial Light Modulator (SLM) is a powerful device of dynamic diffractive optical elements (DOE), that has been employed by Hayasaki et al. [80-87]. The present study also uses an SLM to variably create multiple beams with the demonstration of addressing Computer Generated Holograms (CGHs) in real time and synchronizing with the scanning method, which adds an additional flexibility for surface micro-structuring and shows potential applications for industry [88-91].

### 2.3.1 Parallel microfabrication of periodic structures

Periodic multiple beam patterns can be obtained by multi-beam interference of ultrashort laser pulses and used for parallel microfabrication [54-72]. Figure 2.3.1 schematically demonstrates an experimental design of material processing using this method [72]. A single beam was divided into several by a diffractive beam splitter (DBS). After a lens 1 (L1) and an aperture array (AA), five of the beams ( $\alpha$ ,  $\beta$ ,  $\gamma$ ,  $\delta$ ,  $\epsilon$ ) were selected to generate an interference pattern at the Fourier plane of a lens 2 (L2).

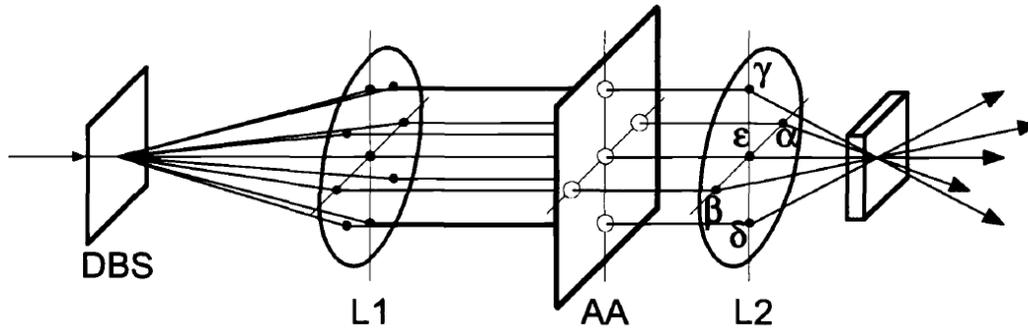


*Fig. 2.3.1: Experimental design of material parallel processing using the method of multi-beam interference. [72]*

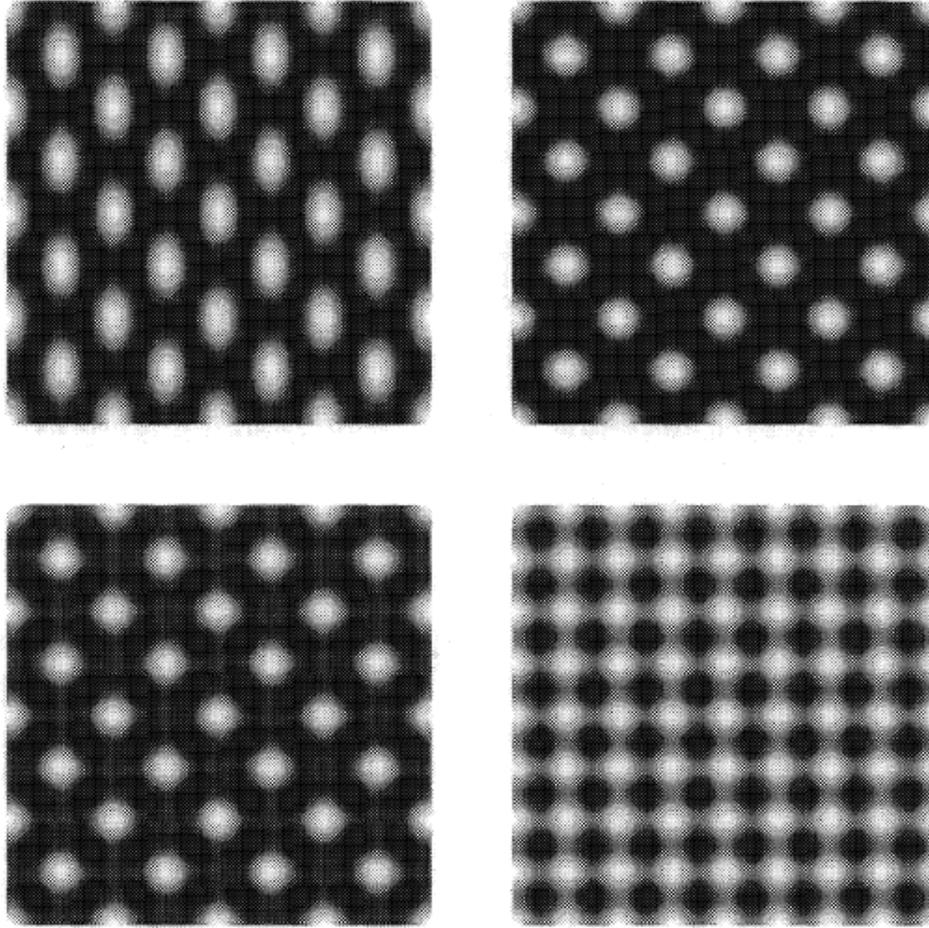


*Fig. 2.3.2: Calculated intensity profiles of 2D periodic patterns. [72]*

Due to interference, the intensity distribution  $I(\mathbf{r})$ , was theoretically calculated as:

$$I(\mathbf{r}) = \left\langle \left| \sum_i E_i(\mathbf{r}) \right|^2 \right\rangle \quad (2.3.1)$$

where  $E_i(\mathbf{r})$  is the electric field of each interference beam.  $I(\mathbf{r})$  can be a periodic pattern, as shown in figure 2.3.2. The fabricated results on a negative photoresist SU-8 are demonstrated in figure 2.3.3.

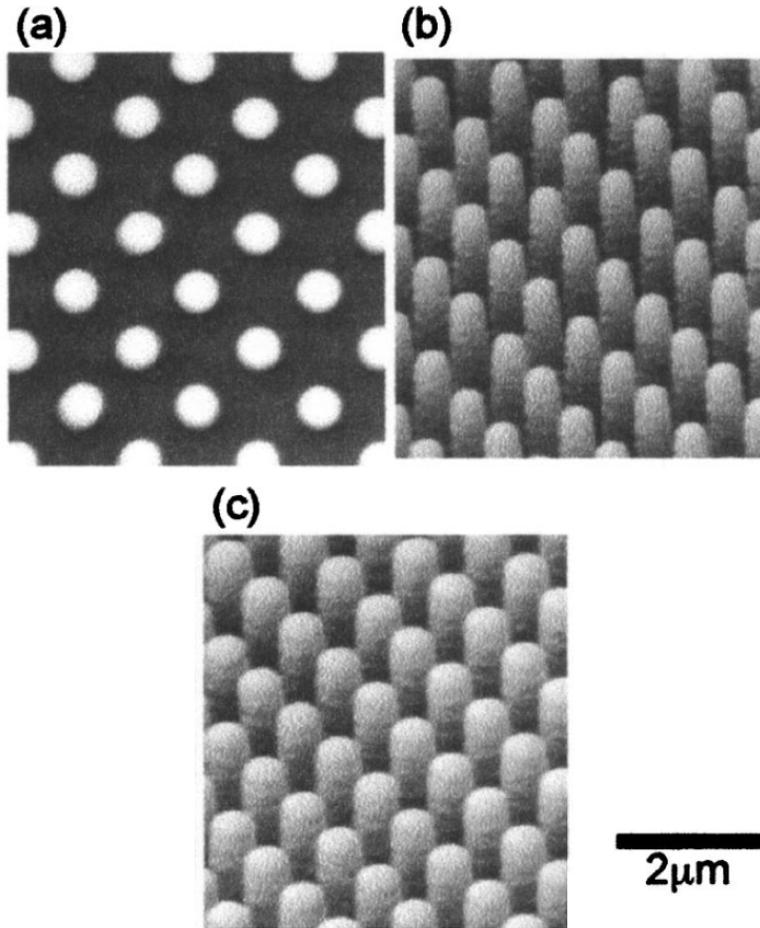


**Fig. 2.3.3:** Scanning electron microscopy (SEM) images of the structure fabricated by the multi-beam interference of ultrashort pulses. (a) Top view, (b) oblique view of the same sample, and (c) oblique view of another sample fabricated at larger exposure energy. [56]

Ultrashort pulse laser microfabrication of periodic structures using a microlens array (MLA) has also been demonstrated [73-79]. Figure 2.3.4 shows a basic scheme of the optical setup. Before an optical microscope, an MLA and a relay lens, L1, were placed in the optical path. The MLA allows multiple focuses at the plane A. The lens L1 and an objective lens project multiple focuses onto the sample surface using the optical microscope by adjusting the separation between the MLA and L1.

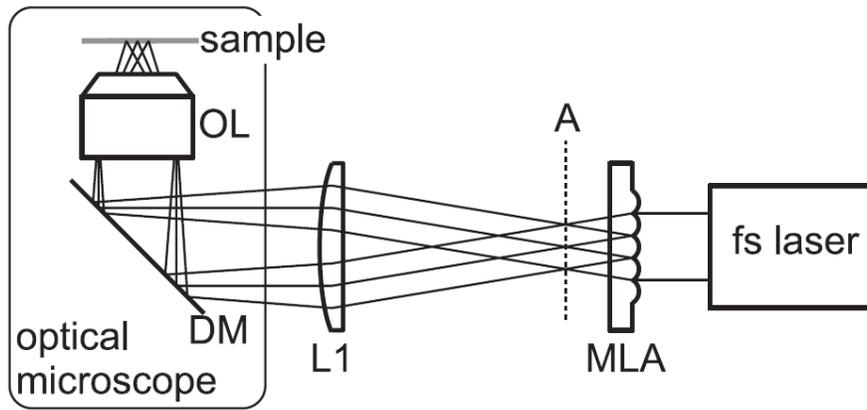


**Fig. 2.3.4:** Basic scheme of optical setup. MLA: microlens array, L1: lens, DM: dichroic mirror, OL: objective lens. A is the plane where multiple foci are generated.

[75]

Figure 2.3.5 shows an optical micrograph of the fabricated structure on the surface of a glass substrate using a femtosecond laser system ( $\tau_p \approx 130\text{fs}$ ) running at 1kHz repetition rate. Approximately  $10 \times 10$  dots were fabricated in a square pattern by laser surface ablation. The total input pulse energy was approximately  $120\mu\text{J}$  with 5s irradiation period. The pitch of the fabricated dots was about  $4.6\mu\text{m}$ .

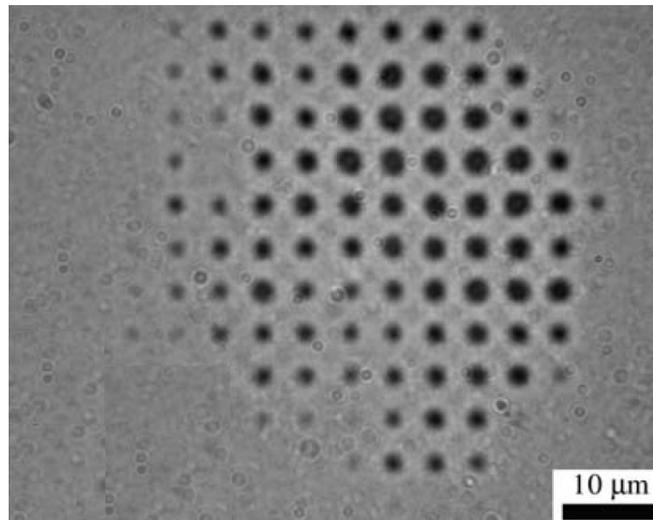


**Fig. 2.3.5:** An optical micrograph of the fabricated structure by MLA laser processing. [75]

### 2.3.2 Parallel microfabrication of arbitrary structures

Arbitrary multi-beam patterns can be generated by Diffractive Optical Elements (DOEs) which work as a hologram to modulate the input beam. With femtosecond laser pulses ( $\tau_p \approx 400\text{fs}$ ,  $\lambda = 800\text{nm}$ ), Y. Kuroiwa et al. successfully demonstrated both surface material ablation and internal structuring of a  $\text{SiO}_2$  glass sample using a DOE generated arbitrary multi-beam pattern [82], as shown in figure 2.3.6. The DOE, which had 4 phase levels and was designed with a wavelength of  $800\text{nm}$ , was made of  $\text{SiO}_2$  glass with  $\frac{1}{4}$  inch ( $6.35\text{mm}$ ) thickness and an effective area of  $8\text{mm} \times 8\text{mm}$ .

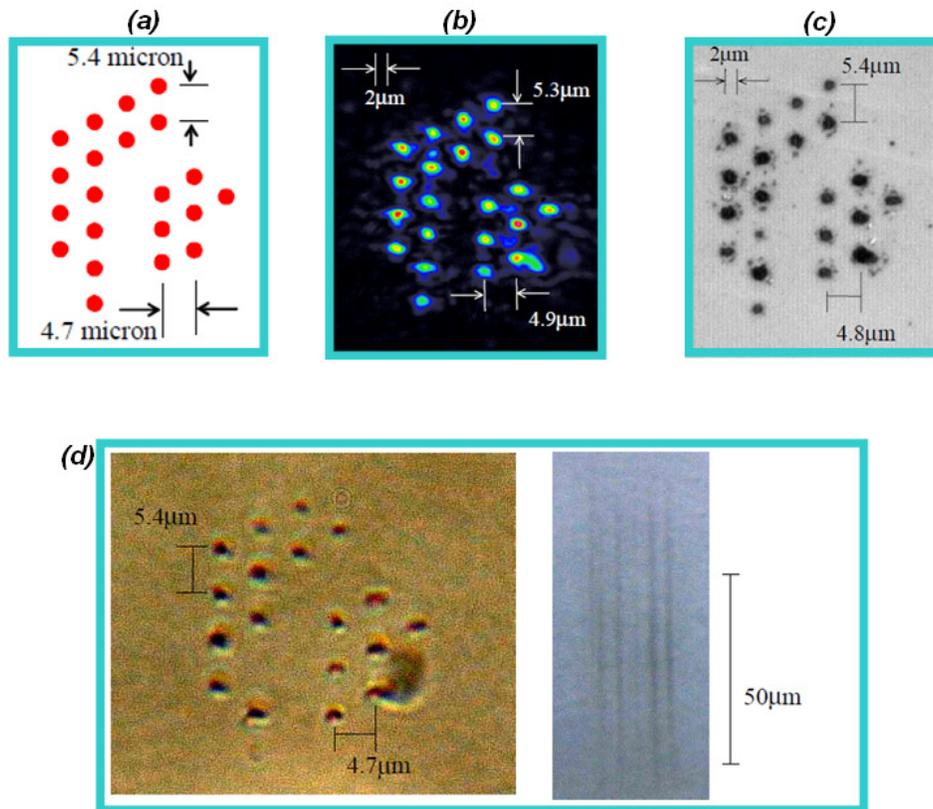


**Fig. 2.3.6:** The results showing the microstructuring using a DOE generated arbitrary multi-beam pattern. (a) The designed focal shape of the pattern, (b) The modulated beam profile, (c) Surface view of ablation pattern observed by optical microscopy, (d) Processed area inside the glass observed by optical microscopy, left: top view, right: side view.

As a dynamic diffractive optical element, a Spatial Light Modulator (SLM) has been employed to modulate femtosecond laser pulses and demonstrated material processing capable of parallel, arbitrary, and variable patterning - termed holographic processing [70].

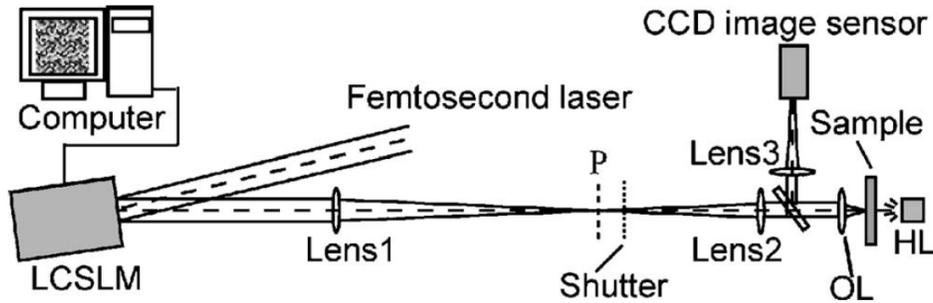


*Fig. 2.3.7: Experimental setup of the holographic femtosecond laser processing system.*  
[80]

Figure 2.3.7 shows the experimental setup of the holographic femtosecond laser processing system. The system consisted mainly of an amplified fs laser system and a liquid crystal SLM. The femtosecond laser system generated 150 fs pulses with mJ level energy at a wavelength of 800 nm. The pulse was diffracted at the SLM and formed a desired processing pattern at the Fourier plane P of Lens 1. The processing pattern was then reduced with Lens 2 and a 40 $\times$  microscope objective lens (OL) with a numerical aperture (NA) of 0.5 and was applied to a sample. The result is demonstrated in figure 2.3.8, where a pattern having 9 desired multiple beams was created by a Computer Generated Hologram (CGH) displayed on the SLM.

However, the use of a fixed hologram creating only 9 diffracted beams may not reach the industrial requirement of high throughput micro-structuring. Additionally, the

diffracted beams were not uniform, which can significantly degrade the machining quality. With these limitations in mind, the present study uses an SLM allowing mJ pulse energy input to variably create  $> 30$  uniform multiple beams with the demonstration of addressing CGHs in real time and synchronizing with a scanning method, which adds an additional flexibility for surface micro-structuring and shows potential applications for industry [88-91].

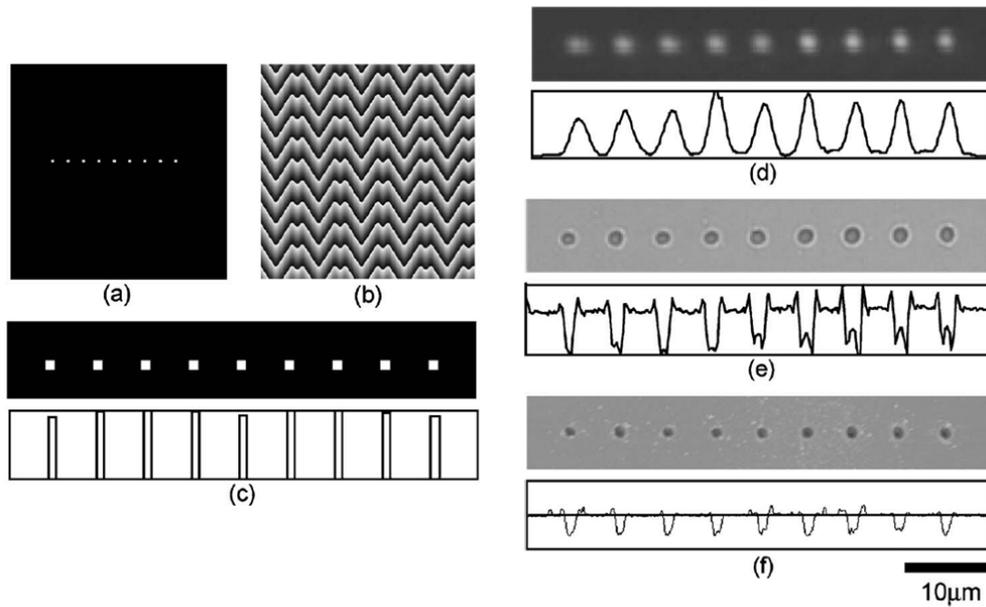


**Fig. 2.3.8:** (a) A target pattern for calculating a CGH, (b) the calculated CGH, (c) the computational reconstruction of the CGH, (d) the optical reconstruction of the CGH at the plane  $P$ , (e) a transmission microscope image, and (f) an Atomic Force Microscopy (AFM) image of the fabricated area. The vertical scale of the AFM profile is  $\pm 500$  nm. [80]

## 2.4 The generation of multiple beams using a Spatial Light Modulator (SLM)

### 2.4.1 Introduction to SLM technology

Figure 2.4.1 is a sketch showing how an SLM works, in which the input light is modulated by the hologram displayed on the SLM after reflection (a) or transmission

(b). The signal transmitting the holograms can be either optical or electrical, depending on the type of SLM. Electrically addressed reflective SLMs (ER-SLMs), Holoeye [92] LC-R 2500 and Hamamatsu [93] X10468 series, which will be introduced in Chapter 3, are employed in this research.

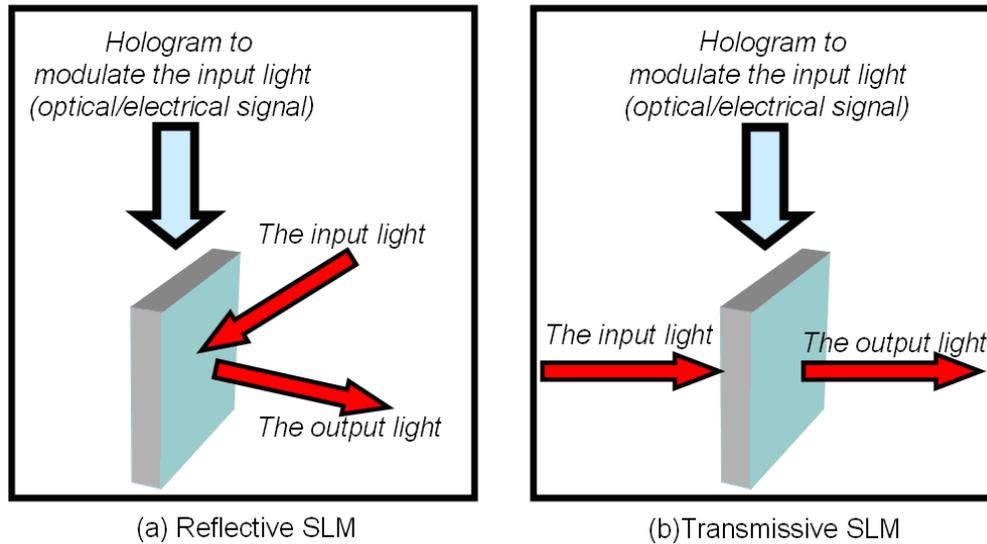


**Fig. 2.4.1:** The sketches demonstrate different types of SLM, reflective (a) and transmissive (b), and how they work.

Most of the ER-SLMs have a parallel-aligned nematic liquid crystal display (LCD), where holograms can be displayed. Figure 2.4.2 schematically shows the basic structure of the LCD. The Charge-Coupled Device (CCD) chip on the left of the figure, having a pixelated two dimension array structure with a given resolution, (1024×768 for Holoeye LC-R 2500 SLM [92]), is a device to electrically load the data from the Computer Generated Holograms (CGHs) which has the same resolution. After the data is transmitted, the required voltage is addressed onto each of the pixels to build up an electric field,  $E$ , leading to a series of changes in the corresponding liquid crystal (LC) e.g. a refractive index change,  $\Delta n$  [94-96]. As shown on the right of the figure, the input light firstly reaches a transparent protective glass, and then a

transparent electrode, normally made of indium tin oxide (ITO). Then, with a reflection on the mirror, the light goes through the liquid crystal for a second time. The phase of the output light is modulated mainly due to refractive index change of the LC,  $\Delta n$ , driven by the electric field,  $E$ .

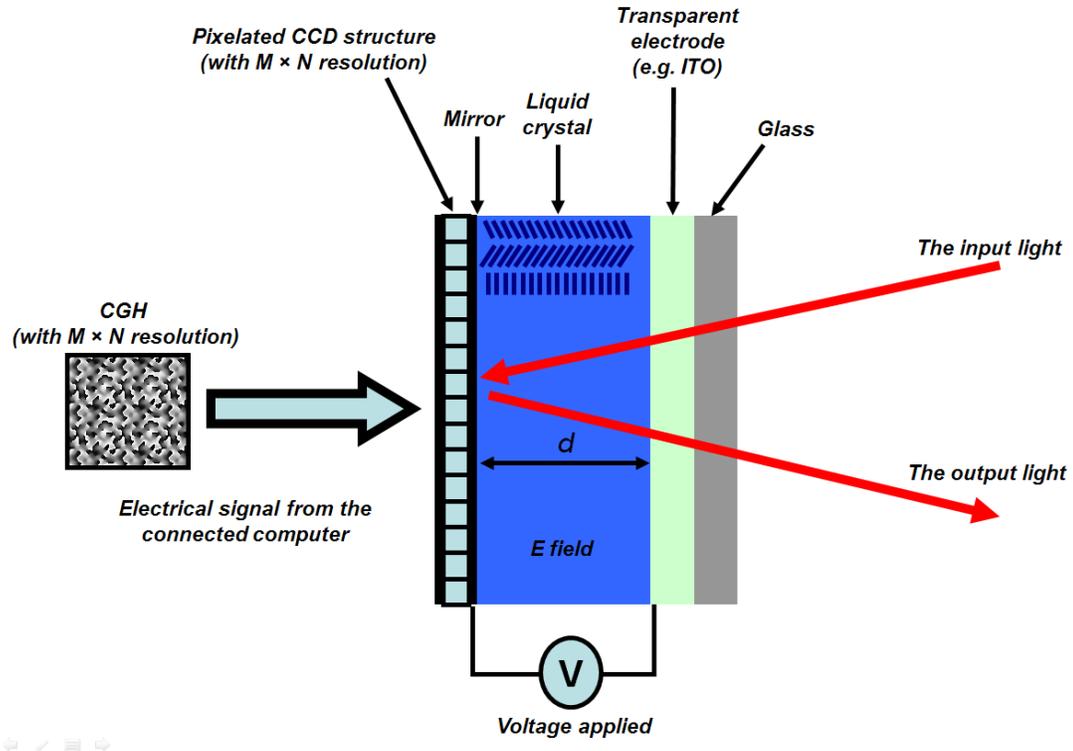


*Fig.2.4.2: The basic structure of an LCD.*

**(a) Phase modulation:**

In simple terms, the optical path difference ( $\delta$ ) and the phase change ( $\Delta\phi$ ) of the output light can be evaluated by the following equations:

$$\delta \approx 2\Delta nd \quad (2.4.1)$$

$$\Delta\phi = k \cdot \delta \approx \frac{2\pi}{\lambda} 2\Delta nd = \frac{4\pi}{\lambda} \Delta nd \quad (2.4.2)$$

where  $k$  and  $\lambda$  are the wave number and wavelength of the input light respectively,  $\Delta n$  is the change of refractive index, and  $d$  is the thickness of the LC. As mentioned,  $\Delta n$  is a function of the voltage ( $v$ ), i.e.  $\Delta n = f(v)$ . Thus:

$$\Delta\varphi \approx \frac{4\pi}{\lambda} d \cdot f(v) \quad (2.4.3)$$

Since the commercial SLM displays 8 bit CGH, where the change of voltage driven by the CCD pixels has  $2^8 = 256$  levels, normally symbolized by the 0 – 255 grey levels, the phase change ( $\Delta\varphi$ ) is a function of the grey level. The graph of  $\Delta\varphi$  versus grey level as shown in Figure 2.4.3 (which is from the measured results of the Holoeye LC-R 2500 SLM with  $\lambda = 632.8\text{nm}$  linearly polarized laser input [97]), demonstrates near linear increase of the phase modulation by changing the grey level from 0 to 255.

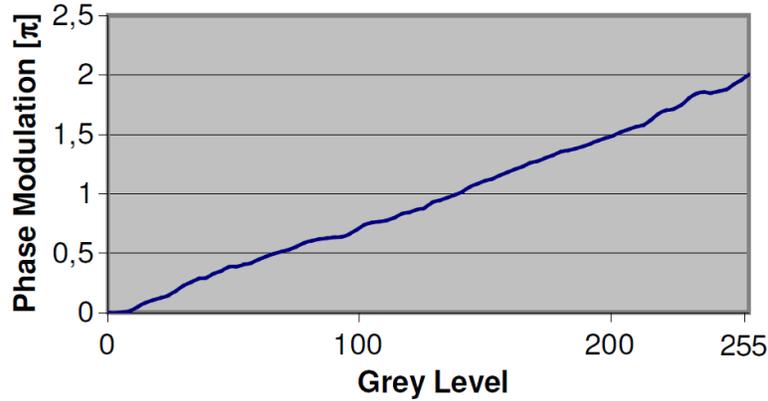


*Fig. 2.4.3: The measured results from a Holoeye LC-R 2500 SLM with  $\lambda = 632.8\text{nm}$  linearly polarized laser input, showing a near linear increase of the phase modulation with increasing the grey level (from 0 to 255).*

**(b) Intensity modulation:**

The polarization of the output light is also changed by the voltage, i.e. the grey level. So, with the setup shown in Fig. 2.4.4, (where two polarizers, P and A, with perpendicular polarisation direction, are installed before the incoming light and after

reflecting the SLM, respectively), intensity modulation can be obtained. The intensity measured after the analyser (A) depends on the grey level driving the voltage through the CCD pixels to twist the LC cells.

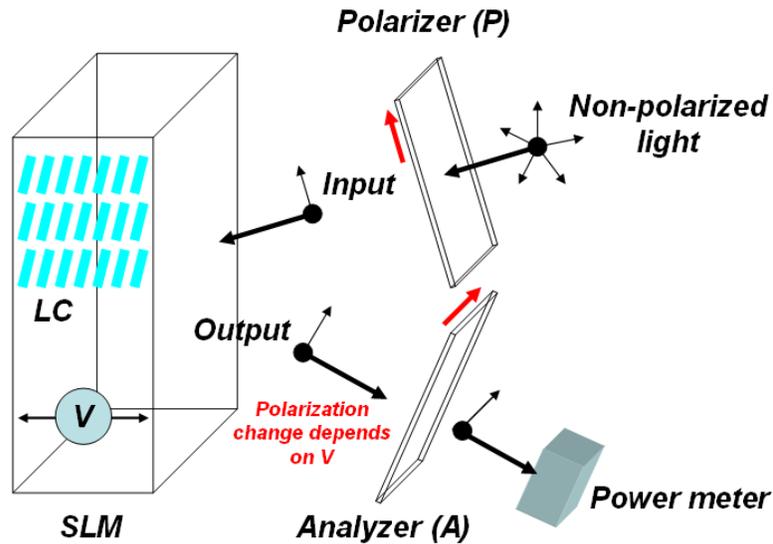


*Fig. 2.4.4: The setup for intensity modulation*

Overall, as shown in figure 2.4.5, an SLM is able to modulate both the phase ( $\varphi_0$ ) and the amplitude ( $A_0$ ) of the input light by applying the appropriate CGHs.

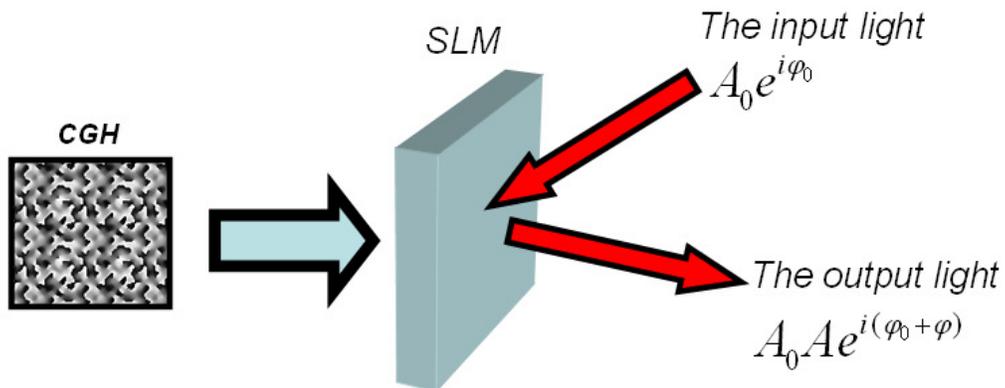


*Fig.2.4.5: How an SLM works – modulation to the phase/intensity of the light*

### 2.4.2 Generation of multiple beams with an SLM

With an SLM, phase holograms can be widely used to generate multiple beams for different applications from multi-trapping of micro-particles in optical tweezers [98-113] to ultrashort pulse laser material micro-processing [82-91]. In addition, intensity holograms have some other applications, such as laser beam shaping where the hologram works as an intensity mask to modulate the intensity distribution of the input laser beam [114, 115].

Generally speaking, according to a positional relationship between the hologram and the target, the phase holograms used to generate multiple beams can be classified into three different types.

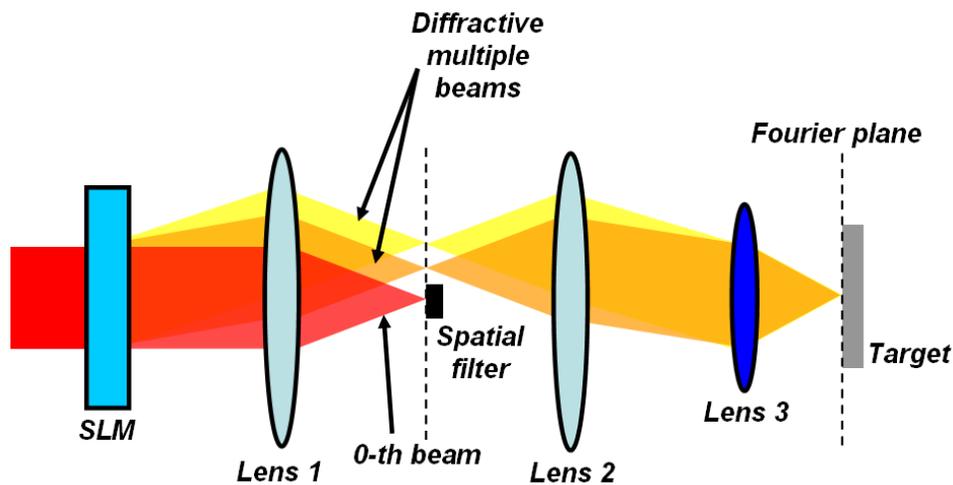


*Fig. 2.4.6 (a): Creation of multiple beams with Fourier Plane Hologram.*

The first type is the Fourier Plane Hologram, as named by the current author, because the target is put on the Fourier plane of the hologram, as shown in figure 2.4.6 (a). Here, lens 1 and lens 2 form a  $4f$ -imaging optical system, used to block the undiffracted zero order (0-th) beam with a spatial filter, and lens 3 is actually used to

focus the diffracted multiple beams at the Fourier plane for the application. Based on a Fourier transform, the iterative Gerchberg-Saxton (GS) algorithm [117] is widely used in various applications from holographic optical tweezers [98-102] to ultrashort pulse laser parallel microprocessing [80] and is probably the most popular method to calculate this type of CGH. An algorithm with a non-iterative approach, known as the superposition of prisms, was first published by J. Liesener et al. [103] and is another method to generate a Fourier Plane Hologram. This has demonstrated some improvements over the GS algorithm, particularly in the calculation speed [118]. Both of the above algorithms have been employed in the current study.

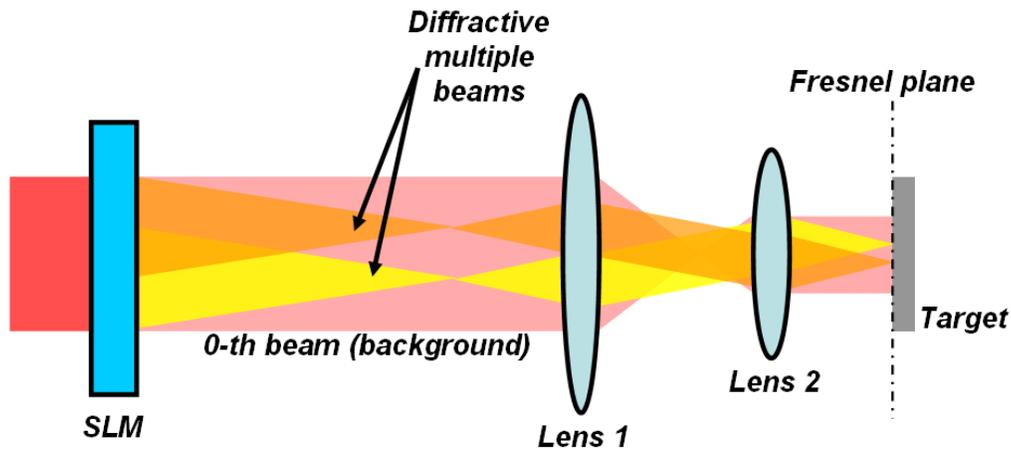


*Fig. 2.4.6 (b): Creation of multiple beams with a Fresnel Plane Hologram.*

The second type of hologram considered is the Fresnel Plane Hologram, where the target is put on the Fresnel plane of the hologram. Figure 2.4.6 (b) demonstrates the positional relationship between this hologram and the target. Here the diffracted beams are focused on the Fresnel plane by the hologram, with lens 1 and 2 employed as a telescope system. The un-modulated zero order beam is in the background of the diffracted peaks, with no influence on the irradiation of the target. The multiplexed Phase Fresnel Lenses Hologram, first attempted by Hasegawa et al. [81, 86] to

generate multiple focused peaks for holographic femtosecond laser processing, is a typical Fresnel Plane Hologram application.

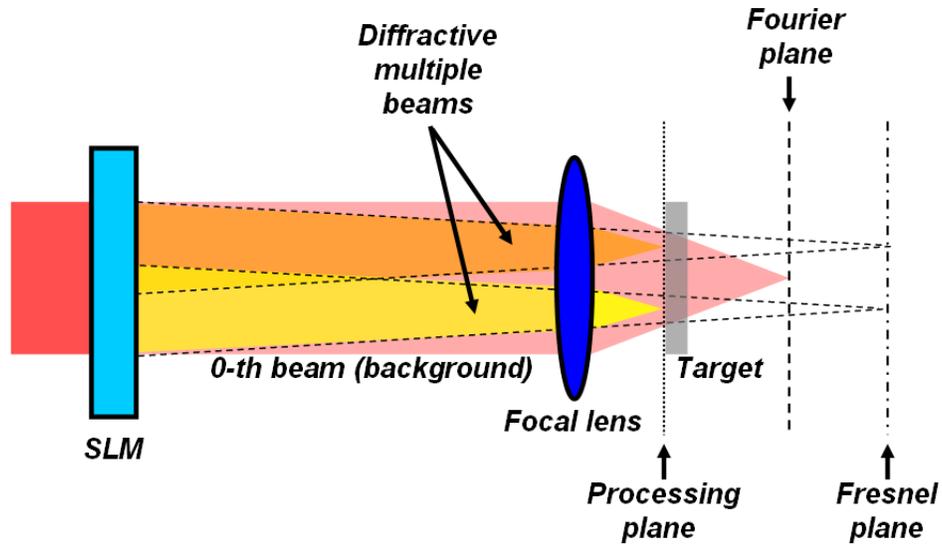


*Fig. 2.4.6 (c): Creation of multiple beams with the third type of hologram - the Fourier and Fresnel plane hologram.*

The third hologram type is the combination of the Fourier and Fresnel plane holograms. As illustrated in the figure 2.4.6 (c), with this type of hologram, the target is put on a plane, which is neither the Fourier nor the Fresnel plane, but the place where the multiple diffractive beams focus. Since the zero order beam is defocused on the target plane, this type of hologram can be used to avoid the unwanted effects caused by the zero order beam (Chapter three). [90]

## 2.5 The calculation of Computer Generated Hologram (CGH) algorithms

### 2.5.1 CGH calculation algorithms summary

An optical beam can be represented by a complex field,  $\Psi$ , which can be written as:

$$\psi_0 = A \exp(i\phi_0) \quad (2.5.1)$$

The modulus  $A$  is the amplitude of the field and  $\varphi$  is the phase. The phase holograms act as a transmission,  $t$ , mathematically expressed as the following (2.5.2), which therefore modifies only the phase of the beam.

$$\psi_t = \exp(i\varphi_h) \quad (2.5.2)$$

When the beam given by equation 2.5.1 is incident on the SLM, the complex amplitude profile of the beam after the modulation of the phase hologram will be:

$$\psi_h = \psi_0 \cdot \psi_t = A_0 \exp[i(\varphi_0 + \varphi_h)] \quad (2.5.3)$$

The algorithms which will be described in this section are used to generate this phase pattern  $\varphi_h$ .

### 2.5.1.1. Algorithms for calculating Fourier Plane Holograms

The Fourier plane phase hologram is designed such that when the modified beam,  $\psi_h$ , is focused by a lens, the light intensity distribution in the image space (at the focus of the lens) is the one desired, e.g. multiple focused spots at prescribed positions.

According to Fourier optics, there is a Fourier transform relationship between the complex field,  $\psi_h$ , in the pupil plane of the focal lens, onto which the plane of the SLM is imaged, and the complex field,  $\psi_i$ , at the focus of the lens in image space, shown as the following expression:

$$\psi_i(x_i, y_i) = FT\{\psi_h(x_h, y_h)\} \quad (2.5.4)$$

The image space field can therefore be thought of as a scaled version of the far-field diffraction pattern that would be produced by the beam leaving the SLM. If one of  $\psi_h$  or  $\psi_i$  is known, it is straightforward to calculate the other unknown field by taking the forward or inverse Fourier transform of the known field, as shown in figure 2.5.1. The algorithms to be introduced in the following are the means of calculating the phase

hologram for a desired far-field intensity pattern, e.g. a certain number of multiple beams with the arbitrary geometry for multiple beam applications.

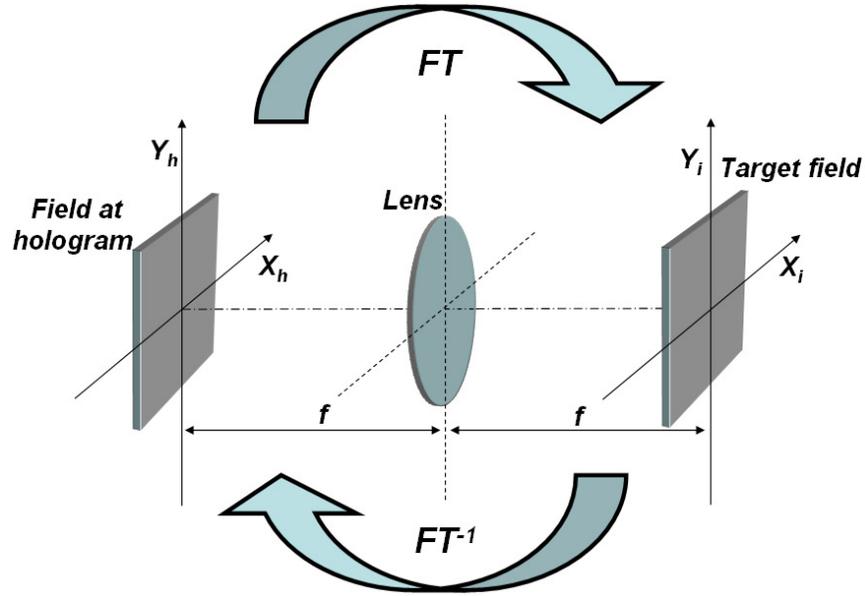


**Fig. 2.5.1:** Fourier relationship between the plane of the hologram and the image space of the focal lens.

#### (a) Iterative Gerchberg-Saxton (GS) Algorithm

As mentioned, with its wide applications from holographic optical tweezers to ultrashort pulse laser parallel microprocessing [80, 99, 116], the Fourier-transform-based GS algorithm, first published by R. W. Gerchberg and W. O. Saxton in 1972 [117], is one of the most popular methods to calculate Fourier plane CGHs.

The GS algorithm can be used to calculate the phase required in the hologram plane to produce a predefined intensity distribution in the focal plane of the lens. The target intensity distribution is defined in the image space as  $I_t(x_i, y_i)$ , and the aim is to find  $\varphi_h(x_h, y_h)$  such that  $(FT \{ \exp(i\varphi_h) \})^2 = I_t$ . To find the desired phase  $\varphi_h$ , the algorithm starts at the hologram plane with a random  $\varphi_r$  and constant unit amplitude. Therefore, for the first iteration step, the light field in the hologram plane is:

$$\psi_{h,1} = \exp(i\varphi_r) \quad (2.5.6)$$

For the first and subsequent iteration, the light field is propagated to the image space by taking its Fourier transform, i.e., for the  $k$ th iteration:

$$\psi_{i,k} = FT\{\psi_{h,k}\} \quad (2.5.7)$$

Then, the light field in the image space is modified by keeping the phase but replacing the intensity with the target intensity,  $I_t$ :

$$\varphi_{i,k} = \arg(\psi_{i,k}) \quad (2.5.8)$$

$$\psi_{i,k}' = \sqrt{I_t} \exp(i\varphi_{i,k}) \quad (2.5.9)$$

The resulting light field is then propagated back to the hologram plane by taking its inverse Fourier transform:

$$\psi_{h,k}' = FT^{-1}\{\psi_{i,k}'\} \quad (2.5.10)$$

The iteration is finally completed by again keeping the phase but replacing the intensity with uniform constant intensity:

$$\varphi_{h,k+1} = \arg(\psi_{h,k}') \quad (2.5.11)$$

$$\psi_{h,k+1} = \exp(i\varphi_{h,k+1}) \quad (2.5.12)$$

Since the laser beam has a Gaussian intensity profile, it is sometimes desirable to replace the intensity with the Gaussian profile. With a few iterations, say  $n$ , the algorithm converges such that the argument of the light field at the hologram plane is the phase required to produce the target field in image space.

$$\varphi_{h,n} = \arg(\psi_{h,n}) \quad (2.5.13)$$

The diagram in figure 2.5.2 graphically shows how to generate a phase hologram with the GS Algorithm. The calculation starts from the upper left corner, and moving clockwise runs through the forward/inverse Fourier transforms by replacing the initial intensity distribution with a target intensity distribution but keeping the initial phase at

the bottom right corner. As described in the iterative approach above, the phase hologram can be finally generated at the bottom left corner after several loops.

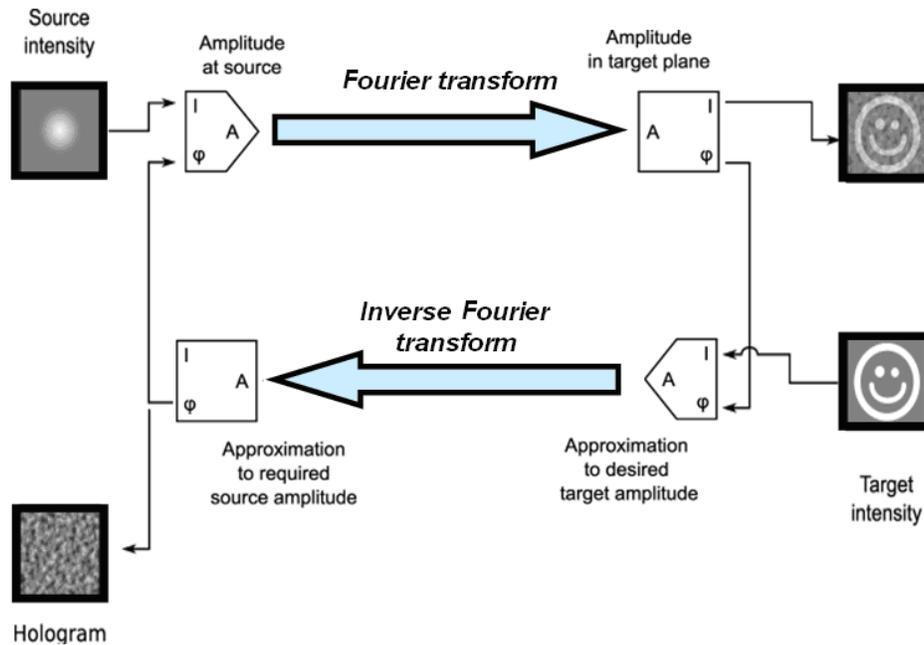


**Fig. 2.5.2:** The diagram graphically shows how to generate a phase hologram with the GS Algorithm. [119]

The GS algorithm can be used not only to generate multiple focussed spots of light but also arbitrary two-dimensional intensity distributions. Extended by Haist et al. (1997) [120], the GS algorithm has been demonstrated to modulate the intensity distributions in several planes simultaneously. Later, Sinclair et al. (2004) [99] have successfully applied this algorithm in holographic optical tweezers, simultaneously trapping several objects in individually controllable arbitrary three-dimensional positions. This algorithm takes advantage of the phase freedom and iteratively optimizes the focal-plane intensity distribution by varying both these phase values and  $\phi_h$ . In contrast, a simpler and computationally faster non-iterative algorithm, the complex superposition of prisms (and lenses for 3D patterns) [102, 103], is introduced in the next section, where the phase between each diffracted beam is fixed.

**(b) Non-iterative complex superposition of prisms (and lenses) algorithm**

First introduced by J. Liesenser [103], the non-iterative complex superposition of prisms (and lenses for 3D patterns) algorithm, may be the simplest and computationally fastest method to calculate phase CGHs for the generation of multiple beams.

As shown in figure 2.5.3, combining the phase of basic optical components, prisms or gratings (resulting in lateral shifts) and lenses (producing axial shifts), the algorithm, sometimes called the Lenses and Gratings (LG) algorithm [102], can generate three dimensional arbitrary multiple beam patterns in the imaging space after a focal lens.

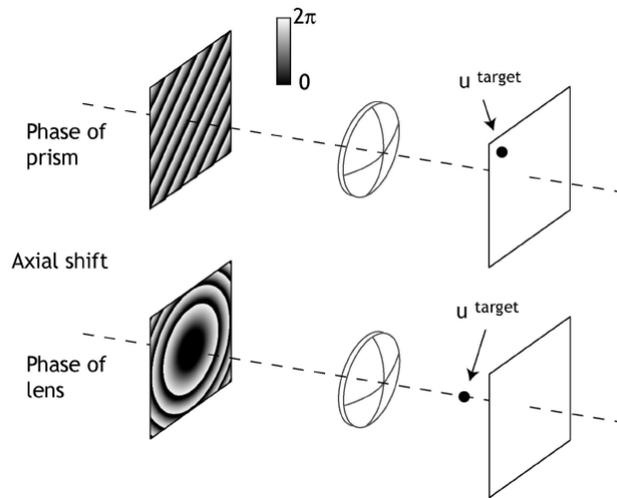


**Fig.2.5.3:** Phase required for lateral and axial shifts. [102]

It is known that a single beam with planar phase fronts at the plane of the hologram, i.e.,  $\varphi_h = \text{constant}$ , corresponds to a single focussed spot in the image space. If the hologram plane has an inclined phase front, the spot in the image space will be laterally displaced from the optical axis. This is equivalent to passing the light through a prism with a small angle that introduces a linearly increasing phase delay  $\varphi_{prism}$

across the beam. The phase at the hologram plane required to produce a lateral shift  $(\Delta x, \Delta y)$  in the position of the focused spot is given by:

$$\varphi_{prism}(x_h, y_h) = \alpha(\Delta x x_h + \Delta y y_h) \quad (2.5.14)$$

where  $\alpha$  is a coefficient that depends on the imaging characteristics and wavelength.

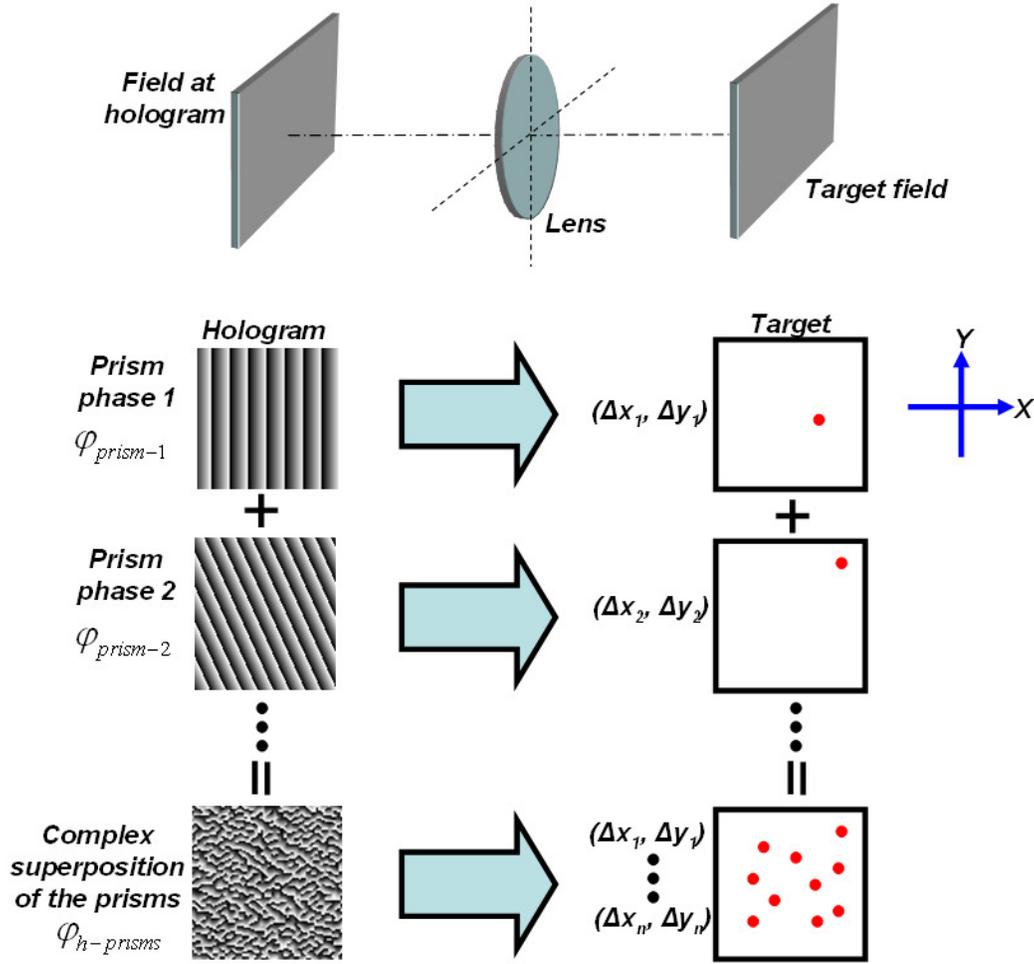


**Fig. 2.5.4:** 2D arbitrary multiple laser beam pattern generated by complex superposition of prism phases.

To generate two dimensional arbitrary multiple beam patterns at the focal plane of the lens, the phase at the hologram plane,  $\varphi_h$ , should be the complex superposition of the prism phases, each of which shifts a focused spot onto one of the requested positions,  $(\Delta x_i, \Delta y_i)$ , as shown in figure 2.5.4, Accordingly,  $\varphi_h$  can be expressed as:

$$\varphi_h = (\varphi_{prism-1} + \varphi_{prism-2} + \dots + \varphi_{prism-n}) \bmod 2\pi = \left( \sum_{i=1}^n \varphi_{prism-i} \right) \bmod 2\pi \quad (2.5.15)$$

To also axially shift each of the focal spots in the image space, an additional lens phase should be added, hence obtaining multiple beam patterning in three dimensions.

The lens phase can be given as:

$$\varphi_{lens}(x_h, y_h) = -\frac{k}{2f}(x_h^2 + y_h^2) \quad (2.5.16)$$

where  $f$  is a function of the axial shift distance and  $k = 2\pi / \lambda$  is the wave number of the light. This is equivalent to passing the light through an additional lens with focal length,  $f$ . With both prism and lens phases added, the focussed spots are displaced not only laterally and but also axially, i.e. three-dimensionally. The phase of the beam at the hologram plane is required to be the (modulus  $2\pi$ ) sum of  $\varphi_{prism}$  and  $\varphi_{lens}$ :

$$\varphi_h' = \left[ \sum_{i=1}^n (\varphi_{prism-i} + \varphi_{lens-i}) \right] \bmod 2\pi \quad (2.5.17)$$

Clearly, without iterative calculation, the GL algorithm is simple and computationally fast. With a standard personal computer, the hologram calculation speed can meet the requirement of real time change in multiple beam patterns. The literature demonstrates dynamic CGHs calculation to two/three dimensional trapping and manipulation of micro/nano particles by optical tweezers with this algorithm [99, 104-105].

However, the diffraction efficiency,  $\eta$  (the ratio of the energy of the light directed to the requested positions to the total energy input) and the uniformity of the diffracted multiple beams may be low, especially for a pattern with symmetric geometry, due to the high possibility that one or more ghosts overlap with the desired diffractive (+1) order beams - a process called 'degeneracy' [118]. In most cases, the ghosts are the

higher order diffractive peaks produced by the phase gratings, i.e. the prism phases. As introduced, a phase grating, equivalent to a prism, deflects an enhanced +1 order beam to a required position  $(\Delta x_i, \Delta y_i)$ , by imposing an appropriate phase  $\varphi_{prism}$ ; however, it also generates other diffractive orders (e.g. -1 order) with much lower intensity. For the GL algorithm, the phase between each multiple beam is fixed, without any freedom to avoid the ghosts overlapping with the desired diffractive +1 orders, hence causing the high possibility of degeneracy.

Probably due to this high possibility of low diffraction efficiency and poor beam uniformity, the GL algorithm is not usually used to generate multiple beams for high precision ultrashort pulse laser processing. The current author is the first to attempt parallel micro-processing using ultrashort pulse laser with diffracted multiple beams generated by the GL algorithm. With the considerations of spectral bandwidth of the laser source (Chapter 4 & 5) and the geometric pattern design of multiple beams (Chapter 6), the results shown and discussed in this thesis, have also demonstrated high diffraction efficiency and excellent beam uniformity, compared with those produced by the time-consuming GS iterative algorithm.

### **2.5.1.2. Multiplexing Phase Fresnel Lenses (MPFL) algorithm for calculating Fresnel Plane Holograms**

#### ***(a) Multiple foci reconstructed in Fresnel diffraction field***

With Fresnel plane holograms, the desired multiple-beam pattern is reconstructed in the Fresnel diffraction field. In terms of the distance away from the aperture, the diffraction of light can be categorized into Fresnel diffraction (near field diffraction) and Fraunhofer diffraction (far field diffraction). As shown in figure 2.5.5, diffraction

takes place after the plane waves from a very distant point source,  $S$ , passing through a single small aperture on an opaque shield,  $\Sigma$ . Imagine that we have an observation plane,  $\sigma$ , parallel with  $\Sigma$ . If  $\sigma$  is very close to  $\Sigma$ , at the geometric projection field, an image of the aperture is projected onto the screen which is clearly recognizable despite some slight fringing around its periphery. As  $\sigma$  moves further away from  $\Sigma$ , reaching the Fresnel diffraction field, the image of the aperture becomes increasingly more structured as the fringes become more prominent. When  $\sigma$  is in Fraunhofer diffraction field, a very great distance from  $\Sigma$  (after  $L_2$ ), the projected pattern has little or no resemblance to the actual aperture due to the Fourier transform.

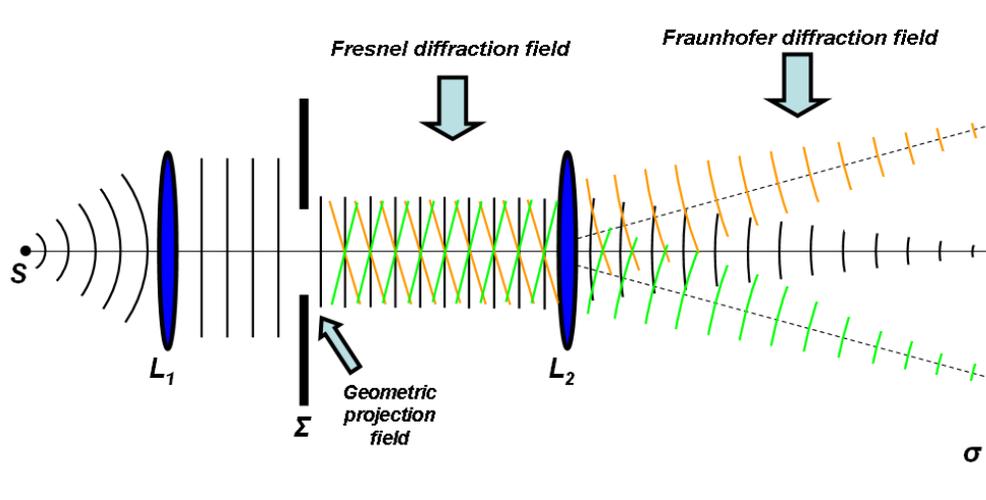


**Fig 2.5.5:** *Fresnel (near field) diffraction and Fraunhofer (far field) diffraction.*

As described in Part A, to reconstruct the multiple foci generated by the Fourier plane hologram, a focal lens is needed to perform the Fourier transform. With the Fresnel plane hologram, the focal lens is not necessary, since the desired multiple foci are reconstructed in the Fresnel diffraction field, as shown in figure 2.5.6.

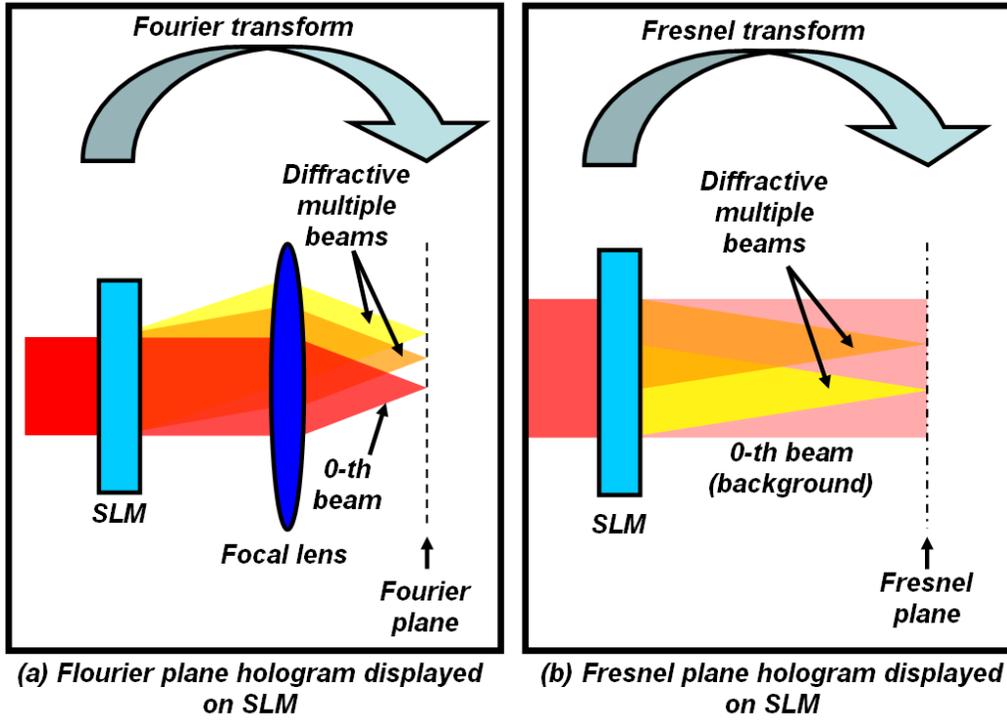


*Fig. 2.5.6: Comparison of the reconstructive plane of multiple foci using Fourier (a) and Fresnel (b) plane hologram.*

**(b) Multiplexing Phase Fresnel Lenses (MPFL) algorithm**

The use of the Multiplexing Phase Fresnel Lenses (MPFL) algorithm, used to calculate Fresnel plane holograms, was first attempted by S. Hasegawa et al. [81, 83] to generate multiple beams for parallel femtosecond laser processing.

It is known that the complex amplitude of a phase Fresnel lens (PFL) is given by:

$$\psi_{PFL}(x, y) = \exp(ik \frac{(x-x_i)^2 + (y-y_i)^2}{2z_i}) \quad (2.5.18)$$

where  $z_i$  is a focal length and  $k = 2\pi / \lambda$  is the wave number. With this phase Fresnel lens, the light can be focussed at  $(x_i, y_i, z_i)$  in the Fresnel diffraction field. Accordingly,

the MPFL which can generate  $n$  multiple foci, three dimensionally arranged in the Fresnel diffraction field, is expressed as:

$$\psi_{h-MPFL}(x, y) = \sum_i^n \exp(ik \frac{(x-x_i)^2 + (y-y_i)^2}{2z_i} + i\phi_i) \quad (2.5.19)$$

where the amplitude is set to 1 and  $\phi_i$  is the centre phase. The diffraction peaks are made uniform by changing the centre phase and size of each phase Fresnel lens while taking account of the intensity distribution of the irradiated laser pulse and the spatial frequency response of the SLM [81].

With the phase hologram calculated by the MPFL algorithm, 2D and 3D parallel femtosecond laser processing with single-pulse irradiation has been demonstrated [81, 83]. This may be useful to fabricate microstructures inside a material and on an arbitrary-shaped material surface. However, parallel processing with diffracted multiple beams reconstructed at the Fresnel plane might not work well for a large area surface micro-structuring application, due to the small diffractive angle allowing only a small area to be fabricated.

### 2.5.2 Calculation of CGHs with a LabVIEW program

A user-friendly interactive LabVIEW program has been developed by the optical group at University of Glasgow for the application of holographic optical tweezers [102]. The program can dynamically calculate Fourier plane holograms to create and individually control the diffracted multiple beams, which, in this case, is used for trapping and manipulating the micro particles.

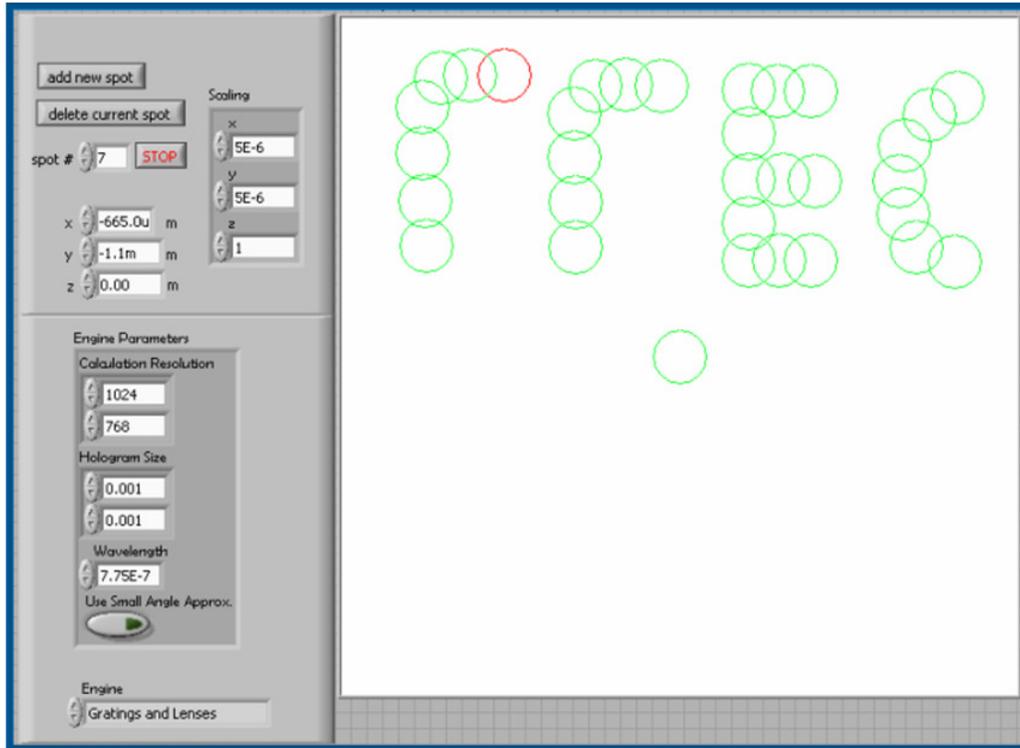


**Fig.2.5.7:** The interface of the LabVIEW program generated by Leach et al. [102]

Basically, the program consists of three main parts. Figure 2.5.7 shows the first part of the program, the interface, where the user can specify the number of traps and the trap coordinates,  $(x, y, z)$ , which is relative to the focal position in Fourier diffraction field. As shown, the interface contains an area that represents the trapping plane of the optical tweezers. Users can easily change the coordinates of each trap by clicking and dragging the cursor on the target trap within this area, or numerically entering the coordinates. After receiving the coordinates of each trap from the interface, the program starts to calculate the corresponding Fourier plane hologram by the chosen algorithm in the second part of the program, the calculation engine, in which many algorithms has been included, e.g. Gerchberg-Saxton and Grating and Lenses. When the calculation stops, the hologram design is passed to the final part of the program, which displays the calculated hologram pattern on the SLM. Figure 2.5.8 (a)

demonstrates a hologram generated by this program using the Grating and Lenses algorithm, whose computational reconstruction is given in figure 2.5.8 (b).

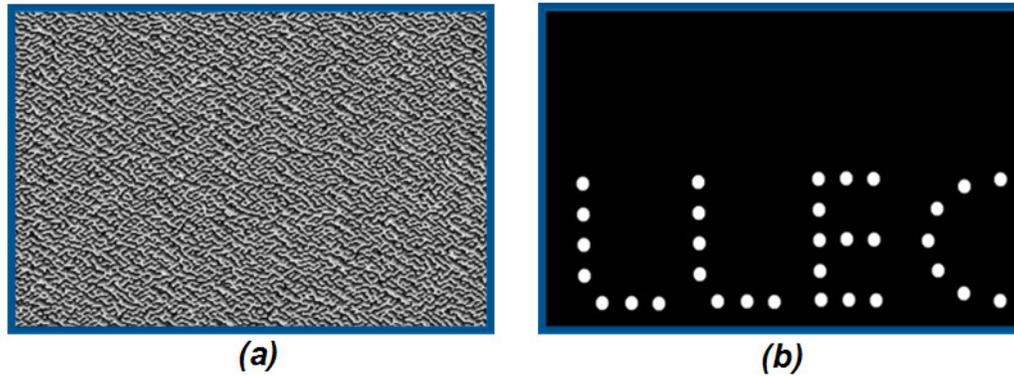


*Fig.2.5.8: A CGH calculated by the program (a) and its computational reconstruction (b).*

This LabVIEW program has been used to calculate appropriate Fourier plane holograms for the current research. More details about this will be given in the following Chapters.

## 2.6 Summary

This chapter starts with a brief introduction of ultrashort pulse laser systems and its material processing. Previous studies demonstrating the great advantages of ultrashort pulse lasers micro-processing over CW and long pulse lasers are reviewed, while the results from literature, showing the main drawback of ultrashort pulse laser material processing are also highlighted. This drawback is the low processing efficiency and throughput, mainly due to the significant energy wasted by severely attenuating the mJ level output to meet the requirement of  $\mu\text{J}$  level pulse energy (just a little above the material's ablation threshold) for high precision micro-machining.

As dynamic diffractive optical elements, Spatial Light Modulators (SLM) has been recently used to generate multiple beams for multi-trapping of micro-particles in optical tweezers, and have demonstrated for parallel material micro-processing. The following chapters discuss the algorithms used to calculate proper Computer Generated Holograms (CGH) which can transform the incident beam intensity distribution, i.e. Gaussian, into the desired multiple beam patterns.

## **Chapter 3**

# **Experimental Equipment and Techniques**

### **3.1 Introduction to experimental**

This chapter will firstly introduce the main equipment employed for current research, including the ultrashort pulse laser systems, Spatial Light Modulators (SLMs), scanning galvanometer systems and multi-axis motion control systems. Results on the equipment test are also discussed.

After introducing this main equipment, the methods to eliminate the zero order beam, which otherwise might cause unwanted surface damage, will be discussed and followed by the introduction of experiment setups.

### **3.2 Principal experimental apparatus used for the research**

#### **3.2.1 Ultrashort pulse laser systems**

##### **3.2.1.1 Clarke-MXR CPA2010 femtosecond laser system**

A femtosecond laser system, Clark-MXR CPA2010, has been used to generate ultrashort laser pulses for the present research. The CPA2010 is a compact, integrated Ti:Sapphire amplified laser system, which is physically comprised of a laser head, a ORC-1000 power supply, a DT-505 Pockels cell driver, and a temperature stabilization unit, as shown in figure 3.2.1.

Similar to most of the other ultrashort pulse laser systems, the CPA2010, which contains many subcomponents in its bi-level laser head, is more complicated, compared to CW and long-pulse laser systems. Figure 3.2.2 schematically demonstrates the layout of CPA2010's bi-level laser head. Chirped pulse amplification (CPA), where the pulse duration manipulation is involved with the pulse

stretcher and compressor setting before and after a Ti:Sapphire regenerative amplifier respectively, is adopted, as introduced in 2.2.1.2.

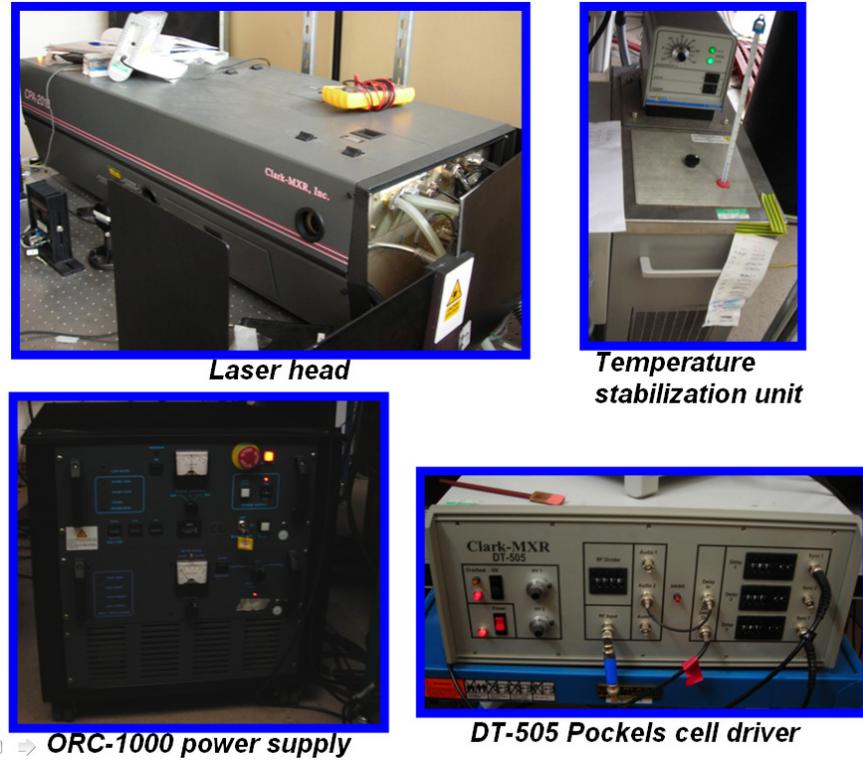


*Fig. 3.2.1: Clark-MXR CPA2010 femtosecond laser system*

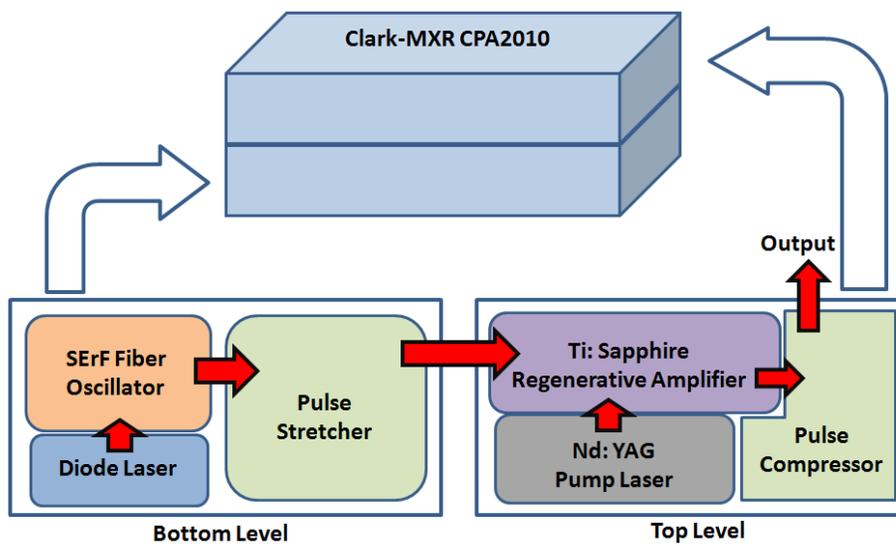


*Fig. 3.2.2: CPA-2010 bi-level laser head schematic layout*

The oscillator, schematically demonstrated in figure 3.2.3, is based on a unidirectional, polarization rotation additively pulse mode-locked (APM) fibre laser, which uses Erbium doped fibre (SErF) as the active medium [121]. Pumped by an all solid-state fibre-coupled laser diode operating at approximately 980nm, the SErF fibre laser generates initial seed pulses at the wavelength of 1500nm [122]. By going through a second harmonic generator, a BBO (Beta-barium borate) crystal, the frequency of the pulses is doubled, hence generating a new wavelength of 775nm for further amplification. The stretched seed pulse is then amplified in the Ti:Sapphire regenerative amplifier, pumped by a Nd:YAG laser with a ORC-1000 flash lamp. Finally, through the pulse compressor, which can be misaligned to generate longer output pulse duration as mentioned in 2.2.1.2, the output laser pulse can reach approximately 1mJ pulse energy with minimum 180fs pulse duration.

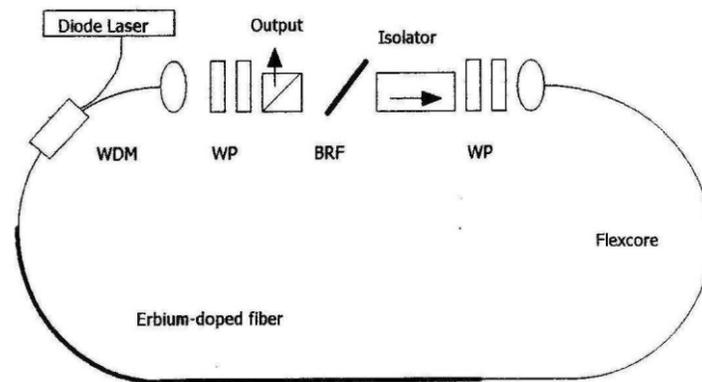


**Fig. 3.2.3:** The schematic of the fibre oscillator. WP denotes waveplates and BRF denotes birefringent filter. [121]

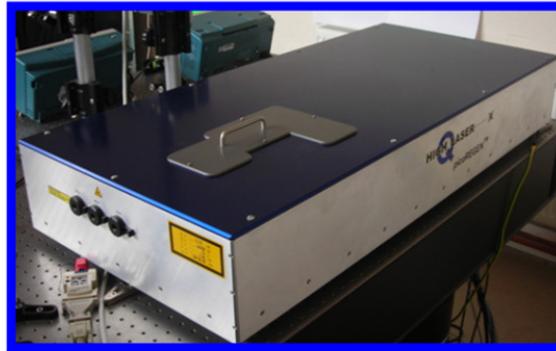
Femtosecond laser pulses always have a broad spectral bandwidth, because the pulse duration is inversely proportional to its spectrum (see equation 2.2.1), i.e. ultrashort pulse duration always causes a broad spectrum. The spectral bandwidth ( $\Delta\lambda$ ) of the pulses generated by the CPA2010 has been measured by an autocorrelator,  $\Delta\lambda \approx 5$  nm,

which can cause obvious chromatic distortion of the shape of the generated multiple beams with a large diffractive angle (Chapter 4).

### 3.2.1.2 High-Q picoseconds laser system

Another ultrashort pulse laser system used for the present research is a custom made seeded Nd:VAN regenerative amplifier laser system (High-Q IC-355-800ps, Photonics Solutions [34]) capable of running at up to 50 kHz repetition rate with output wavelengths at 1064 nm, 532 nm and 355 nm. Maximum pulse energy,  $E_p > 0.25$  mJ, was measured at 1064 nm, with pulse duration,  $\tau_p \approx 10$  ps. The high-Q IC-355-800ps system is principally comprised of a laser head, a laser controller (including power supply) and a chiller, shown in figure 3.2.4.

As introduced in 2.2.1.3, with a more compact and simpler system design, where the complicated chirped-pulse amplification (CPA) is not required, picosecond laser systems are more stable and reliable. The layout of High-Q IC-355-800ps system is similar to the one shown in figure 2.2.4 (chapter 2, page 13), where without any manipulation of pulse duration, a pulse picker followed the regenerative amplifier output hence allowing a single pulse to be selected by applying an appropriate TTL signal to the controller. Moreover, the system is remotely controlled by user-friendly computer software. Figure 3.2.5 shows the interface of the control software, through which most of the common laser operations can be easily done by mouse clicks and drags, e.g. switching the pulse repetition rate (by controlling the TTL signal), varying the output (by tuning the internal attenuator) and so on.



**Laser head**



**Laser controller  
(including power supply)**



**Chiller**

*Fig. 3.2.4: High-Q IC-355-800ps picosecond laser system.*

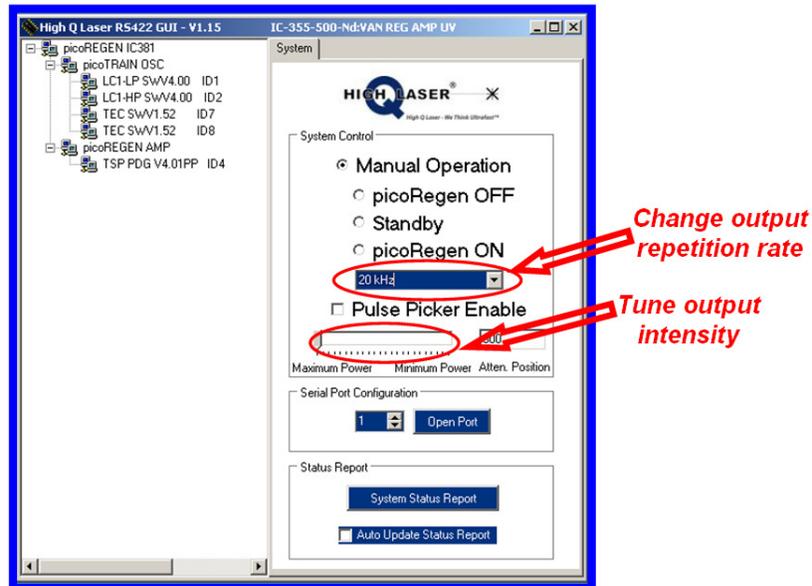


*Fig. 3.2.5: The interface of High-Q IC-355-800ps control software*

Due to the longer pulse duration, the monochromaticity of the High-Q IC-355-800ps system is good. Spectral bandwidth,  $\Delta\lambda \approx 0.1\text{nm}$ , has been measured at output wavelength,  $\lambda_0 = 1064\text{nm}$ , which makes the chromatic aberration negligible; hence this is taken advantage of in the present research for diffractive multiple beam microprocessing (Chapter 6).

### 3.2.2 Spatial Light Modulators (SLM)

#### 3.2.2.1 Holoeye - Boardband coated SLM

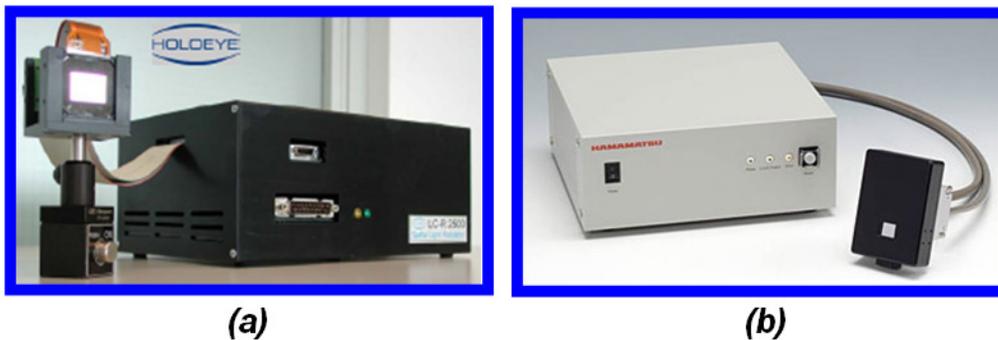


**Fig. 3.2.6:** Commercial SLMs used for current research: (a) Holoeye LC-R 2500, (b) Hamamatsu X10468-03 (X10468-04 has the same appearance as X10468-03).[92, 93]

As shown in figure 3.2.6 (a), the Holoeye [92] LC-R 2500, one of the SLMs used for present research, is an electrically addressed reflective SLM (ER-SLM), based on a pixelated liquid crystal on silicon (LCoS) microdisplay supporting digital visual interface (DVI) signals with extended graphics array (XGA) resolution ( $1024 \times 768$  pixels). With broad band metallic coating for visible light (central wavelength,  $\lambda_0 = 532\text{nm}$ ), the reflectivity and maximum phase modulation of the LC-R 2500 have been measured as approximately 75% and  $2\pi$ , respectively, when inputting the laser pulses from the Clark-MXR CPA2010 with 180fs pulse duration and 775nm wavelength at near infrared region. As will be introduced in detail in 4.3, the response time of the

LC-R 2500, the time for building up and fading out a CGH, has been measured approximately 10 and 18 ms respectively, which allows the real time CGH displaying rate for parallel processing to reach 50Hz.

### 3.2.2.2 Dielectric coated SLM – Hamamatsu

The Hamamatsu [93] X10468-03 and the X10468-04, another two ER-SLMs employed for present research and shown in figure 3.2.6 (b), are also based on a pixelated liquid crystal device with SVGA resolution ( $800 \times 600$  pixels). However, in this case, they have a dielectric coated mirror, providing  $> 90\%$  measured reflectivity for input laser beams with a specified wavelength (1064 and 532nm), for the High-Q picosecond laser system.

Another difference compared to the LC-R 2500 is the characteristics of the liquid crystal (LC). The LC-R 2500 has a 45 degree twisted nematic LC layer whose molecules are arranged in a twisted array from the front to the back of the device. Therefore, the device can not only modulate the phase of the light, but also rotate the plane of polarization. In contrast, the X10468-03/04 is a parallel aligning nematic crystal device, in which the LC molecules are aligned horizontally along the optical axis, hence causing a phase change to the light polarised along the molecule axis, but leaving the light polarisation perpendicular to the molecular axis completely unaffected.

The specifications of both the LC-R 2500 and the X10468-03/04 SLM devices are listed in table 3.1.

**Table 3.1: Specifications of SLMs employed for present research.**

Model	Hamamatsu X10468-03/04	Holoeye LC-R2500
<b>LC Type</b>	Parallel-aligned nematic	45degree twisted nematic
<b>Mode</b>	Phase only	Phase & amplitude
<b>Resolution (pixels)</b>	SVGA (800 × 600)	XGA (1064 × 768)
<b>Pixel pitch (μm)</b>	20	19
<b>Effective area (mm<sup>2</sup>)</b>	16 × 12	19.5 × 14.6
<b>Mirror coating</b>	Dielectric	Board band metallic
<b>Readout wavelength (nm)</b>	510 ± 50 (X10468-04) 1050 ± 50 (X10468-03)	400 - 1064
<b>Reflectivity *</b>	>90%	≈ 75%
<b>Fill factor</b>	95%	93%
<b>Response time** (rise/fall ms)</b>	15/30	10/18
<b>Frame rate (Hz)</b>	60	72

\* The actual reflectivity depends on readout light wavelength.

\*\* Time required to change from 10% to 90% for  $2\pi$  modulation

### 3.2.2.3 High power tests on Spatial Light Modulators (SLM)

#### 3.2.2.3.1 The possible damages on SLM

To ensure that the diffractive multiple beams have sufficient pulse energy for microprocessing,  $E_p > E_{th}$  ( $E_{th}$  is the threshold energy of target material), especially for High-Q IC-355-800ps system running at high repetition rate (up to 50kHz), high input power may be required for parallel processing, which might cause possible damage on the SLM. Therefore, to avoid such damage, a high power test on the SLMs, to determine the safe input power range, is necessary.

The most common forms of damage on SLMs are abrasion of the coating, and photochemical and thermal damage of the liquid crystal (LC) cells [123]. Abrasion damage will occur when the peak power density of input light is too high and exceeds the abrasion threshold, while photochemical damage is caused by absorption of ultraviolet (UV) light by the LC, whose absorption coefficient increases at wavelengths ( $\lambda$ )

less than 350nm, hence making the LC molecules break down. Thermal damage is probably the most common form of damage and may take place due to the following steps:

- (1) A part of the input light energy is absorbed by the material inside the SLM,
- (2) LC heats up as a result of the absorbed energy,
- (3) LC birefringence decreases because of the increased temperature,
- (4) LC birefringence disappears when the temperature of LC reaches the isotropic phase temperature,
- (5) In the extreme case, LC may boil and undergo irreversible change.

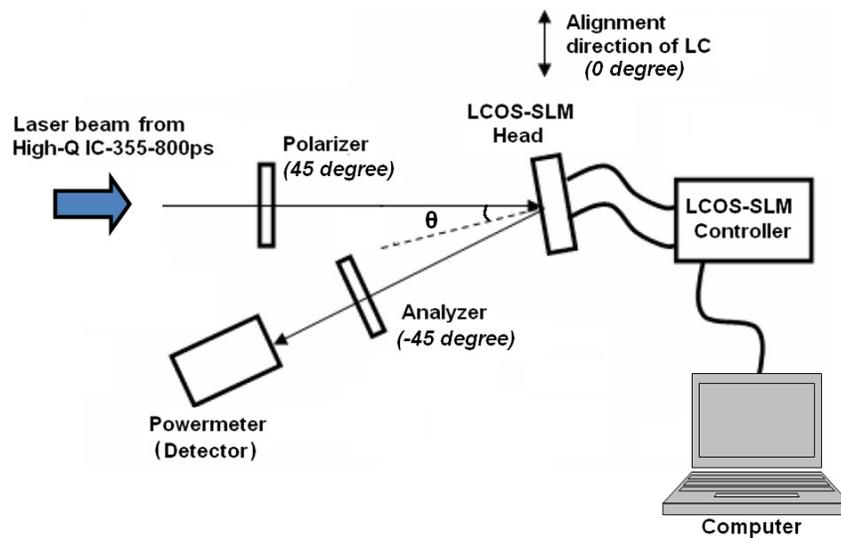


*Fig. 3.2.7: Experiment setup for high power laser beam test on the SLMs*

### 3.2.2.3.2 Experimental high power tests

The phase (birefringence) change in SLMs due to temperature rise was detected with a simple experimental setup, as shown in figure 3.2.7, in which the laser spot ( $\lambda = 1064\text{nm}$ ,  $\tau_p \approx 10\text{ps}$ ) with approximately 8mm diameter from the High-Q IC-355-800ps

was used as a high power source. By monitoring the phase change, a safe laser power range can be found.

As demonstrated in figure 3.2.7, a laser beam was linearly polarized by a polarizer and incident obliquely on an SLM with  $\theta < 10$  degree. Reflected on the SLM (which was located with the LC alignment direction parallel to the plane of the paper), the beam passed through an analyzer and then was detected by a power meter. The polarizer and analyzer were aligned as their polarization directions made an angle of 45 degrees with respect to the LC alignment direction. With this setup, the phase change created in the SLM was converted to intensity change, hence detected by the power meter. Figure 3.2.8 demonstrates the intensity detected when uniform images of various grey level were displayed on the Hamamatsu X10468-03 SLM. The relative intensity ( $I_r$ ) is the ratio of the measured intensity at each grey level ( $I_n$ ) over the maximum intensity ( $I_{\max}$ ).

$$I_r = \frac{I_n}{I_{\max}} \quad (3.2.1)$$

Since the phase modulation was almost linear with the grey level, the intensity modulation detected formed a sinusoidal curve. To make the detection sensitive, the grey level was fixed at a value where the intensity change was large. As shown in figure 3.2.8, 125 was the grey level where the intensity change was most sensitive.

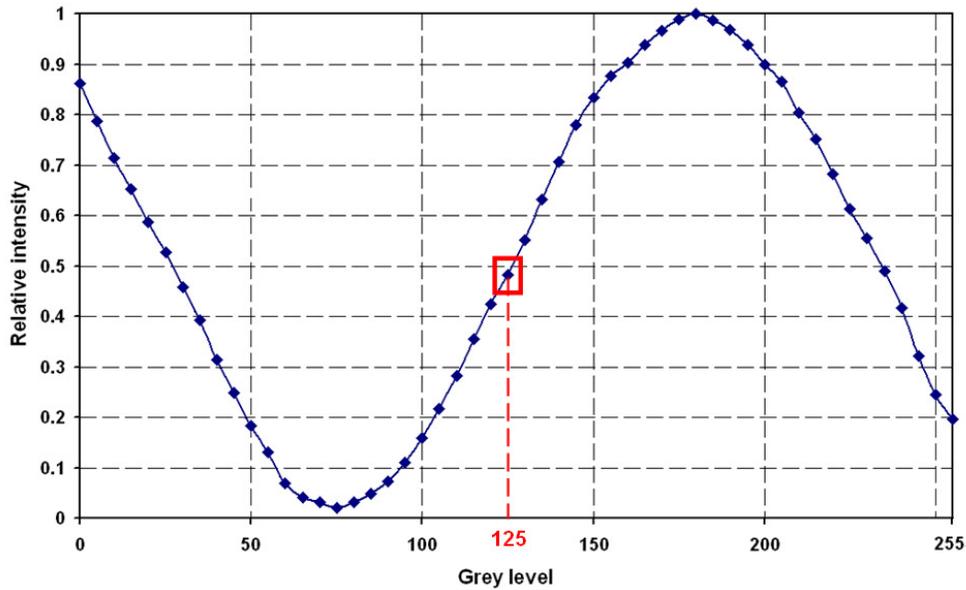


*Fig. 3.2.8: Variation in intensity with grey level, detected when uniform images are displayed onto the X10468-03 Hamamatsu SLM.*

### 3.2.2.3.3 Results and discussions of high power tests

Figure 3.2.9 demonstrates the change of detected relative intensity,  $I_n / I_{max}$ , (i.e. change of the phase modulation) versus the time after the illumination, when the laser beam ( $\lambda = 1064\text{nm}$ ,  $\tau_p \approx 10\text{ps}$ ) from the High-Q IC-355-800ps laser system running at 20kHz repetition rate, was input on the Holoeye LC-R 2500 and the Hamamatsu X10468-03 SLM individually with different power level.

As shown, the detected intensity dropped initially and became stable after illumination of approximately five minutes. This was due to the factor that the phase modulation changed by absorbing the thermal energy from the input laser beam and became stable after reaching the thermal equilibrium between the liquid crystal cells and other parts of the SLM. Since the LC-R 2500 absorbed more thermal energy because of the lower reflectivity, the intensity drop detected was greater and the SLM

could not work safely with high power input,  $> 2\text{W}$ . Due to the high reflectivity, the X10468-03 still worked quiet well with 2.6W power, the maximum output of the Q IC-355-800ps laser system, when only a  $< 5\%$  intensity drop was detected. With the same dielectric coating, X10468-04 also performed perfectly well with the high power input at  $\lambda = 532\text{nm}$  from the High-Q IC-355-800ps.

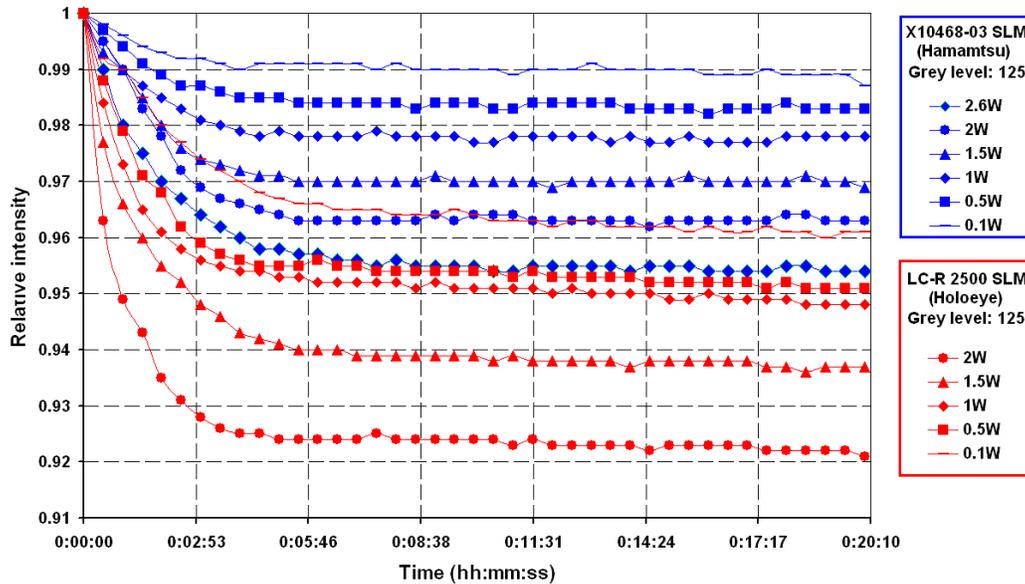


**Fig. 3.2.9:** The change of detected relative intensity,  $I_n / I_{max}$ , versus the time after the illumination. The blue data is from X10468-03 SLM with high reflectivity dielectric coating, while the red data is from LC-R 2500 absorbing more thermal energy due to its lower reflectivity.

#### 3.2.2.3.4 Analysis of high power laser beam tests

Since the dielectric coating provided high reflectivity, the X10468-03/04 worked safely with little intensity drop, even input with full power, 2.6W, from the High-Q IC-355-800ps. Accordingly, the X10468-03/04 was employed for ultrashort pulse laser parallel processing with high repetition rate, i.e. 20 kHz, and together with the generation of 25 diffracted beams, the processing demonstrated an ‘effective’ repetition rate of 500 kHz without restrictive scan speeds (Chapter 5).

For the LC-R 2500, due to the high energy absorption, > 5% intensity change was detected within five minutes illumination when > 1W power was applied, indicating that the LC might be damaged with high power applied and long illumination time. Therefore, the LC-R 2500 might not be able to handle the high power required for diffractive multiple beams parallel ultrashort pulse processing with high repetition. However, the LC-R 2500 worked perfectly well with the Clark-MXR CPA2010 running at 1kHz, where the ultrashort pulse laser ( $\lambda \approx 775\text{nm}$ ,  $\tau_p \approx 180\text{fs}$ ) with several hundreds of  $\mu\text{J}$  pulse energy (i.e. several hundreds of milliwatt in power) was diffracted into 30 highly uniformed diffracted beams for surface micro-structuring (Chapter 4).

### 3.2.3 Scanning galvanometer systems and multi-axis motion control systems

#### 3.2.3.1 Scanning galvanometer systems

Two scanning galvanometer systems, a GSI - High Performance Laser Scanning Module (GSI-HPM10VM2) and a Nutfield – XLR8 [125, 126], were employed to scan and focus the laser beam generated from the Clark-MXR CPA2010 and the High-Q IC-355-800ps, respectively. Figure 3.2.10 shows the workings of the galvanometer driven laser beam scanning system, which consists of two galvanometer driven mirrors (X and Y), a flat field f-theta lens with focal length  $f \approx 100\text{mm}$ , and integrated driver electronics enclosed in a black cube-like metallic case.

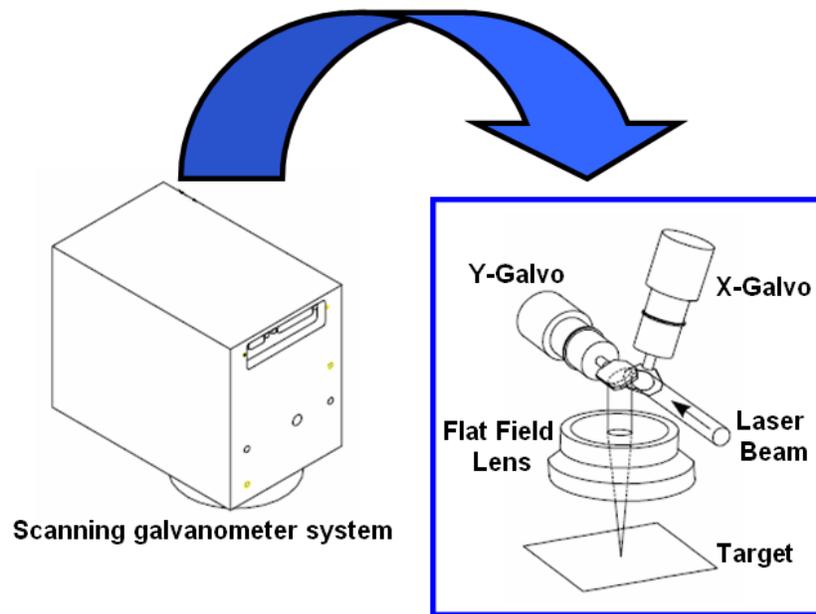


**Fig. 3.2.10:** The workings of the galvanometer driven laser beam scanning system, which consists of two galvanometer driven mirrors (X and Y), a flat field  $f$ -theta lens with focal length  $f \approx 100\text{mm}$ , and integrated driver electronics enclosed in a black cube-like metallic case.

The two-mirror, two-axis scanners provided the capability of deflecting optical beams in an XY manner for all possible laser applications. The synchronized action of the two galvanometer servo-controlled turning mirrors directed the laser beam to specific locations on a target material surface in both X and Y directions through the flat field  $f$ -theta lens producing an agile focusing system. The motion of the galvanometer, with nanometer level accuracy and up to  $10^4\text{mm/s}$  scanning speed, was controlled by two optional control software, SCAPS-SAMlight [127] and Lanmark-Winlase Pro.[128], both having a user friendly interface. As shown in figure 3.2.11, the software can create various geometrical shapes and texts as scanning orders with user defined parameters such as scanning speed.

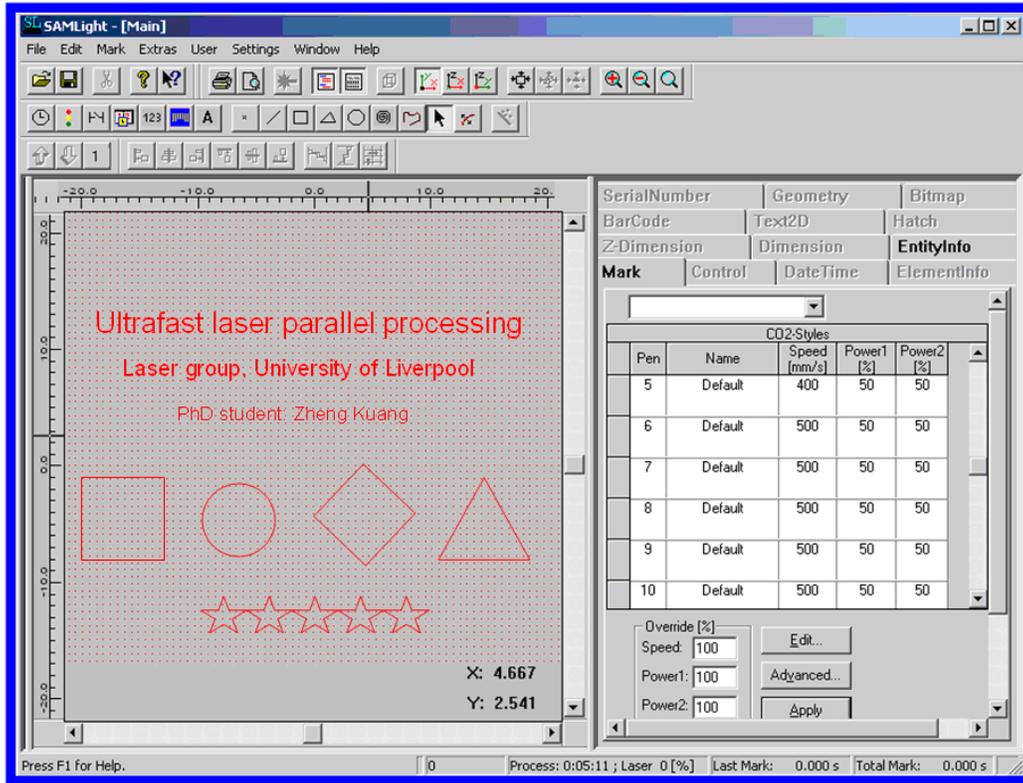


*Fig. 3.2.11: The interface of the software used to control the scanning galvanometer system.*

### 3.2.3.2 Multi-axis motion control system (Aerotech)

Two multi-axis Aerotech [129] motion control systems, as shown in figure 3.2.12 (a) and (b), were employed to precisely manipulate the sample with sub-micrometer and microradian accuracy for the Clark-MXR CPA2010 and the High-Q IC-355-800ps laser systems, respectively. These comprise four axis (x, y, z, u), x-y-z three dimensional movement plus the rotation (u), and five axis (x, y, z, p, q), x-y-z three dimensional movement plus the angles tilted in the x (p) and y (q) directions, as shown in figure 3.2.12. Both of the systems were controlled by a computer program provided by Aerotech and the motion of the sample stage was able to be synchronized with the scanning of the laser beam controlled by the galvanometer systems.

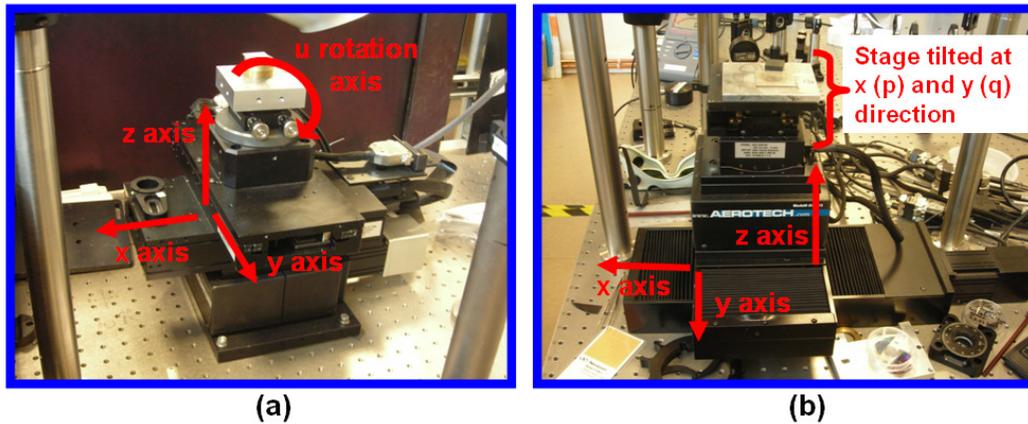


**Fig. 3.2.12:** Four axis (a) and five axis (b) Aerotech motion control systems used for current research.

### 3.3 Methods to remove the zero order beam

Since the diffraction efficiency  $\eta$  (defined as the percentage of the total energy output divided by the energy diffracted to the desired orders) cannot reach 100% with current commercial SLMs, there is always part of the output energy un-diffracted, which is called the zero order beam. To generate a diffracted pattern with over 10 desired multiple beams,  $\eta$  is measured at approximately 50%, meaning that the zero order beam, contains about half of the output energy and is always much stronger than any of the desired orders. Therefore, the zero order beam may lead to unwanted damage on the sample during processing, and hence should be removed.

As shown in figure 3.3.1, the brighter spot in the middle, corresponds to the zero order beam and is much stronger than any of the desired spots, the +1 orders at the bottom. The upper weaker spots were the -1 orders, which were the undesired higher orders and sometimes called ‘ghosts’. Since the hologram generating this multi-beam pattern was calculated to enhance the +1 orders, the intensity of the undesired orders, e.g. -1,

were normally below the material ablation threshold and should have no effect on the sample. (LLEC stands for Lairside Laser Engineering Centre, where the laboratory of the present research is located.)

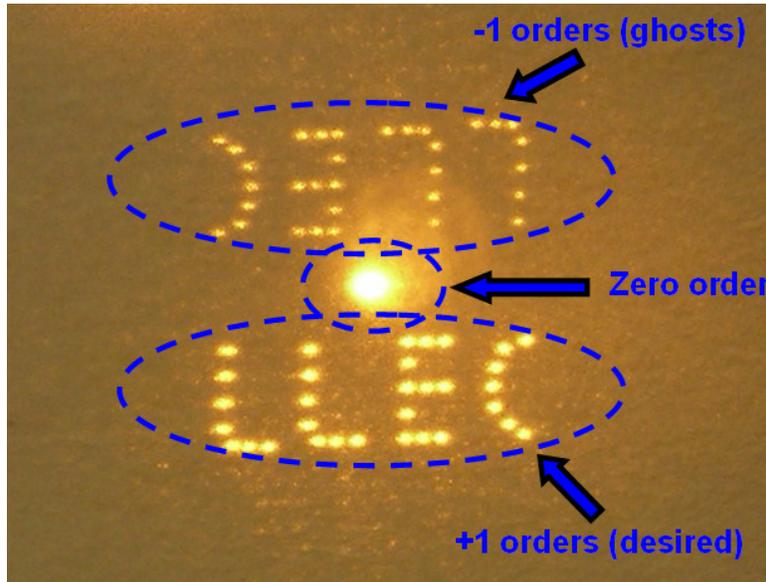


*Fig. 3.3.1: An 'LLEC' pattern with 32 desired diffracted beams projected on a paper screen.*

### 3.3.1 Removal of the zero order beam with a 4f-imaging optical system

#### 3.3.1.1 Zero order beam removed with 4f system

Physically blocking the zero order beam at the Fourier plane of a 4f optical system is the most common and direct method to avoid sample damage by the focussed zero order beam. This method is shown in figure 3.3.2, in which lens 1 and lens 2, both having a focal length of  $f$ , form a 4f optical system, i.e.  $AB = BP = PC = CD = f$ . The input beam, represented by a complex field,  $\psi_0 = A \exp(i\phi_0)$ , is modulated by the phase hologram,  $\psi_t = \exp(i\phi_h)$ , displayed on the SLM. Therefore, after reflection, the

modulated beam,  $\psi_h = \psi_0 \cdot \psi_t = A_m \exp[i(\varphi_0 + \varphi_h)]$ , is diffracted with an angle  $\theta$  to the desired position, while the zero order beam,  $\psi_0 = A_0 \exp(i\varphi_0)$ , is not diffracted, i.e.  $\theta = 0$ , and hence is separated from the desired orders at the Fourier plane P through lens 1. Since a small target is put at Q to only block the zero order beam, the optical field at A is reconstructed after the lens2 at D, but without the un-modulated zero order beam. As a scanning galvanometer with a flat field f-theta lens working as a focal system is used in the current research to make parallel processing more flexible, the modulated beam will go through the galvanometer aperture and will be again focussed on the sample to allow material machining.

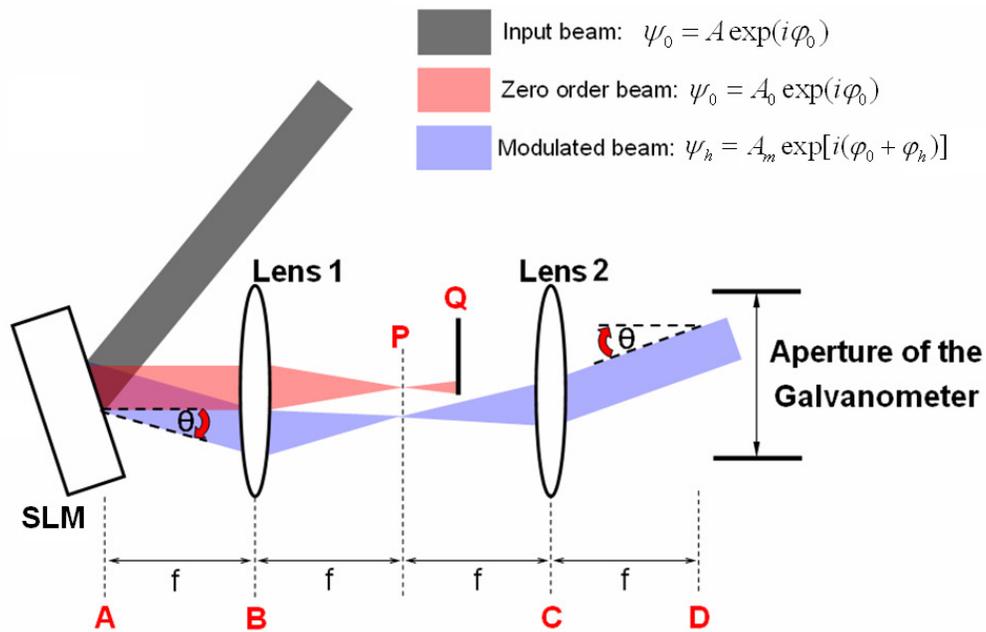


**Fig. 3.3.2:** Schematic diagram for blocking the zero order beam at the Fourier plane P of the 4f optical system.

### 3.3.1.2 Modelling the 4f-imaging optical system with ZEMAX

To properly build up a 4f optical system into the experiment setup, it was necessary to carefully choose the correct optics (e.g. lenses and mirrors) and reasonably align them to match the experimental environment. To meet this, the 4f optical system was modelled by a powerful optical design computer program, ZEMAX [124].

There was a stock lens catalog in ZEMAX, where various models of lenses from vendors, e.g. Newport, Coherent, CVI and so on, could be chosen for the modeling of 4f optical system. By consideration of both performance and price, two plano-convex lenses, detailed in the following table, were ordered from Newport.

*Table 3.2: The details of lens chosen for building up the 4-f optical system.*

Vender	Model	Material	Coating	EFL***	Diameter
Newport	KPX205 *	BK7	AR.16 **	300mm	50.8 mm

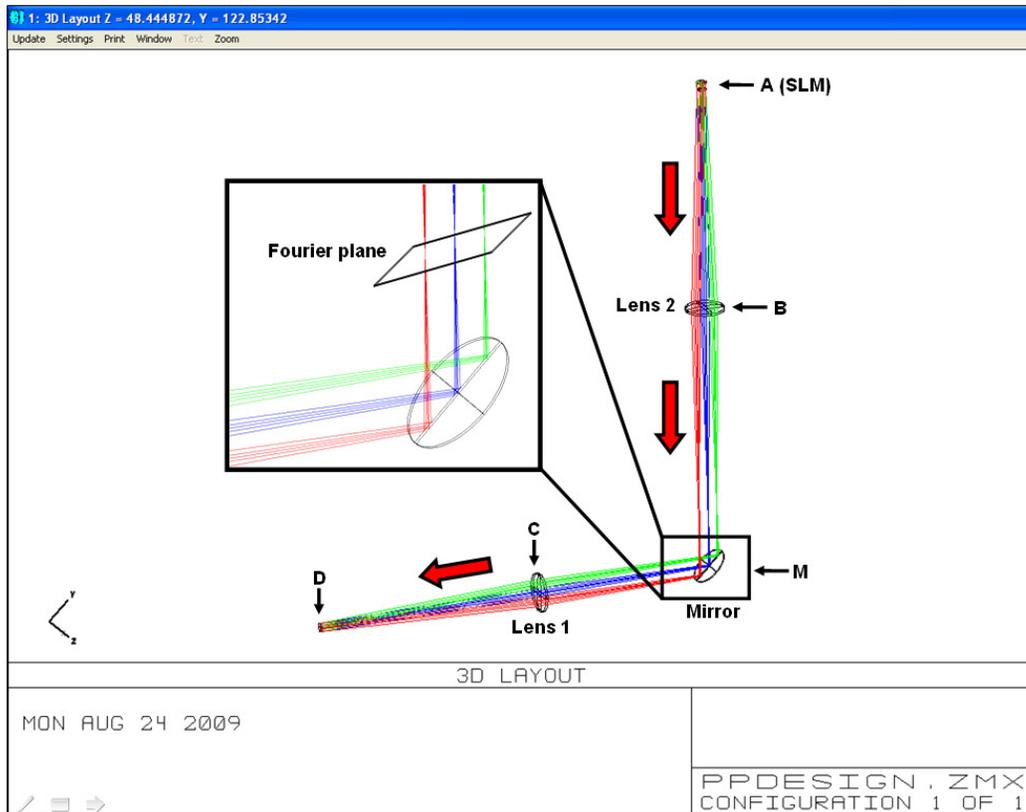
\* **KPX205 is a plano convex lens**

\*\* **Anti-reflection coating for 650-1064nm**

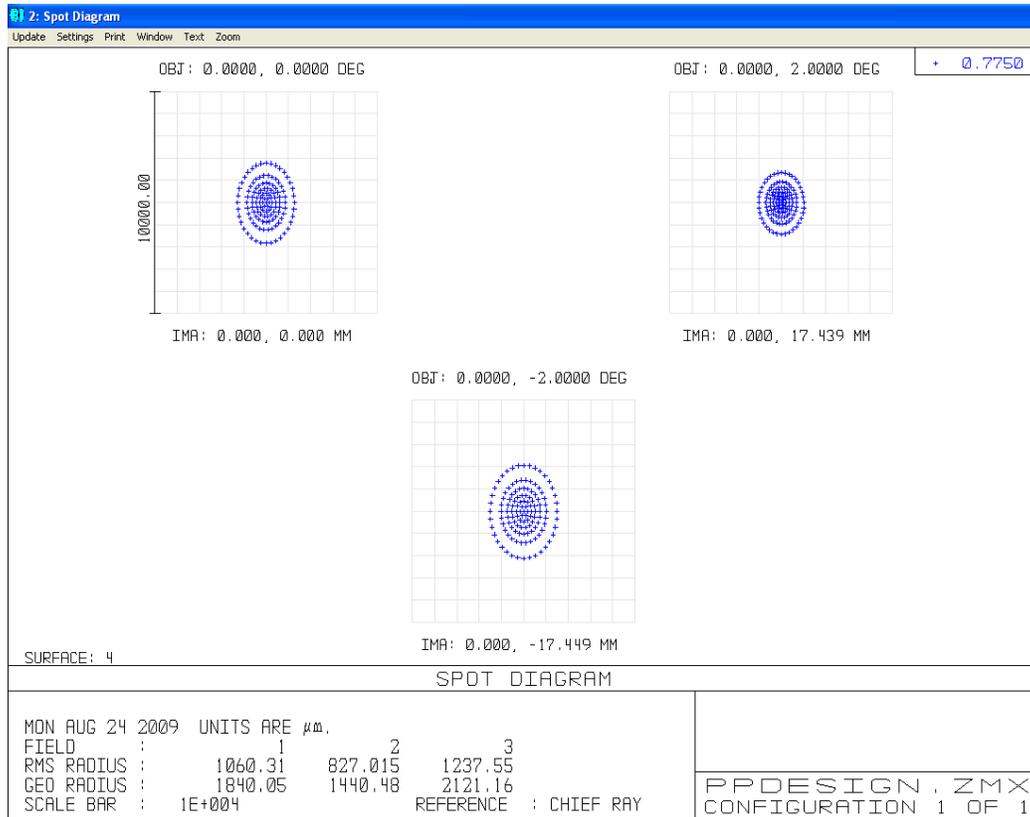
\*\*\* **Effective Focal Length**

Figure 3.3.3 shows the 3D layout of the modeled 4f optical system using ZEMAX, where lens 1 and 2 were the ordered plano-convex lenses, and a mirror, coated for 45 degree input, was used, directing the beam to the required path. The position A, where three collimated beams with different angle,  $\theta$ , start, corresponded to the reflection plane of the SLM. The blue beam, standing for the zero order beam, had  $\theta = 0$ , while the green and red beams respectively had  $\theta = \pm 2$  degree, greater than the maximum diffractive angle of the desired +1 order with 1064nm input. More details about the beam reflection on the mirror are given in the inserted 3D layout with large magnification, which clearly demonstrates that the zero order beam can be separated

from the others and physically blocked by a small opaque target somewhere near the Fourier plane. The mirror was set away from the Fourier plane, where the spot size was sufficiently large, hence ensuring that the beam intensity on the mirror was lower than the damage threshold, as shown in figure 3.3.4. Table 3.3 lists the optimized value of distance between each optical element to minimize the wavefront distortion, while figure 3.3.5 shows that the zero order beam was successfully blocked with a 4f optical system according to the ZEMAX modeling results.



**Fig. 3.3.3:** 3D layout of the modeled 4f optical system



**Fig. 3.3.4:** Spot diagram showing each spot size on the mirror – The radius of the spots,  $r$ , is given beneath; the energy intensity,  $I$ , hence was easily calculated by

$$I = \frac{E_p}{\pi r^2}, \text{ which was well below the damage threshold of the mirror coating.}$$

**Table 3.3:** Optimized value of distance between each optical element to minimize the wavefront distortion.

Distance AB	Distance BM	Distance MC	Distance CD
~303.20mm	~215.33mm	~382.07mm	~302.05mm

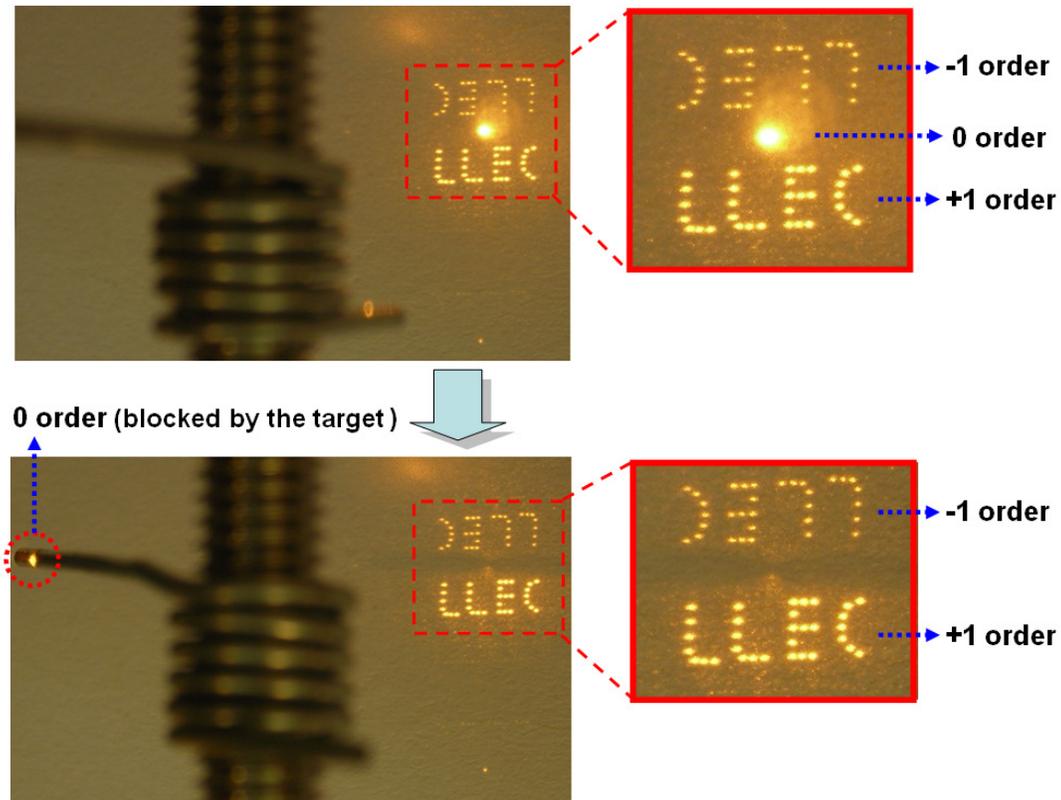


*Fig. 3.3.5: Demonstration of the enhancement of the +1 diffracted orders (LLEC pattern) combined with blocking the zero order beam using a small metallic target. The image shows intensity distribution on a paper screen taken with a digital camera.*

### 3.3.2 Removal of the zero order beam by adding a Fresnel zone lens

#### 3.3.2.1 Defocusing of the zero order beam at processing plane

Alternatively, in the current research, the zero order beam was also significantly defocused at the processing plane by adding a phase Fresnel lens (PFL) onto the computer generated hologram (CGH) [90]. The focal length ( $f_i$ ) of the PFL can be adjusted by the software developed by Holoeye [92], as shown in figure 3.3.6.

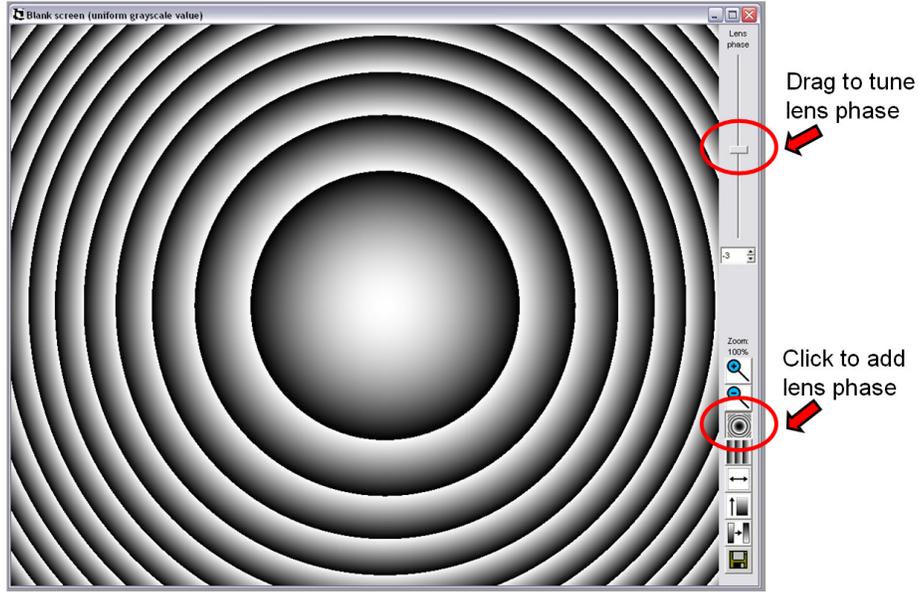


*Fig. 3.3.6: Interface of the software developed by Holoeye, which can easily superimpose and adjust the phase of the PFL.*

Only the diffracted beams were converged ( $f_i > 0$ ) or diverged ( $f_i < 0$ ) by the PFL while the zero order beam was unaffected hence separating the focal planes of the diffracted from the zero order beam, as shown in figure 3.3.7. The following beam matrix equation describes the propagation of the diffracted beam from the Liquid Crystal on Silicon (LCoS) surface (A) to its focal plane (B),

$$\begin{pmatrix} X_B \\ tg\theta_B \end{pmatrix} = \begin{pmatrix} 1 & d_2 \\ 0 & 1 \end{pmatrix} \times \begin{pmatrix} 1 & 0 \\ -\frac{1}{f_2} & 1 \end{pmatrix} \times \begin{pmatrix} 1 & d_1 \\ 0 & 1 \end{pmatrix} \times \begin{pmatrix} 1 & 0 \\ -\frac{1}{f_1} & 1 \end{pmatrix} \times \begin{pmatrix} X_A \\ tg\theta_A \end{pmatrix} \quad (3.3.1)$$

where  $X_A$  and  $X_B$  are the distances of the beam from the axis and  $tg\theta_A$  and  $tg\theta_B$  are the gradients of the beam with respect to the axis at the position A and B, respectively. Since  $tg\theta_B = 0$  and  $X_A = 0$ , the focal plane separation ( $\Delta d$ ) can be calculated by the following equation derived from the beam matrix equation:

$$\Delta d = |d_2 - f_2| = \left| \frac{f_1 f_2 - f_2 d_1}{f_1 + f_2 - d_1} - f_2 \right| \quad (3.3.2)$$

where  $d_1 \approx 200\text{mm}$  was the distance between the LCoS and the  $f$ -theta lens, and  $f_2 \approx 100\text{mm}$  was the focal length of the  $f$ -theta lens. Thus:

$$\Delta d(\text{mm}) = \left| \frac{100f_1 - 20000}{80 + f_1} - 100 \right| \quad (3.3.3)$$

A slightly defocused zero order beam could still damage the sample because it contains approximately 50% of the input pulse energy which was much stronger than any of the diffracted orders. Accordingly,  $f_1$  must be adjusted carefully to allow sufficient separation ( $\Delta d$ ) so that the fluence at the substrate is below the damage threshold. Figure 3.3.8 (a) demonstrates a CGH calculated by the Gratings and Lenses (GL) algorithm [102, 103] to generate eight first order identical beams and its computational reconstruction, while figure 3.3.8 (b) shows the micro-machined results on Ti6Al4V using the CGHs which were superimposed by PFLs with different  $f_1$  to adjust  $\Delta d$ . Figure 3.3.8 (b) shows that the defocused zero order beam still damaged the sample when the separation was  $\Delta d = 1\text{mm}$  (middle lower picture), while it was totally removed when  $\Delta d = 5\text{mm}$  (right lower picture).

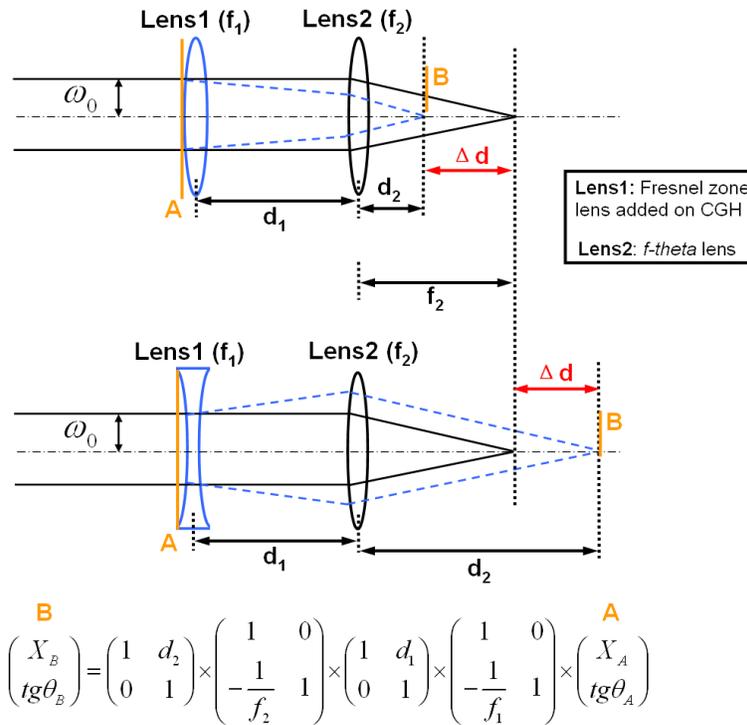


**Fig. 3.3.7:** Schematic showing the method to separate the focal plane of diffracted beams from the zero order beam. The added PFL, lens 1, can work as either positive lens (upper) or negative lens (lower) to obtain the separation,  $\Delta d$ . The beam matrix equation describes the propagation of diffracted beam from LCoS surface (A) to its focal plane (B).

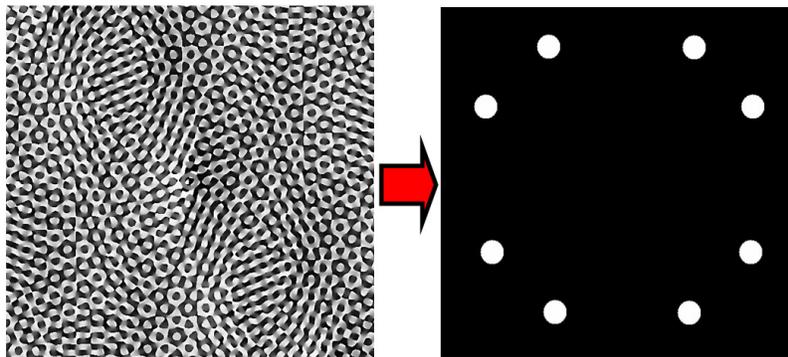


**Fig. 3.3.8 (a):** A CGH calculated by the GL algorithm to generate eight first order identical beams (left) and its computational reconstruction (right).

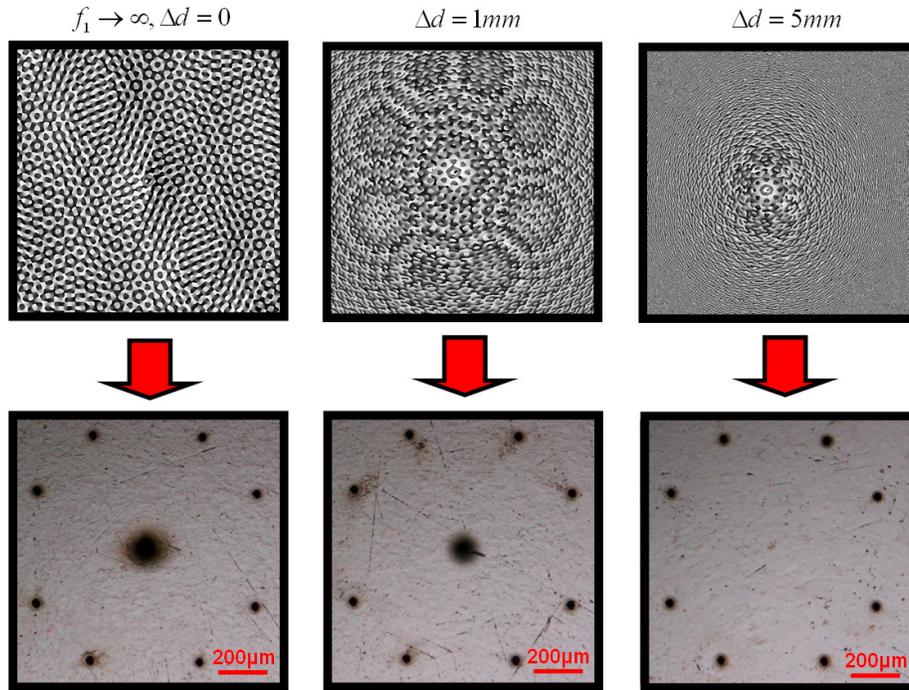


*Fig. 3.3.8 (b): The CGHs superimposed by PFLs with different  $f_1$  to adjust  $\Delta d$  (upper) and the machined results on Ti6Al4V (lower).*

### 3.3.2.2 Combination of the Fourier and Fresnel plane hologram

By superimposing a PFL, the desired diffractive multiple beams were focused on neither the Fourier nor the Fresnel plane. Referring to section 2.2, the CGH hence became the third type, the combination of the Fourier and Fresnel plane hologram. The current author is the first to avoid the unwanted zero order effect using above method [90].

## 3.4 Experimental setups

In the present research, there were two different experimental setups in terms of the method used to eliminate the zero order beam.

### 3.4.1 Experimental setup without the 4f optical system

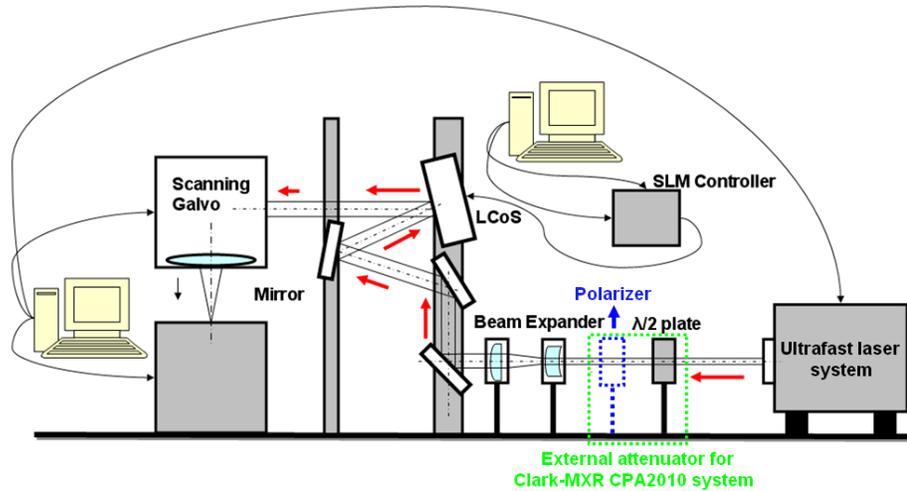


*Fig. 3.4.1: Experiment setup without the 4f optical system.*

Figure 3.4.1 shows the schematic of the experimental setup without the 4f optical system, by which the zero order beam was eliminated by adding a phase Fresnel lens. As shown, the ultrashort pulse laser beam, from the Clark-MXR CPA2010 ( $\tau_p \approx 180\text{fs}$ ) or the High-Q IC-355-800ps ( $\tau_p \approx 10\text{ps}$ ), traversed a half wave plate used for adjusting the linear polarization direction, a beam expander,  $M \approx 2$ , and after reflection on mirrors 1 and 2, illuminated a proper coated commercial SLM liquid crystal on silicon (LCoS) device, oriented at  $<10$  degree angle of incidence. Directed by the LCoS, the modulated beam entered a scanning galvanometer with  $f = 100\text{mm}$  flat field of an  $f$ -theta lens. Substrates were mounted on a precision 4 ( $x, y, z, u$ ) or 5 ( $x, y, z, p, q$ ) axis motion control system (Aerotech) allowing accurate positioning of the substrate surface at the laser focus. For the Clark-MXR CPA2010 without internal intensity adjustor, an external attenuator, formed by setting a Glan laser polarizer after the half wave plate, was used in the experiments.

### 3.4.2 Experimental setup with 4f optical system

Although eliminating the zero order beam by adding a phase Fresnel lens (PFL) simplified the experiment setup, it also brought difficulties on finding the processing plane, where the desired diffractive multiple beams are focused. Furthermore, since the CGHs with added PFLs of different focal length,  $f$ , have a different processing plane, synchronization of stage movement (up and down) and the applied CGH is needed for the process requiring real time playing of these CGHs. Even if the complicated synchronization could be correctly performed, the time consuming stage movement would significantly decrease the processing speed. Therefore, a 4f optical system was also used for the research to physically separate and block the zero order beam, while the processing plane, i.e. the focal plane of the  $f$ -theta lens, was not changed for all the applied Fourier Plane CGHs.

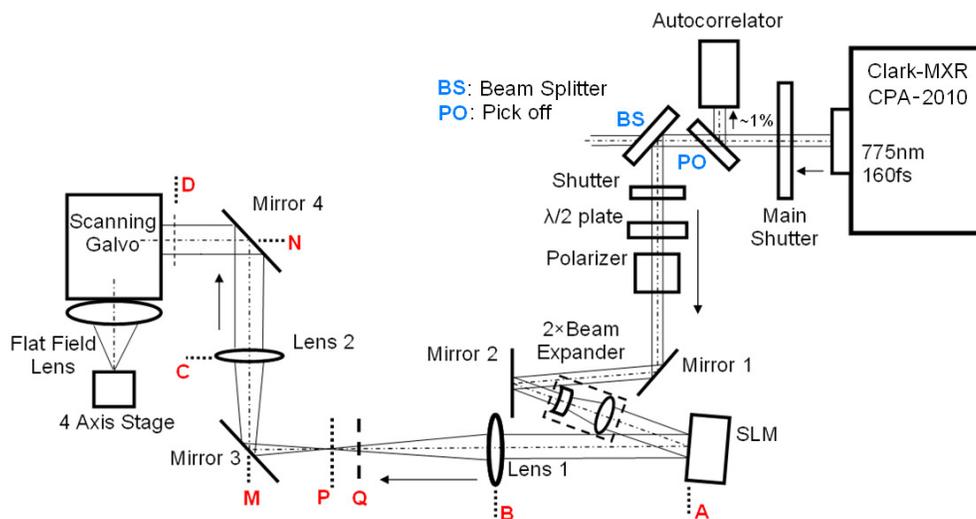


**Fig. 3.4.2:** The schematic of experiment setup for Clark-MXR CPA2010 with a 4f optical system.

Figure 3.4.2 shows a schematic of the experimental setup with a 4f optical system, where the Clark-MXR CPA2010 was employed, generating ultrashort laser pulses,  $\tau_p \approx 180\text{fs}$  and  $\lambda_0 = 775\text{nm}$ . The output of ultrashort pulses with 1 kHz repetition rate was attenuated by a half wave-plate and a Glan laser polariser. After reflection on mirrors 1 and 2, the laser illuminated a reflective SLM liquid crystal on silicon (LCoS) device with  $1024 \times 768$  pixels (Holoeye LC-2500), oriented at  $< 10^\circ$  angle of incidence. A beam expanding telescope, with magnification,  $M \approx 2$ , was used to reduce the average intensity on the SLM, where the computer generated holograms (CGHs) were displayed. Appropriate holograms required to create arbitrary multi-beam patterns at the substrate surface were generated via an interactive LabVIEW program using a number of algorithms to calculate the CGHs (detailed in 2.3.2.3). The input optical beam was represented by a complex field,  $\psi_0 = A \exp(i\phi_0)$ , and the SLM displayed a phase hologram,  $\psi_t = \exp(i\phi_h)$ . Accordingly, after reflecting on the SLM (at A in fig. 3.4.2), the beam was modulated to be  $\psi_h = \psi_0 \cdot \psi_t = A_m \exp[i(\phi_0 + \phi_h)]$ . Lens 1 and 2 were two AR coated BK7 plano-convex lenses as detailed in table 3.2. Referring to Fig. 3.4.2, since distance  $AB = BP = PM + MC = CN + ND \approx f$  ( $\approx 300$  mm), following the modelling results given in table 3.3, a 4f optical system with unity magnification was formed. Accordingly, at D, the complex field was identical with that at A. The zero order reflected beam was spatially separated and blocked at Q. Just after D, the modulated beam,  $u_h$ , entered the 10 mm aperture of a scanning galvanometer system with a flat field lens ( $f = 100$  mm). The proximity of the beam,  $u_h$ , (at D) to the input aperture of the galvanometer ensured that diffracted beams were transmitted cleanly to the substrate surface, while the flat field of the f-theta lens produced a near perfect focusing system. Substrates were mounted on a precision

4-axis (x, y, z, u) motion control system (Aerotech) allowing accurate positioning of the substrate surface at the laser focus.

For the High-Q IC-355-800ps, the experimental setup was very similar to that shown in figure 3.4.2. A dielectric coated SLM (Hamamatsu X10468-03 or X10468-04) with high reflectivity, > 90%, was used for 1064nm and 532nm output respectively, where high average power (up to ~ 2.6W) was applied with high repetition rate, 20kHz, demonstrating encouragingly fast parallel processing (Chapter 6).

### **3.5 Summary**

This chapter has introduced the main equipments used for the current research, including the ultrashort pulse laser systems, SLMs, scanning galvanometer and motion control systems. Then, the two different methods used to eliminate the unwanted zero order beam have been presented. The first method physically blocks the zero order beam at the Fourier plane of a 4f optical system, while the second method, devised by the current author and published in a peer reviewed journal [90], defocuses the zero order beam at the processing plane using a combination of the Fourier and Fresnel plane holograms. The final part of the chapter introduced the experimental setups.

## **Chapter 4**

# **Diffractive multi-beam microprocessing using femtosecond laser pulses**

## 4.1 Introduction

After giving the detailed experimental procedure in chapter 3, this chapter presents the results of diffractive multi-beam microprocessing using femtosecond laser pulses,  $\tau_p \approx 160\text{fs}$ ,  $\lambda = 775\text{nm}$ , and  $f = 1\text{kHz}$ , generated by the Clark-MXR CPA2010 laser system.

The results from micro-machining using static diffractive pattern created by the simple and computationally fast Lenses and Gratings algorithm will be firstly demonstrated in 4.2.1, where  $\sim 0.3\text{mJ}$  pulse energies were successfully split into more than 30 desired diffractive multiple beams with good uniformity, each of them having  $\mu\text{J}$  pulse energy, the observed energy level for precision processing. The observed linearly increased eccentricity of hole shape when gaining the diffractive angle, which was caused by finite spectral bandwidth of femtosecond laser pulses, will be discussed after in 4.2.2.

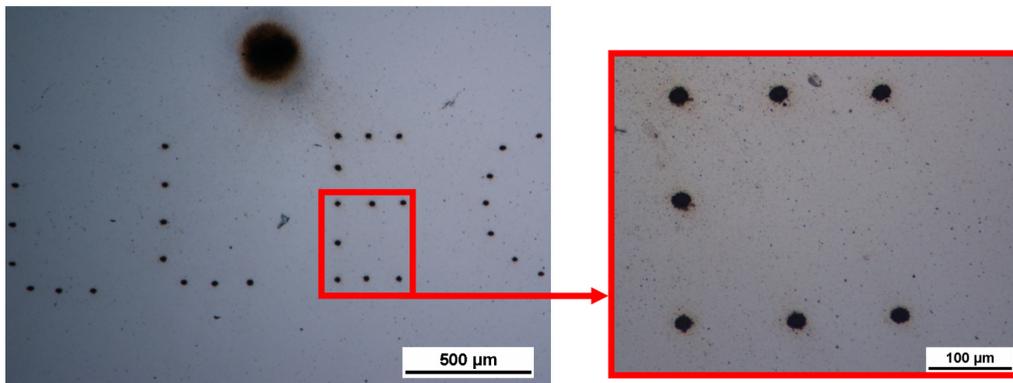
Starting with the discussion of the SLM response time, section 4.3 will demonstrate dynamic diffractive pattern micro-processing by real time playing of the CGH plus synchronization of the scanning method, which added an additional flexibility for surface micro-structuring.

## 4.2 Static CGH multiple laser beam micro-processing

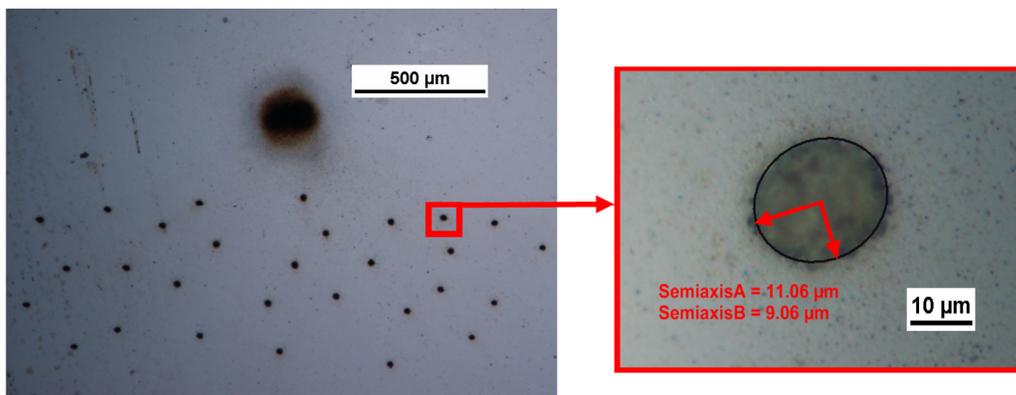
### 4.2.1 Precision micro-drilling using diffractive $\mu\text{J}$ -level multiple beams

Figure 4.2.1 (a) shows optical micrographs of the surface structuring on silicon with an ‘LLEC’ pattern comprising 32 blind holes while Figure 4.2.1 (b) demonstrates a random spot pattern comprising 30 holes. Each hole pattern was micro-machined simultaneously on a silicon wafer by creating the spot patterns in the LabVIEW

program [102] then applying the calculated CGHs to create the desired geometries. The Gratings and Lenses (GL) algorithm [102, 103], which is simple and computationally fast, was used to calculate computer generated holograms (CGHs) producing multiple independent diffractive +1 order beams for processing. The incident pulse energy on the SLM was  $E_p \sim 300\mu\text{J}$ . All diffractive spots had similar dimensions indicating accurate calculation of the CGH. The large hole above the main pattern of holes was generated by the zero order beam.



*Fig. 4.2.1 (a): 'LLEC' pattern comprising 32 micro-sized holes.*



*Fig. 4.2.1 (b): Random spots pattern comprising 30 micro-sized holes.*

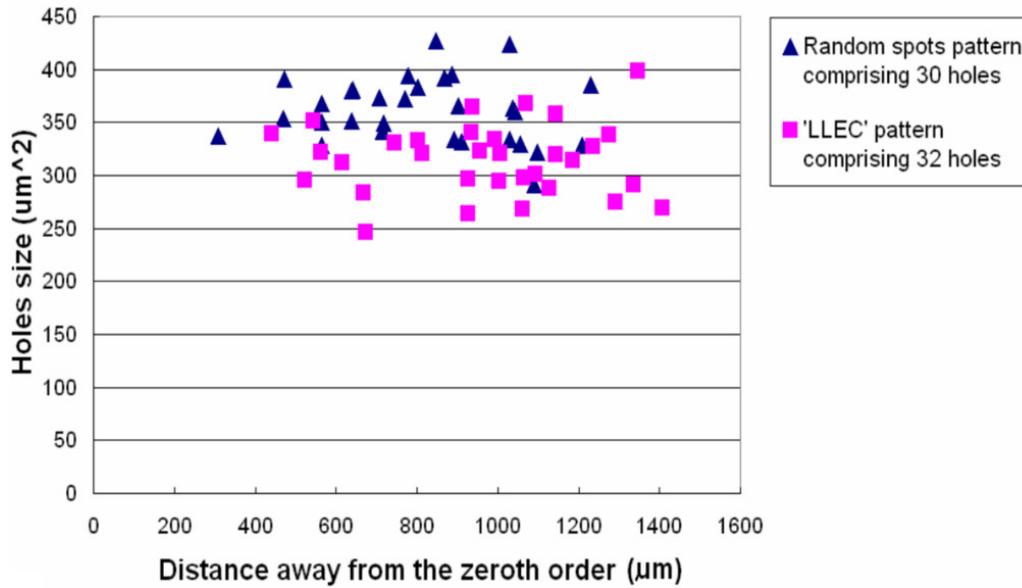
In order to evaluate the pulse energy of each of the diffracted spots, the size of hole produced was compared to a calibrated series of drilled holes using a single beam of varying pulse energy, as shown in table 4.1. When using the SLM, the diameter of each of the 30 diffractive spots was measured to be  $\sim 20\mu\text{m}$ , which indicated that each of the spots had a pulse energy of approximately  $5\mu\text{J}$ . The total input pulse energy was evaluated by measuring the power ( $\sim 300\mu\text{J}$ ) before the aperture of the scanning galvanometer. Consequently, the diffraction efficiency of the SLM is approximately 50%, which is fairly typical of commercially available units, especially when used slightly outside their recommended range of operating wavelengths (in this case, the employed SLM, the Holoeye LC-2500, is broad band coated and recommended for use in the visible region, 400-700nm).

**Table 4.1:** The calibrated series of drilled hole diameters using a single beam of varying pulse energy.

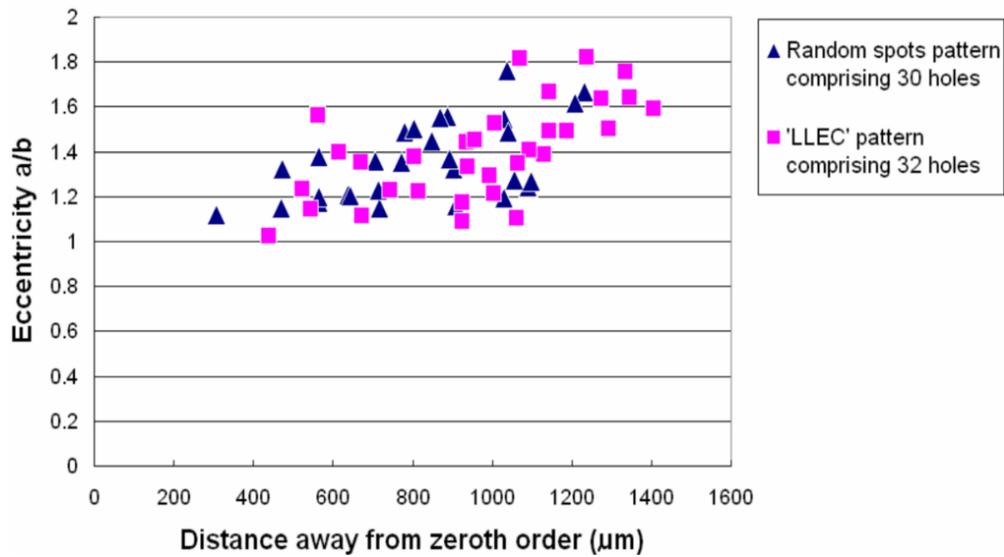
Pulse energy, $E_p$ ( $\mu\text{J}$ )	Spot diameter ( $\mu\text{m}$ )
1-3*	$<15^{**}$
4*	$\sim 15$
5	$20.3 \pm 0.4$
10	$25.1 \pm 0.5$
15	$30.2 \pm 0.6$
20	$35.5 \pm 0.8$
25	$41.3 \pm 0.8$
30	$46.2 \pm 1.1$
35	$52.4 \pm 1.3$
40	$58.6 \pm 1.4$

\* Around the ablation threshold

\*\* Unstable ablation crater size



(a) Hole size (area) vs. distance away from zeroth order hole



(b) Eccentricity  $a/b$  vs. distance away from zeroth order hole

**Fig. 4.2.2:** Hole size and eccentricity versus the distance from each diffracted spot to the zero order hole in both 'LLEC' and random spots patterns

Figures showing measured hole size and eccentricity versus distance from the zero order hole in both 'LLEC' and random spots patterns are given in Figures 4.2.2 (a) and (b). The uniformity of the diffracted beams is shown by the measurements of ablated spot diameters ( $\Phi$ ) using the Wyko NT1100 optical surface profiler (Veeco) [130]:  $\Phi_1=20.3\pm 1.2\mu\text{m}$  ('LLEC' pattern) and  $\Phi_2=21.7\pm 1.1\mu\text{m}$  (random spots pattern). The spot size in random spots pattern is significantly larger than 'LLEC' pattern. This might be due to the highly asymmetric pattern design of the random spots pattern, which caused a higher diffractive efficiency. Chapter 6 will give more details about the effects caused by geometric pattern design. To avoid large variations in the required intensity distributions between spots, it is advantageous to avoid patterns with a high degree of symmetry, which is discussed in Chapter 6.

Additionally, there is a modest increase in eccentricity with distance, which is probably mainly due to the finite bandwidth of the laser source. All diffractive optics suffer from the same limitation when used with a broadband source, namely for a given design of CGH, the shift of the focused spot away from the zero order is proportional to the wavelength ( $\lambda$ ) of the spectral component. Accordingly, the spot is elongated by an amount equal to its fractional spectral bandwidth multiplied by the number of equivalent grating line-pairs in the CGH design. For example, the 160fs source has a fractional spectral bandwidth of approximately 0.7% ( $\lambda = 775\text{nm}$ ,  $\Delta\lambda = 5\text{nm}$ ). A spot shifted away from the zero order using a CGH with 25 line-pairs per mm would result in an eccentricity of the diffraction limited focal spot of approximately 2:1, in agreement with the observed results. The laser source bandwidth would therefore appear to set an upper limit on the useful field of view of

the system. Further study on spectral bandwidth caused beam shape distortion will be discussed in 4.2.2.

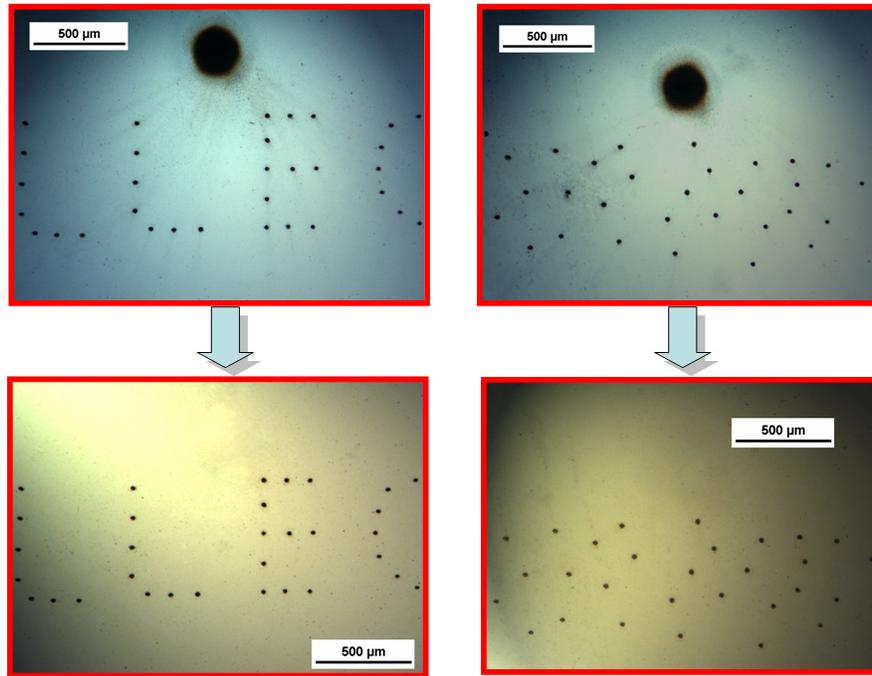


**Fig. 4.2.3:** The zero orders removed when micro-structuring a silicon substrate with the ‘LLEC’ and random spots patterns.

The un-diffracted zero order beam containing approximately 50% of the input pulse energy was blocked by a metallic target at position Q (Figure 3.3.2). Referring to figure 3.3.5, digital camera images show the holographically produced energy distribution of the ‘LLEC’ pattern on a paper screen near the Fourier plane. The +1 order beams contain the majority of the diffractive energy because the CGH was designed to enhance them, while -1 order beams with much lower energy ( $\ll$  the material ablation threshold) leave the substrate unaffected. The lower two pictures of figure 4.2.3 demonstrate the absence of large holes showing that the zero order beam was successfully removed.

## 4.2.2 The distortion of beam shape caused by finite spectral bandwidth

### 4.2.2.1 The observation of distorted beam shape

As mentioned, the observed significant increase in eccentricity when applying a larger diffractive angle was due to the lateral chromatic aberration caused by the finite bandwidth ( $\Delta\lambda$ ) of the laser source [82, 131]. If the input beam has a single wavelength, it will keep the initial round shape after the diffraction, as shown in figure 4.2.4 (a). However, the laser beam, generated by Clark-MXR CPA2010 laser system, had a broad bandwidth,  $\Delta\lambda \approx 5\text{nm}$ . Since the angle of diffraction is proportional to the input wavelength, the components with longer wavelength will have a larger angle of diffraction, while the shorter wavelength components will be diffracted at a smaller angle, hence elongating the beam shape after the diffraction, as shown in figure 4.2.4 (b).

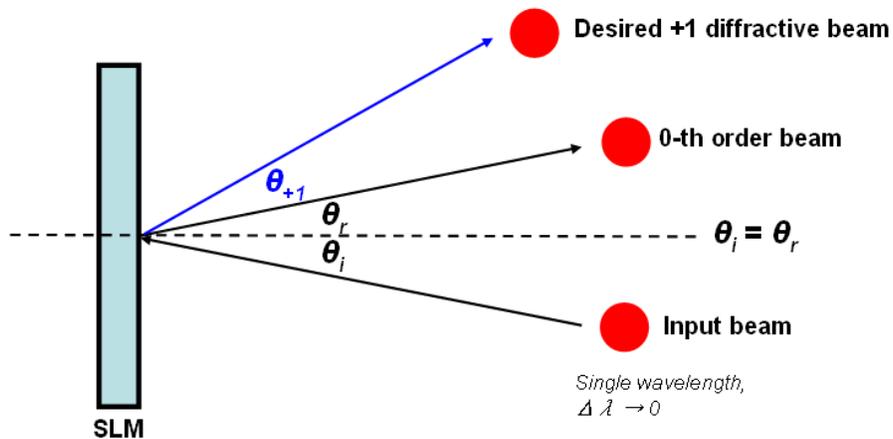


**Fig. 4.2.4 (a):** Illustration of how the desired +1 diffractive beam retains a round shape when the input beam has a single wavelength i.e.  $\Delta\lambda \rightarrow 0$ .

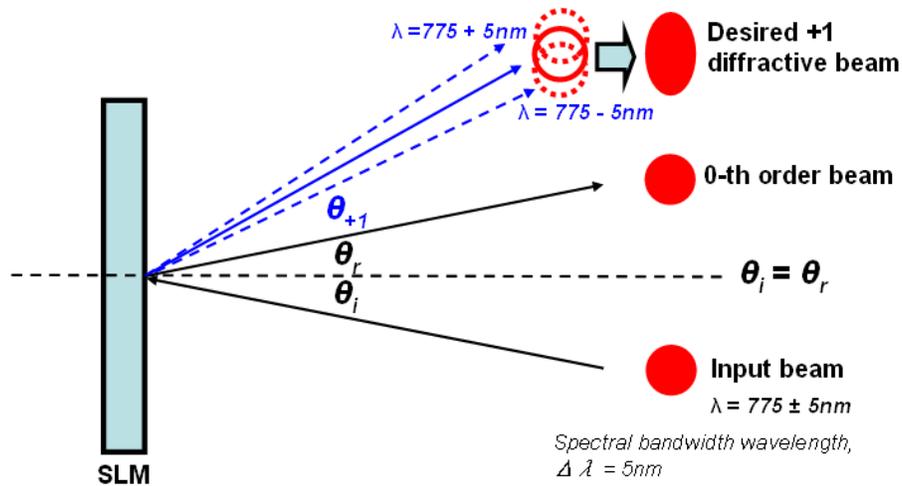


*Fig. 4.2.4 (b): Illustration of how the shape of desired +1 diffractive beam is elongated towards zero order beam when the input beam has a measurable finite bandwidth,  $\Delta\lambda \approx 5\text{nm}$ .*

To investigate this phenomenon further, holes were ablated on silicon with the +1 order laser beams with varying angle of diffraction (figure 4.2.5). Referring to figure 4.2.5 (a), the results show that the long axis of the elliptically fabricated structure was slightly tilted away from the direction towards the zero order beam, instead of aligning with the axis. This may be explained by micro-machining, in this case, at a significant distance from the centre of the flat field of the f-theta lens, where the slight astigmatism of the femtosecond beam becomes apparent if the focus wanders away from the true f-theta plane. The combination of this minor effect and the primary effect of chromatic dispersion led to a rotation of the long axis. Secondly, the ablation debris on the surface is deposited non-uniformly, aligning along the short axis of the ellipse, which is thought to be due to an asymmetric expansion of the plasma following ablation, driven by the much higher intensity gradient along the short axis.

By taking greater care with regard to the SLM alignment in the optical line and positioning the zero order close to the centre of the f-theta lens field, improved results demonstrate that the long axis of the elliptically fabricated structure is indeed aligned to the direction toward the zero order beam (figure 4.2.5 (b)). In this case, the debris was easily removed with methanol and a lens tissue.

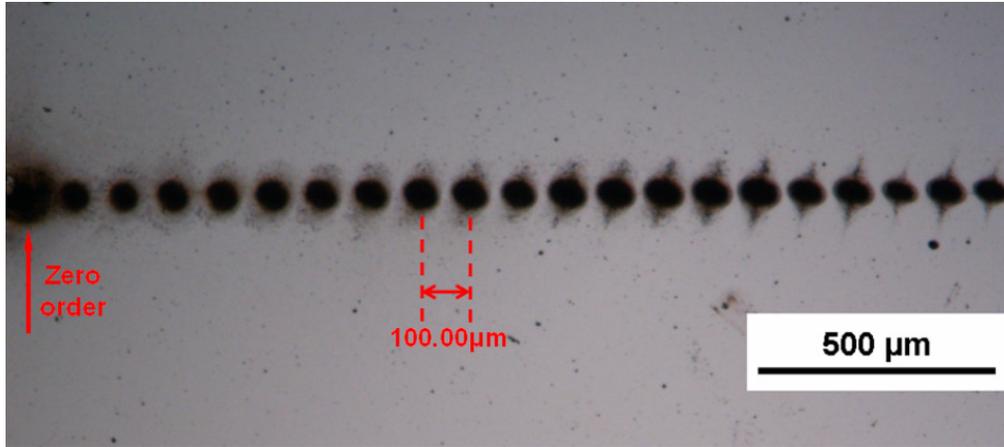


**Fig. 4.2.5 (a):** Observed growing eccentricity of micro-machined holes on a silicon substrate with increasing diffractive angle of +1 orders, showing a slight tilt of the major axis. The ablation debris is deposited non-uniformly due to the asymmetric expansion of the plasma. The zero order is marked.

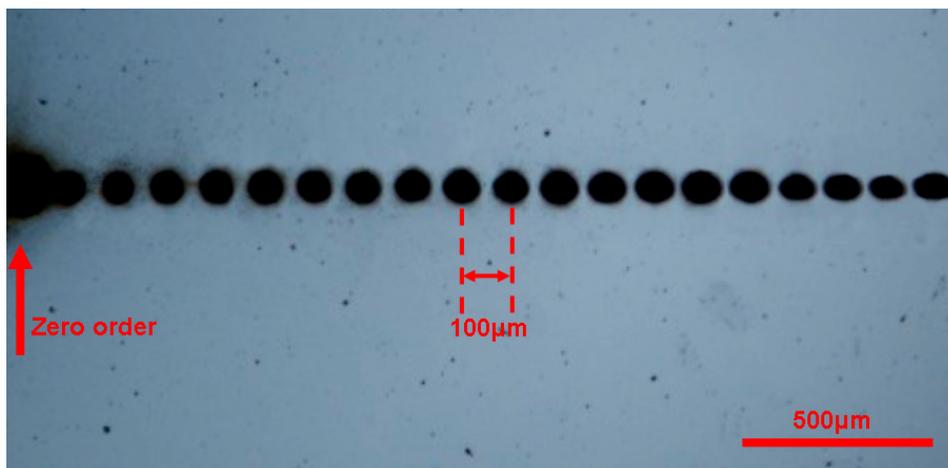


**Fig. 4.2.5 (b):** Improved result over figure 4.2.5 (a) in which the major axis of the elliptical structures aligns to the zero order. The debris has been simply removed using methanol.

#### 4.2.2.2 Prediction of the eccentricity of beam shape by calculation

The bandwidth limitation, mentioned above, is a characteristic of all diffractive optics when used with a broadband source (in this case,  $\Delta\lambda \sim 5\text{nm}$ ). Based on the grating equation,  $\Lambda (\sin\theta_m + \sin\theta_i) = m\lambda$ , where  $\Lambda$  is the grating period and  $m$  is the order of diffraction, the expected variation of eccentricity  $e$  versus diffractive angle can be used to predict the drilled hole shape. Here, the incident angle  $\theta_i$  on the SLM is  $< 10^\circ$ , and +1 order ( $m = 1$ ) diffractive angle  $\theta_{+1}$  is  $< 2^\circ$ , hence  $\sin \theta_{+1} \sim \theta_{+1}$ . The grating equation can be simplified to:  $\theta_{+1} \approx \sin \theta_{+1} = \lambda/\Lambda$ , (where  $\Lambda$  is the grating period.). Hence by differentiating, the following is obtained:

$$\frac{\Delta\theta_{+1}}{\Delta\lambda} = \frac{1}{\Lambda} \text{ or, } \Delta\theta_{+1} = \frac{\Delta\lambda}{\Lambda} \quad (4.2.1)$$

If  $f$  is the focal length of the f-theta lens, the elongation  $\Delta l$  caused by  $\Delta\lambda$  at the focal plane is then:

$$\Delta l = f \cdot \Delta\theta_{+1} = \frac{f}{\Lambda} \Delta\lambda \quad (4.2.2)$$

while the diameter of the focused spot can be calculated from:

$$2\omega_0 = \frac{4M^2 f \lambda}{\pi D} \quad (4.2.3)$$

where  $D$  is the raw beam (spot) diameter and  $M^2 \sim 1$  is the beam quality factor. Thus, the eccentricity  $e$  at a given diffractive angle can be calculated by  $e = a/b \approx (\Delta l + 2\omega_0) / 2\omega_0$ , where  $a$  and  $b$  are the major and minor semiaxis of the elliptical hole shape. Figure 4.2.6 indicates excellent agreement between the experimental and calculated eccentricity,  $e$ , which increases linearly when varying the angle of diffraction.

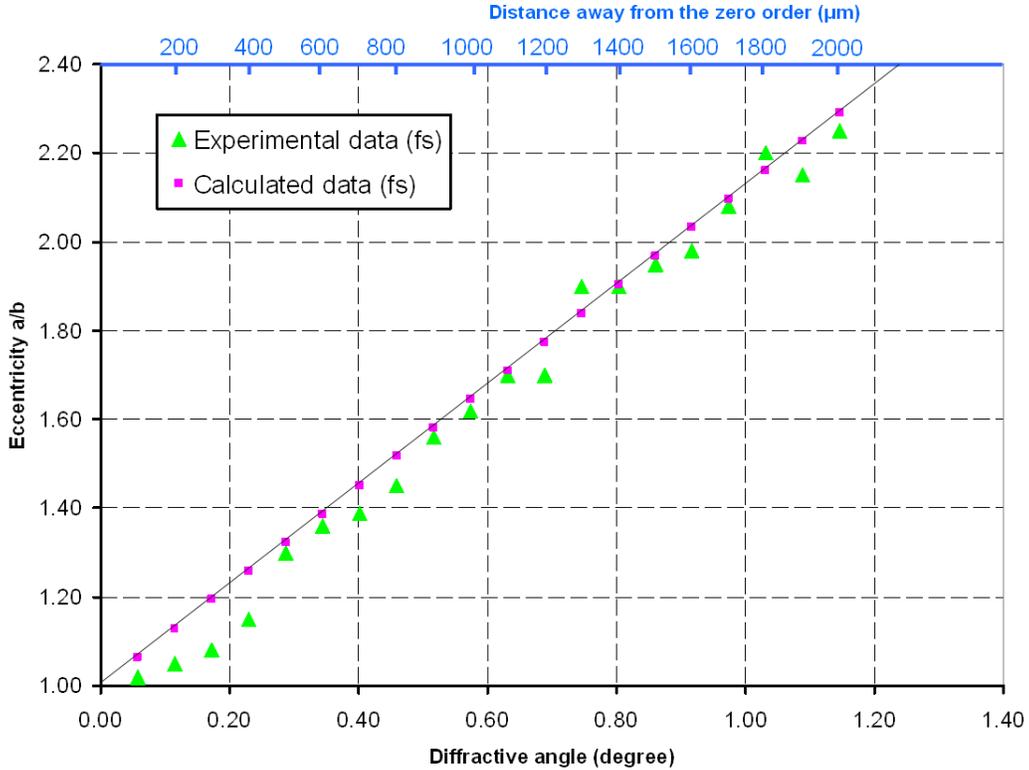


**Fig. 4.2.6:** Experimental and calculated eccentricity  $a/b$  of machined holes versus angle of diffraction showing excellent agreement. Eccentricity increases linearly with angle of diffraction.

#### 4.2.2.3 Effect of beam shape distortion on process stability

The distorted intensity profile at higher angles of diffraction also affects ablation. Figure 4.2.7 shows a comparison of the measured ablation depth on Ti6Al4V with angle of diffraction and pulse number. In each case, pulse energy was  $E_p \sim 5 \mu\text{J}$  and ablation depth decreased with increasing angle of diffraction due to the growing ellipticity of beam shape. Accordingly, to ensure precision femtosecond processing with a 5nm bandwidth (at  $\lambda = 775\text{nm}$ ), the diffracted angle should be limited to  $\theta_{+1} < 0.5$  degree where the eccentricity  $e = a/b < 1.5$ .

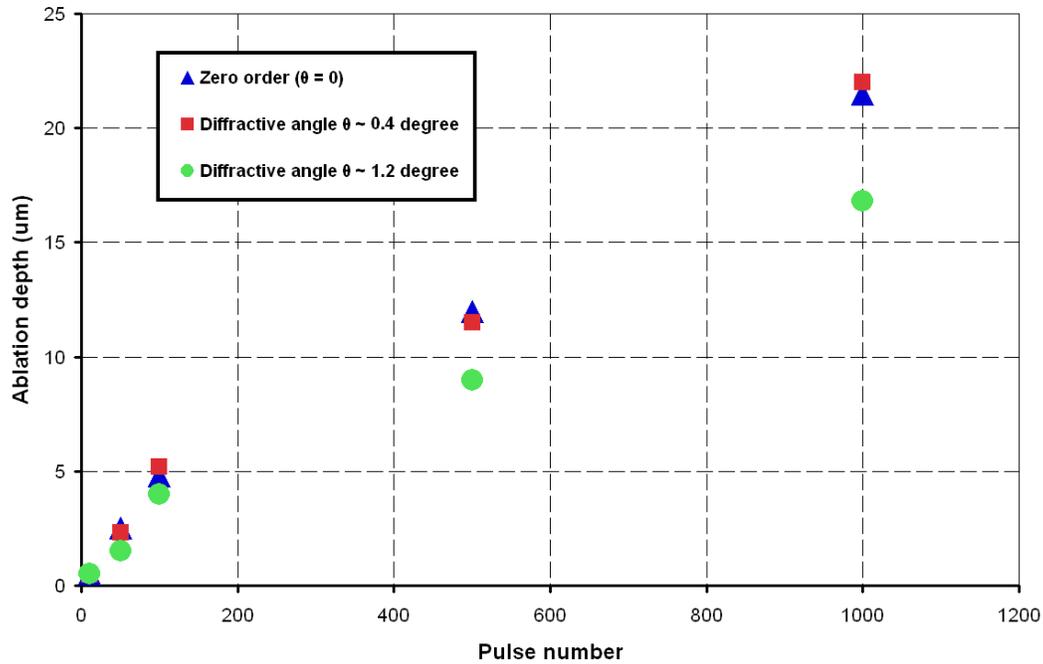


*Fig. 4.2.7: A comparison of ablation depth on Ti6Al4V with angle of diffraction and pulse number, showing that the ablation depth drops at higher angles due to increasing distortion of the intensity profile.*

### 4.3 Laser microprocessing with dynamic diffracted beam patterns

While static holograms are useful and can be combined with the galvanometer system to demonstrate parallel processing with fixed spot geometry, processing by real time control the CGHs is demonstrated in this section.

#### 4.3.1 Response time of the SLM

When addressing a series of CGHs in real time, the playing rate (i.e. the number of CGHs played per second) is significantly restricted by the response time, which is the period of time required to fade out the previous CGH (fall time) and build up a new

one (rise time). In this section, the response time of the Holoeye LC-R 2500, one of the SLMs used for the present research, is investigated.

In the experiment, two CGHs, calculated by the GL algorithm, capable of generating three desired diffractive beams individually, were alternately displayed on the SLM at a 10Hz refresh rate, whilst the laser was scanned in a straight line at a speed of 50mm/s on a polished silicon sample by the scanning galvanometer. Figure 4.3.1 shows an optical micrograph of the machined pattern on the silicon sample, where CGH1 was fading out and CGH2 was building up during the scanning. Due to the quick scanning speed, partially or completely separated single-pulse-machined craters (holes) were produced on the surface of the sample. Since the pulse repetition rate was 1kHz, the period of time between two adjacent holes was 1ms. On the left hand side of figure 4.3.1, towards the scanning direction, the size of the holes machined by the diffracted order beams decreases, while, in contrast, the zero order machined holes increase in size. This indicates the fading out of the CGH1, where the diffracted pulse energy was gradually transferred back to the zero order beam. Similarly, the increase of diffracted beam hole size and the decrease of the zero order beam hole size on the right hand side of the figure represent the time period when CGH2 was gradually building up and the pulse energy was re-diffracted to the desired multiple beams.

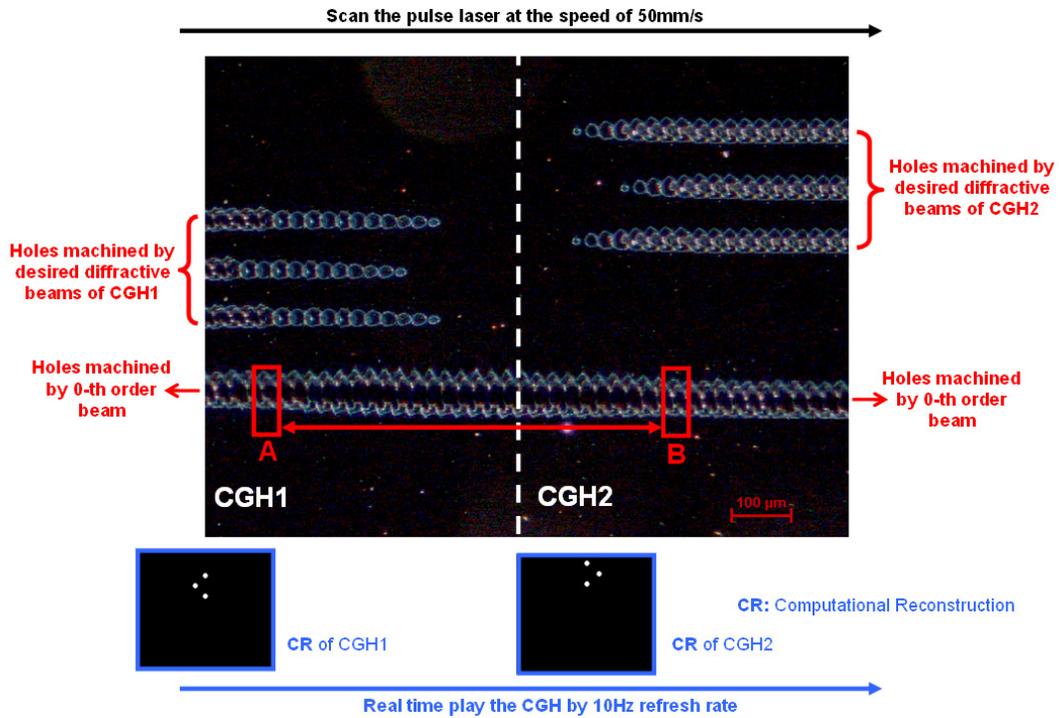


*Fig.4.3.1: Optical micrograph of the machined pattern on a silicon wafer, where the CGH1 was fading out and CGH2 was building up during the scanning. The number of zero order beam machined holes between A and B was 27, and the period of time between two adjacent holes was 1ms; hence the response time was estimated at ~ 27ms.*

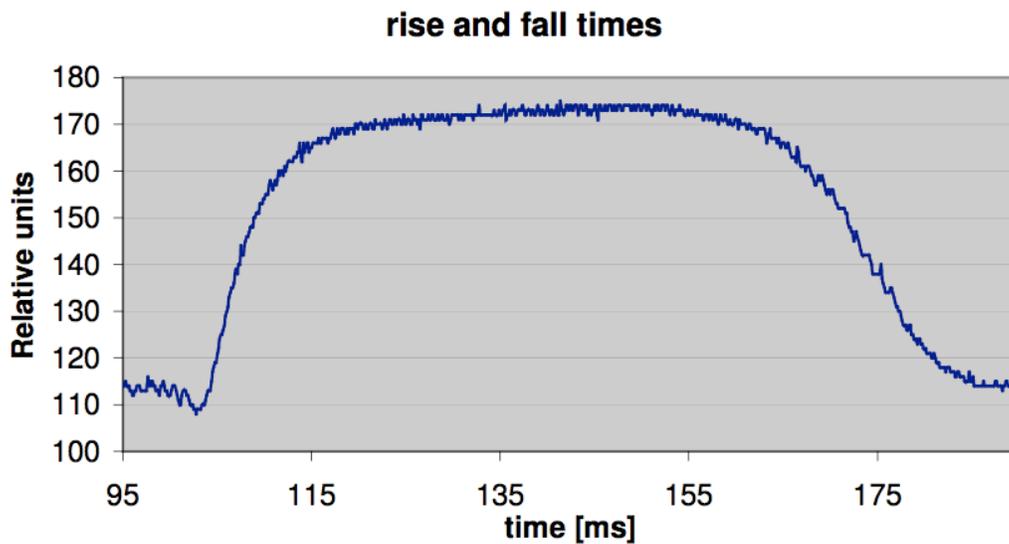


*Fig. 4.3.2: Rise and fall times of SLM (LC-R 2500) given by Holoeye. [97]*

As shown in figure 4.3.1, by counting the number of zero order beam machined craters from A (CGH1 starting to fade out) to B (CGH2 built up completely), the response time was estimated to be ~ 27ms (fall time ~ 17ms, rise time ~ 10ms), which reasonably matches the value given in Holoeye LC-R 2500 specification manual, 28ms (fall time ~ 18ms, rise time ~ 10ms), shown in figure 4.3.2.

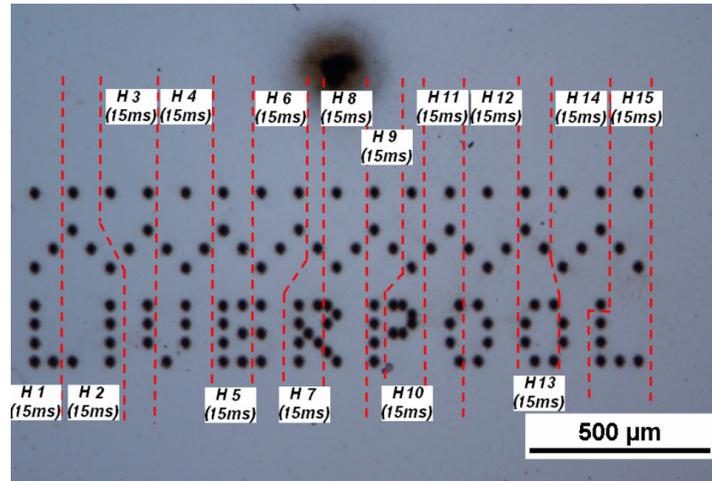
The maximum CGH playing rate is restricted by the response time and should be < 50Hz. However, if there is a little change in the position of the desired diffracted beams when building up the successive CGH, a 50Hz rate of CGH playing also allows perfectly good machining results in parallel processing, which will be demonstrated in section 4.3.2.

### **4.3.2 Micro-processing by real time playing CGHs**

Figure 4.3.3 (a) shows a pattern comprising 121 holes laser machined by real time playing of 15 stored CGHs at 20 Hz refresh rate, and Fig. 4.3.3(b) demonstrates the formation of the pattern, which was completed within 0.75s. The incident pulse energy on the SLM was  $E_p \sim 300\mu\text{J}$ .

Combining real time control of the CGHs with scanning, diffractive multi-beam processing has significant potential to produce complex surface micro-machining patterns. Figures 4.3.4 (a) and (b) illustrate this on a polished Ti6Al4V substrate where 6 micro-channels, a-f were generated by applying the appropriate CGHs at 50Hz refresh rate while simultaneously scanning the diffracted spots at a speed of

1mm/s. The resulting micro-channels a – f, were  $\sim 40\mu\text{m}$  wide and  $\sim 10\mu\text{m}$  deep. The wider channel positioned above the micro channels, was machined by the zero order beam.



4.3.3 (a): Pattern completed by real time playing 15 series of CGHs at 20 Hz refresh rate (50ms duration per CGH).

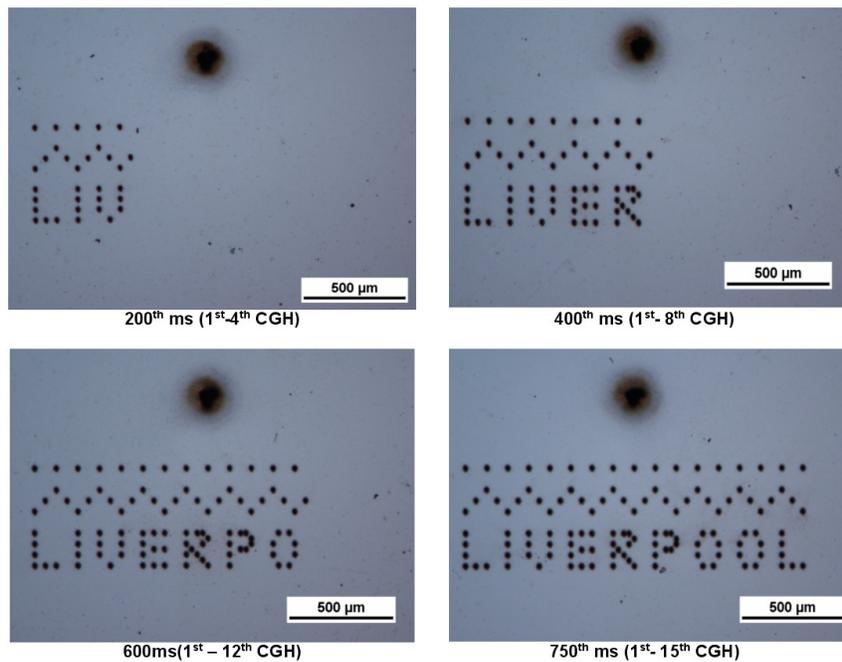
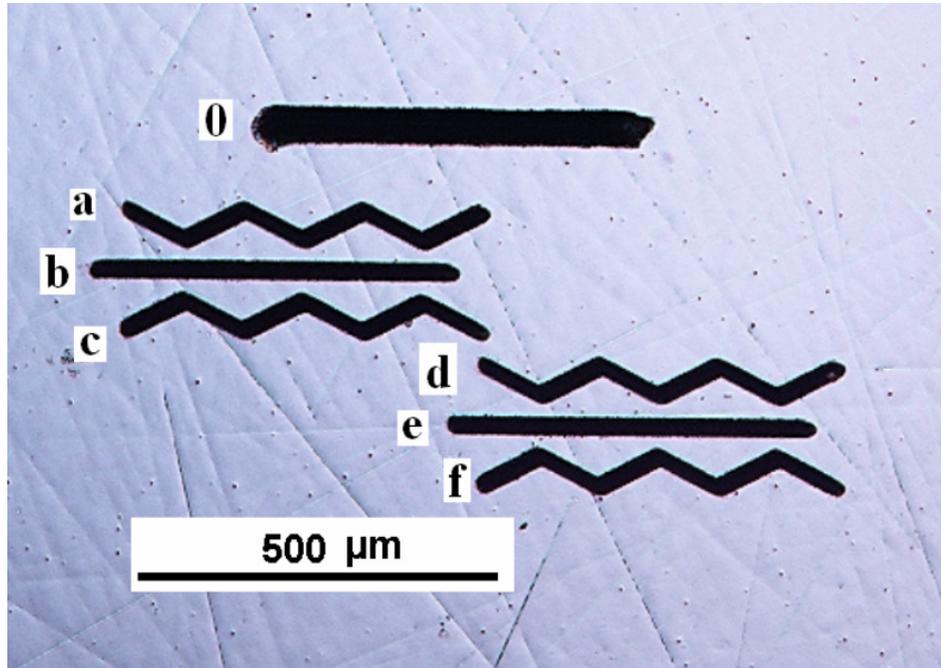
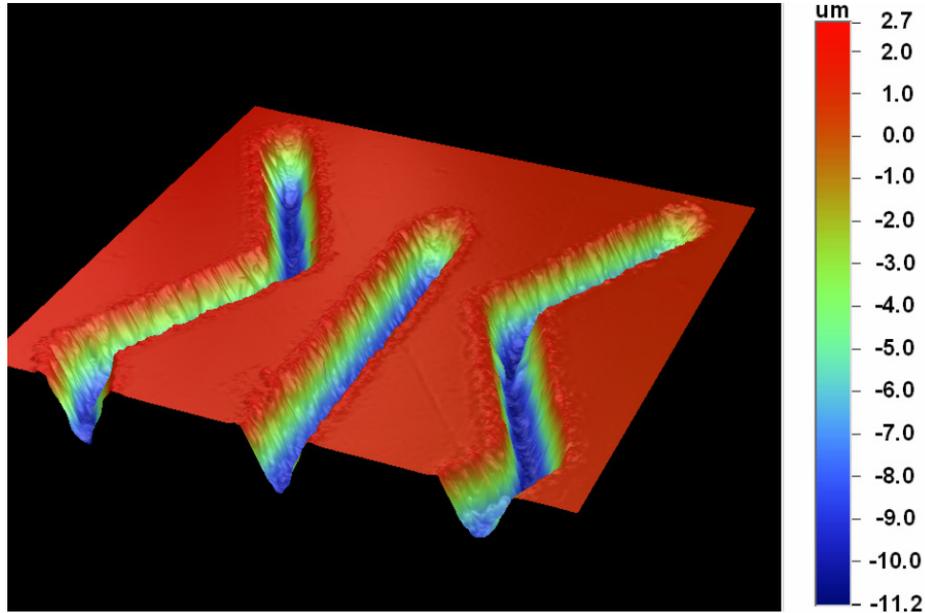


Fig. 4.3.3 (b): The stages in formation of the pattern of figure 4.2.3 (a).



(a) Whole pattern view (5× objective); 6 channels a to f were generated by the diffractive beams while the wider channel 0 above was formed by zero order beam



(b) 3D view by Wyko NT1100 optical surface profiler, where ~10 μm depth (10 times over scan) micro-channels are illustrated

**Fig. 4.3.4:** Micro-channels obtained by combining CGH real time control with Galvanometer scanning.

### 4.3.3 Synchronizing the action of hologram application with scanning techniques

By synchronisation of real time playing holograms with laser beam scanning, 2D surface micro-structuring of Ti6Al4V was achieved and analysed. A pattern ‘OPTICS’ (in Chinese and English) comprising 129 holes processed on a Ti6Al4V substrate using 7 CGHs combined with the galvanometer scanner is shown in figure 4.3.5, while figure 4.3.6 shows the pattern with zero order removed. The incident pulse energy on the SLM was  $E_p \sim 150\mu\text{J}$ , and the measured hole diameter ( $\Phi \sim 25\mu\text{m}$ ) and depth ( $\sim 2.3\mu\text{m}$ ) corresponds to an exposure time of 200ms (i.e. 200pulses), with pulse energy  $E_p \sim 5\mu\text{J}$  in each +1 diffracted order beam. As each CGH generated more than 15 higher order holes simultaneously, a throughput gain factor  $G > 15$  was demonstrated compared to single beam processing in this case.

The material samples chosen for this research were silicon wafer (a significant semiconductor widely used in the fabrication of integrated circuit and other microdevices) and Ti6Al4V (a metallic alloy extensively used in aerospace and bioscience). Both materials have a relatively low threshold for femtosecond pulse induced laser ablation. Thus, when using a single beam to machine, significant attenuation would be needed to provide a pulse energy just above the threshold, hence resulting in low processing efficiency. Here, however, the above results from parallel processing demonstrate great advantages in term of increasing both processing throughput and efficiency.

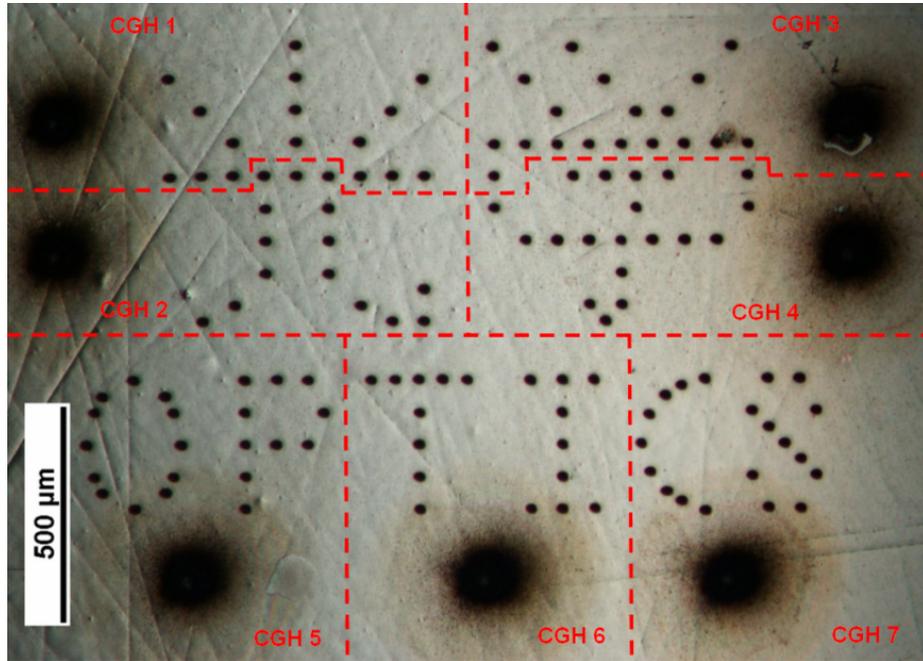


*Fig. 4.3.5: 'OPTICS' pattern created by 7 CGHs applied at appropriate positions using the galvanometer scanner (shown together with zero order holes).*

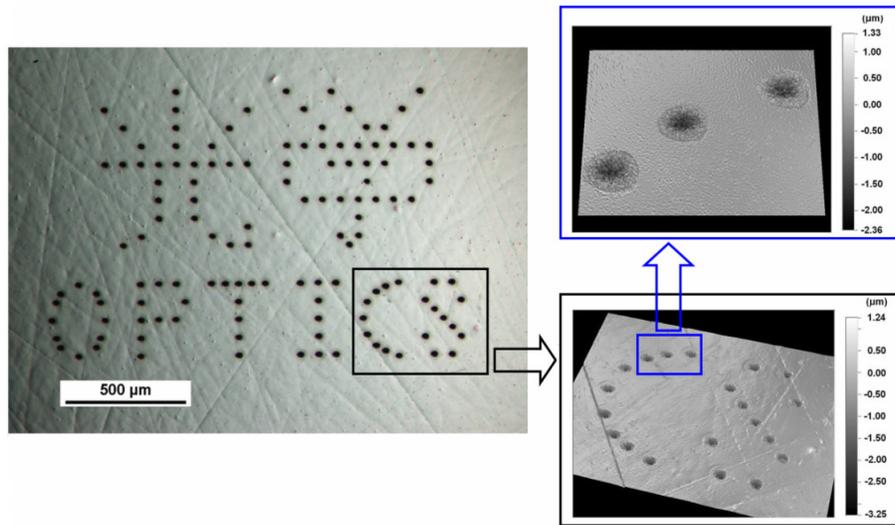


*Fig. 4.3.6: 'OPTICS' pattern with zero order holes eliminated (The insert 3D pictures were measured using Wyko NT1100 optical surface profiler, illustrating the depth of the holes).*

## **4.4 Summary**

The results obtained from multiple diffracted beam laser microprocessing using femtosecond pulses demonstrate that precision ultrashort pulse laser micro-structuring using an SLM in this approach is a novel method to increase processing efficiency and throughput. Pulse energies up to 300 $\mu$ J at 1kHz repetition rate were diffracted into > 30 spots with 50% efficiency. This constitutes a throughput gain > 1 order of magnitude for precision micro-structuring tasks requiring micro-joule level pulse energies. Additionally, the ability to address CGHs in real time and synchronize with the scanning method adds an additional flexibility for surface micro-structuring. This work has been published in peer reviewed journals [88, 89].

However, caused by the finite bandwidth ( $\Delta\lambda \sim 5\text{nm}$ ) of the laser source, the elongation of the machined holes, which was observed, and correctly predicted by our simple calculation based on the grating equation, highlights a potential limitation of parallel processing using an SLM with femtosecond laser pulses. Therefore, the picosecond laser system (High-Q IC-355-800ps), which generates 10ps duration pulses with much narrower spectral bandwidth ( $\Delta\lambda \sim 0.1\text{nm}$ , at 1064nm output), can make the spectral distortion negligible. This was employed to perform diffracted multi-beam microprocessing, and will be detailed in Chapter 5.

## **Chapter 5**

# **Diffractive multiple beam microprocessing using picosecond laser pulses**

## 5.1 Introduction

A picosecond laser system (High-Q IC-355-800nm) with narrow spectral bandwidth ( $\tau \approx 10\text{ps}$ ,  $\Delta\lambda \approx 0.1\text{nm}$ ) was employed for diffractive multiple beam processing. Compact solid state picosecond laser systems ( $\tau < 15\text{ps}$ ) with high pulse energy, high average power and high repetition rate, have advantages over femtosecond systems for high precision micro-machining [42-47]. The distortion of the intensity profile at high diffracted angle is eliminated due to the narrower spectral bandwidth of the laser source compared to a femtosecond laser. The drilled holes retained a near perfect round shape (eccentricity:  $e < 1.04$ ) when applying a large diffractive angle ( $\theta \approx 1.27^\circ$ ). The successful achievement of high power (2.5W) parallel processing with 25 diffracted beams and 20kHz laser repetition rate demonstrated the industrial potential of this precision laser micro-processing.

## 5.2 Experiment setup

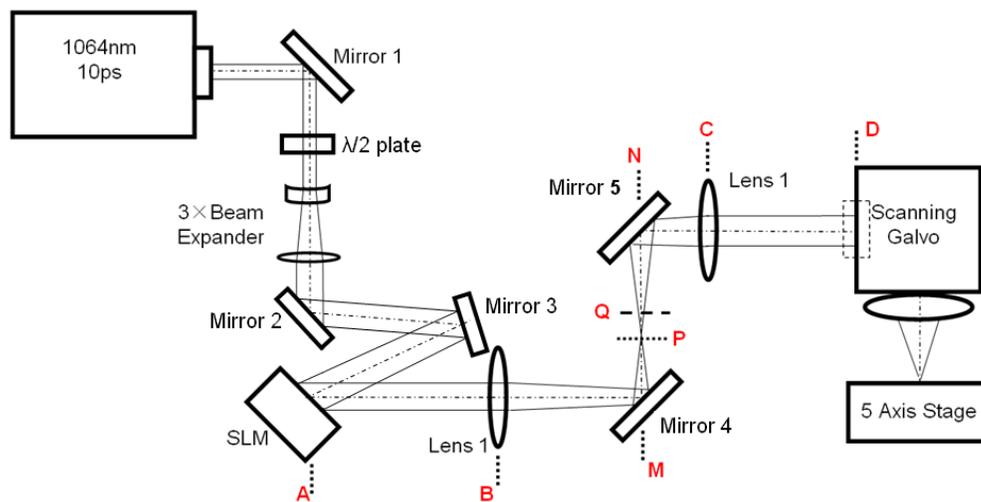


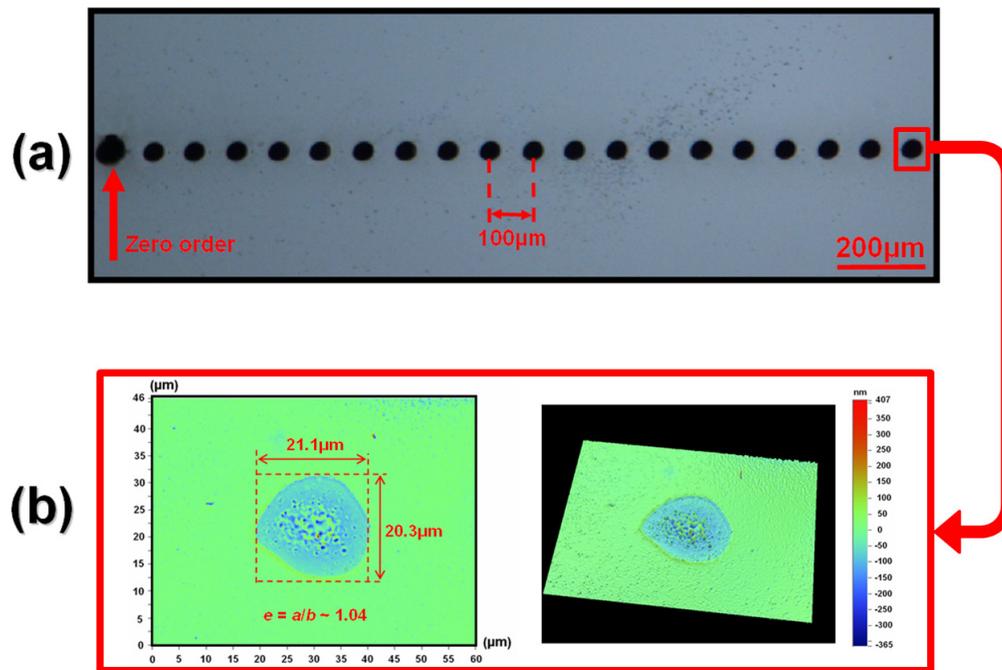
*Fig. 5.2.1: The schematic of experiment setup for High-Q IC-355-800ps with a 4f optical system.*

The picosecond laser system used for the work here was a custom made seeded Nd:Vanadate regenerative amplifier laser system (High-Q IC-355-800ps, Photonics Solutions [34]), as introduced in Chapter 3. Figure 5.2.1 shows the schematic of the experimental setup. The 10 ps output beam ( $\lambda = 1064\text{nm}$  or  $532\text{nm}$ ) traversed a half wave plate used for adjusting the linear polarization direction, a beam expander ( $M \approx 3$ ) and, after reflection on mirrors 1, 2 and 3, illuminated a reflective phase only SLM (Hamamatsu X10468-03 or 04). This was a liquid crystal on silicon (LCoS) device with  $800 \times 600$  pixels and dielectric coated for  $1064\text{nm}$  or  $532\text{nm}$  wavelength (Reflectivity  $\eta \approx 95\%$ ), respectively, oriented at  $<10$  degree angle of incidence. A 4f-optical system was formed from A to D to remove the unwanted 0-th order beam. The modulated beam entered a scanning galvanometer with  $f = 100\text{mm}$  flat field  $f$ -theta lens (Nutfield) producing a near perfect focusing system. Substrates were mounted on a precision 5-axis (x, y, z, p, q) motion control system (Aerotech) allowing accurate positioning of the substrate surface at the laser focus. The spectral bandwidth,  $\Delta\lambda \approx 0.1\text{nm}$ , was relatively narrow and important in eliminating any chromatic dispersion from the SLM.

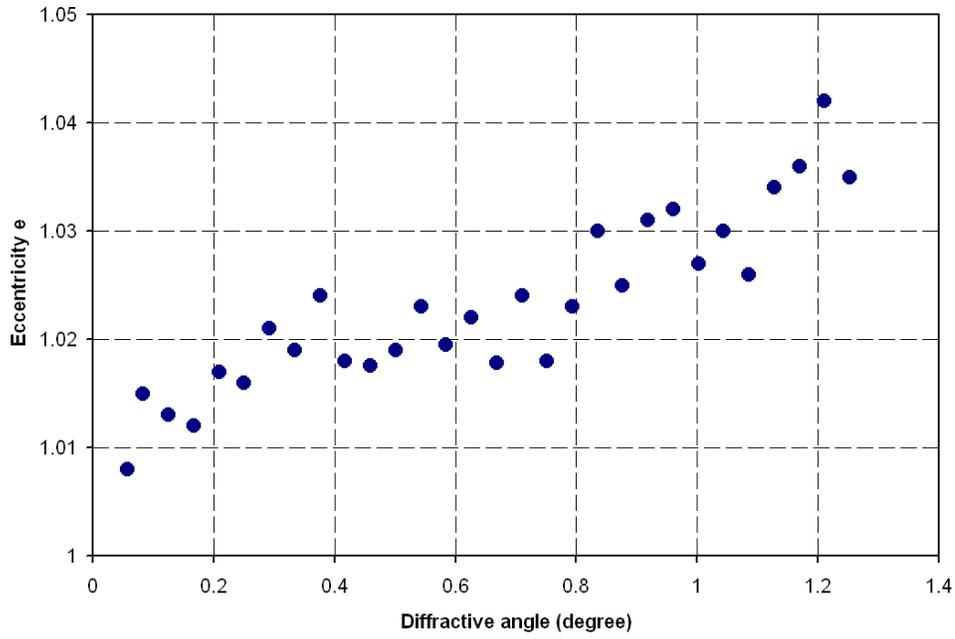
### 5.3 Spectral bandwidth effect on diffracted beam shape

Figure 5.3.1 (a) shows a series holes drilled on a silicon sample using 10ps ( $\lambda_0 \approx 1064\text{nm}$ ,  $\Delta\lambda \approx 0.1\text{nm}$ ) pulses when varying the diffractive angle. Figure 5.3.1 (b), the 2D (left) and 3D (right) micrographs with large magnification clearly show the reasonably round hole shape when applying a large angle of diffraction ( $\theta > 1^\circ$ ). The eccentricity  $e = a / b$  of these drilled hole shape as a function of diffractive angle is plotted in figure 5.3.2, and shows that  $e$  increases only very modestly,  $e < 1.04$ . Figure 5.3.3, shows that there is a negligible variation of ablation depth (1000 pulses,  $E_p \approx$

5 $\mu$ J) with increasing angle of diffraction, demonstrating a high degree of reproducibility of diffractive multi-beam processing. The above results indicate that the elongation of diffracted beam shape caused by chromatic distortion can be eliminated by employing picosecond laser pulses ( $\tau \approx 10$ ps) with narrower bandwidth, hence allowing constant ablation rate.



**Fig. 5.3.1:** (a) A series holes drilled on a silicon sample when varying the diffractive angle. (b) The 2D (left) and 3D (right) micrographs with large magnification, showing the shape of the hole, fabricated by single 10ps pulse, when applying large diffractive angle,  $\theta > 1^\circ$ .



*Fig. 5.3.2: The eccentricity  $e$  of hole shape drilled by 10ps when varying the angle of diffraction.*

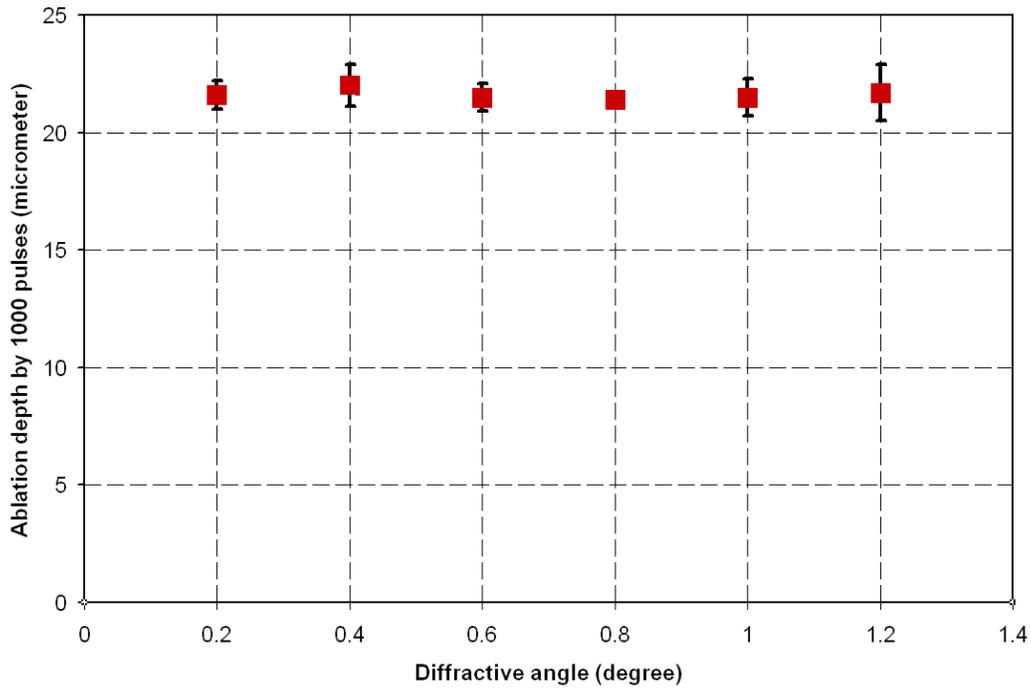


*Fig. 5.3.3: The variation of ablation depth using one thousand 10ps pulses ( $E_p \approx 5\mu J$ ) when varying the angle of diffraction.*

### 5.4 High power parallel processing with high repetition rate at $f = 20\text{kHz}$

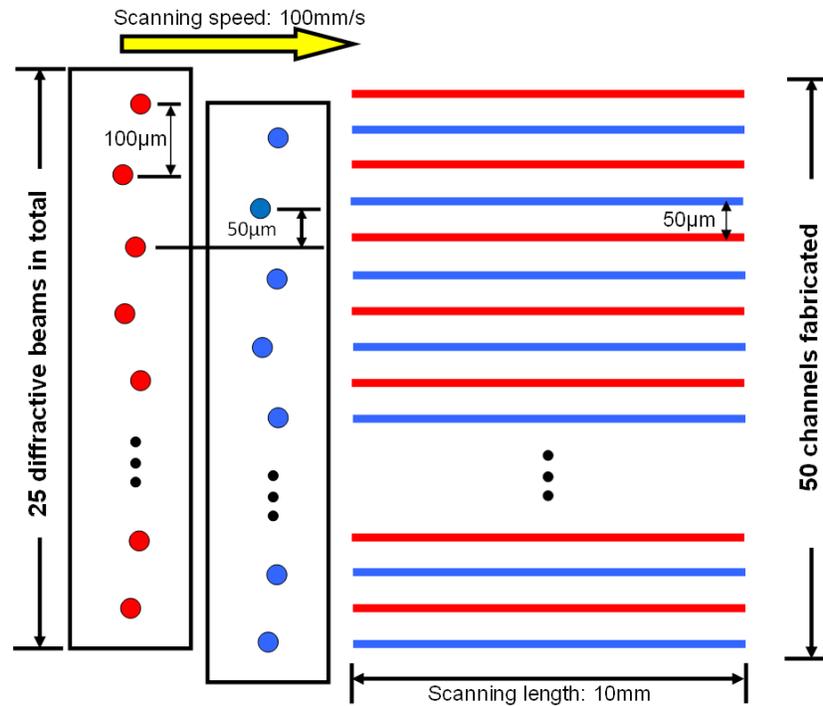


*Fig. 5.4.1: Schematic showing the design of the 25 beams pattern and the method of scanning. (The vertical distance between two adjacent spots was  $100\mu\text{m}$ ; by repeatedly scanning the pattern with  $50\mu\text{m}$  vertical offset each time, multiple micro-channels with  $50\mu\text{m}$  intervals can be obtained.).*

With the ps system ( $\tau \approx 10\text{ps}$ ) operating at high repetition rate ( $f = 20\text{kHz}$ ) and maximum output ( $P_{\text{average}} \sim 2.5\text{W}$ ), parallel processing was demonstrated, using a 25 diffractive beams pattern, created by a CGH calculated by the 2D Gershberg-Saxton (GS) algorithm. The schematic given in figure 5.4.1 demonstrates the design of the beams pattern and the method of scanning, while the micrographs in figure 5.4.2 show the micro-machining results on a polished Ti6Al4V sample. A  $10 \times 10\text{mm}$  surface area was processed by covering it with  $\sim 2\mu\text{m}$  deep micro-channels at  $50\mu\text{m}$  intervals and overscanned 20 times at a scan speed  $100\text{mm/s}$ , in a time of 16s. The channels

created were very uniform and had a width of  $25.3 \pm 0.4 \mu\text{m}$ , indicating the accuracy of CGH calculation using the GS algorithm. The diffractive efficiency was measured at  $\sim 50\%$ , allowing  $> 1.2\text{W}$  to be diffracted into 25 parallel beams. This had the effect of creating an "effective" repetition rate of 500kHz without encountering the limit of the galvanometer scanning speed.

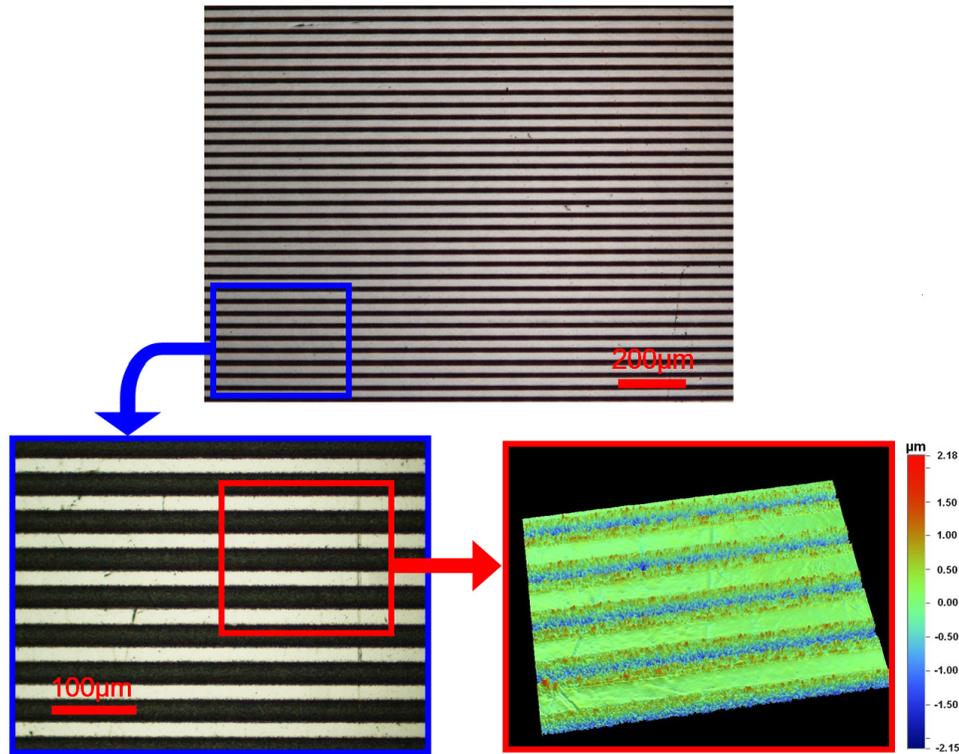


**Fig. 5.4.2:** Micrograph demonstrating the results of micro-channels covering a  $10 \times 10\text{mm}$  area machined by the 25 beams pattern on polished Ti6Al4V (upper), and micrographs showing the result with higher magnification (lower left) and 3D surface profile image by Wyko NT1100 optical surface profiler (lower right).

## 5.5 Summary

Microprocessing with the diffractive multiple beams derived from 10ps laser pulses has been discussed in this chapter. The machined holes were found to be perfectly round, independent of angle of diffraction and hence demonstrating the advantage of parallel processing using ultrashort pulses with picosecond pulse duration and narrow

spectral bandwidth. Furthermore, simultaneously scanning of multiple diffracted beams ( $n = 25$ ) containing  $> 1.2\text{W}$  average power with higher repetition rate (up to)  $f = 20\text{kHz}$  successfully yielded high throughput surface micro-structuring, by creating an "effective" repetition rate of  $500\text{kHz}$ , which would otherwise not have been possible due to the maximum scan speed of the galvanometer mirrors. This work has been published in a peer reviewed journal [90].

## **Chapter 6**

# **Uniformity study of diffractive laser beam patterns**

## 6.1 Introduction

The uniformity of the diffractive pattern is a significant parameter, since many industrial applications would require that all the diffractive beams have a good identity to ensure consistent processing.

As reported by Curtis et al.[118], the uniformity of the diffractive pattern is not only affected by the algorithm used to calculate the CGH, but also the geometric design of the diffractive pattern. A slight spatial disordering of periodic and symmetric patterns can significantly reduce intensity variations among each of the desired diffractive peaks. A better uniformity of diffractive pattern has been demonstrated by improving the CGH calculation algorithm, e.g. adding iterative calculations to minimize the uniformity error of the computationally reconstructed diffractive peaks [81, 102], or taking into account of the intensity distribution of the irradiated laser pulse and the spatial frequency response of the SLM [81, 83, 87]. However, there are no reports that experimentally studied the change of the pattern uniformity by control of the geometric design of diffractive pattern.

This chapter will demonstrate the experimental results showing the change of uniformity by varying the geometric pattern design.

## 6.2 Methodology of the uniformity study

### 6.2.1 Geometric design of the diffractive pattern

Two typical CGH calculation algorithms, the Lenses and Gratings (non-iteration) [102, 103] and the Gerchberg-Saxton (iteration) [117], were adopted for this uniformity study.

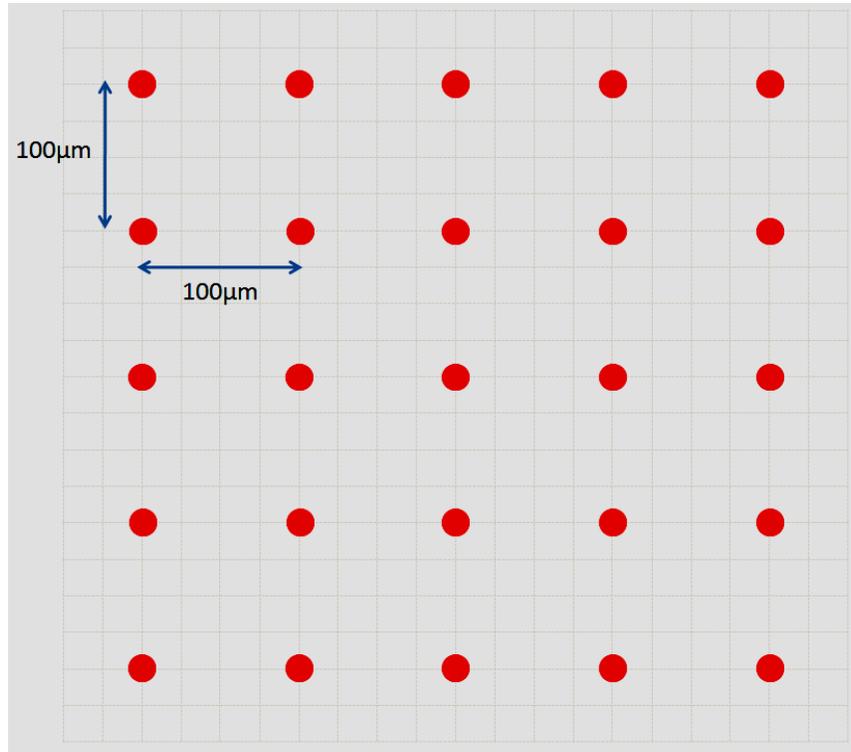


*Fig. 6.2.1: The periodic 5×5 array with high degree of symmetry - the basic geometric design of a diffractive pattern.*

A periodic 5×5 array with high degree of symmetry, shown in figure 6.2.1, was the basic geometric design of the diffractive pattern. To quantitatively control the degree of symmetry, each of the designed diffractive order beams in the pattern was given a freedom of asymmetry ( $R$ ), and they hence no longer had a fixed position, but were located randomly within a circle area (centre:  $(\rho_i, \rho_j)$ ; Radius =  $R$ ), shown in figure 6.2.2.

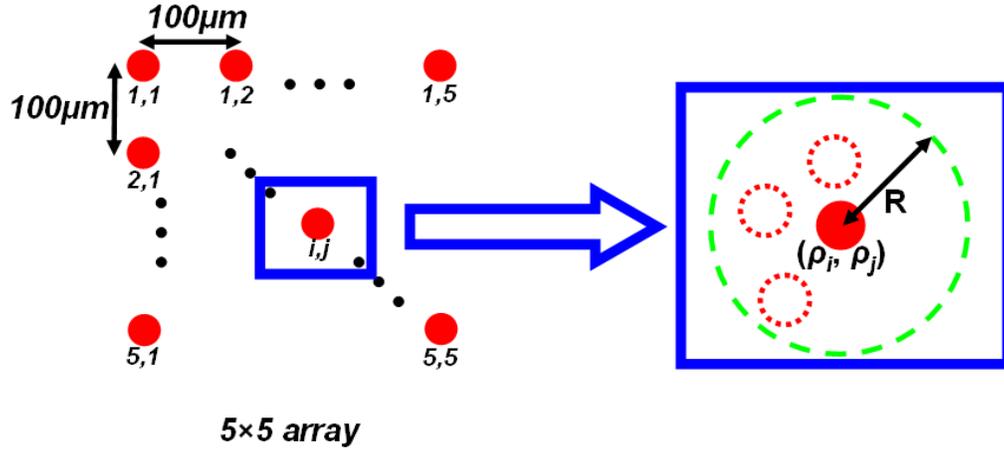


*Fig. 6.2.2: Schematic showing that by applying a freedom of asymmetry,  $R$ , the position of each desired diffractive peaks is no longer fixed, but randomly located within a circle area.*

### 6.2.2 The uniformity measurement

The uniformity of the diffractive patterns can be quantitatively described by calculating the standard deviation,  $\sigma$ . In this study, the diameter of each micro-sized hole machined by the diffracted beams,  $D_1, D_2, D_3 \dots D_n$ , was first measured, and then an average value  $\bar{D}$  was calculated from:

$$\bar{D} = \frac{1}{n} \sum_{i=1}^n D_i \quad (6.2.1)$$

Accordingly, the standard deviation was calculated from:

$$\sigma = \sqrt{\frac{1}{n} \sum_{i=1}^n (D_i - \bar{D})^2} \quad (6.2.2)$$

Finally, the percentage variation was analysed to quantitatively describe the uniformity of the diffracted beam patterns according to the following calculation.

$$V = \frac{\sigma}{\bar{D}} \times 100\% \quad (6.2.3)$$

## 6.3 Results of uniformity study

### 6.3.1 Diffraction efficiency and uniformity resulting from the geometric pattern design

The optical micrographs in figure 6.3.1 show the machining results on a polished Ti6Al4V substrate using the LG algorithm, and show the change of the pattern uniformity by varying the freedom of asymmetry. Figures 6.3.2 shows the diffractive efficiency (a), the total fraction of light directed to the desired multiple beams, and uniformity (b) versus the freedom of asymmetry,  $R$ , where the applied CGHs were calculated using two different algorithms, the Lenses and Gratings (LG) and the Gerchberg-Saxton (GS). Each data point in the figures represents the average value calculated from five different random patterns given the same freedom of asymmetry,  $R$ .

As shown in the graphs, the asymmetrically designed geometric pattern ( $R > 20\mu\text{m}$ ) greatly improves the uniformity and diffraction efficiency. For symmetric patterns ( $R < 20\mu\text{m}$ ), the iterative GS algorithm clearly outperforms the LG algorithm. Nonetheless, by increasing of the freedom of asymmetry ( $R$ ), both uniformity and diffraction efficiency were greatly improved using the LG algorithm, matching (and even slightly surpassing) the results using the GS algorithm.

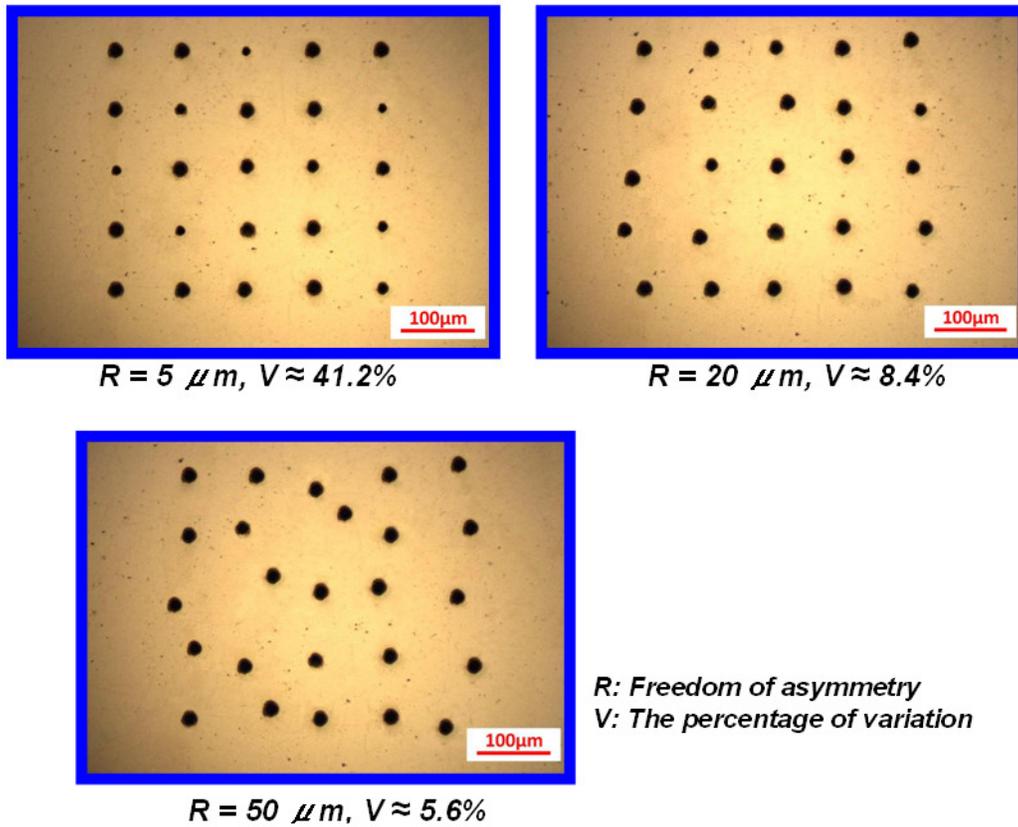


**Fig. 6.3.1:** Optical micrographs showing the machining results on a polished Ti6Al4V substrate using the LG algorithm when the freedom of asymmetry was set to be:  $R = 2 \mu\text{m}$ ,  $20 \mu\text{m}$ , and  $50 \mu\text{m}$ . Clearly, the pattern with a high degree of symmetry, shows poor uniformity, e.g. When  $R = 2 \mu\text{m}$ ,  $V \approx 41.2\%$ , while more an asymmetrically designed pattern has good uniformity, e.g. When  $R = 50 \mu\text{m}$ ,  $V \approx 5.6\%$ .

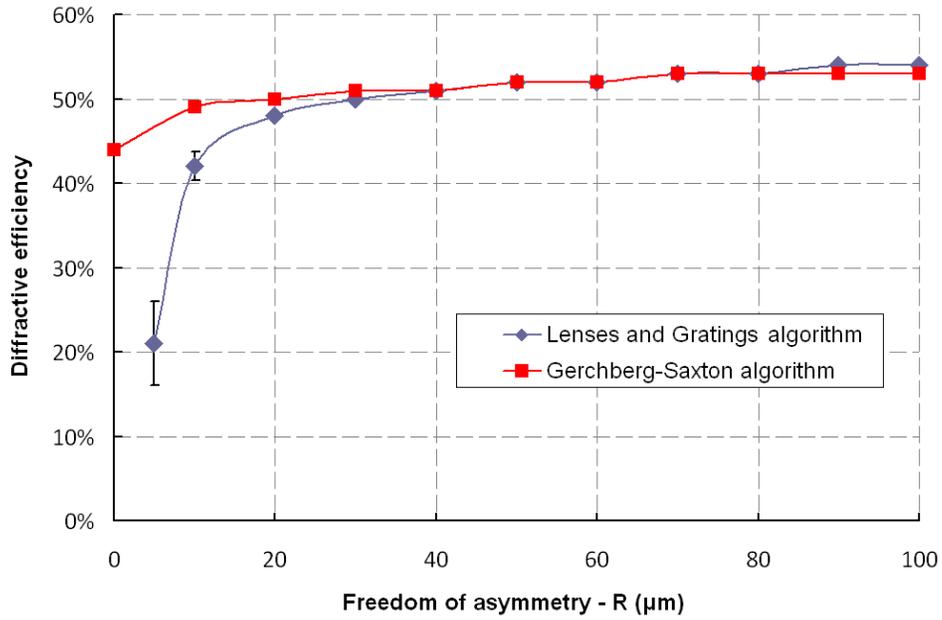


*Fig. 6.3.2 (a): The diffractive efficiency of the multi-beam pattern versus the freedom of asymmetry, R.*

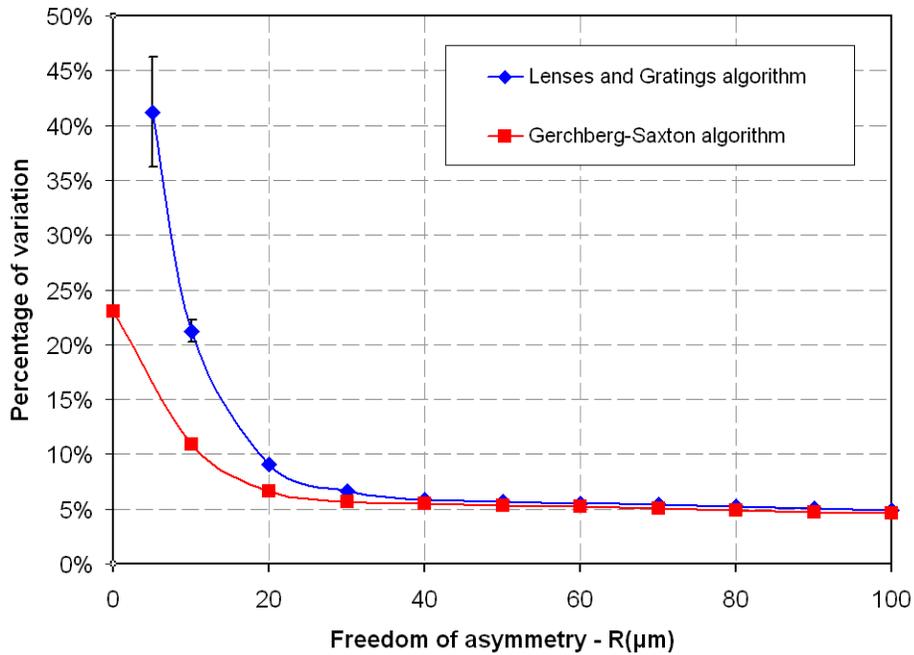


*Fig. 6.3.2 (b): The uniformity of the machined holes on a Ti6Al4V substrate (described by the Percentage of Variation) versus the freedom of asymmetry, R.*

### 6.3.2 Generating symmetric patterns by combination of several asymmetric patterns with good uniformity

To generate a uniform periodic or symmetrical pattern (e.g. a beam array), the pattern can be separated into several asymmetric parts playing one after another at a given rate with a synchronization of the scanning motion.

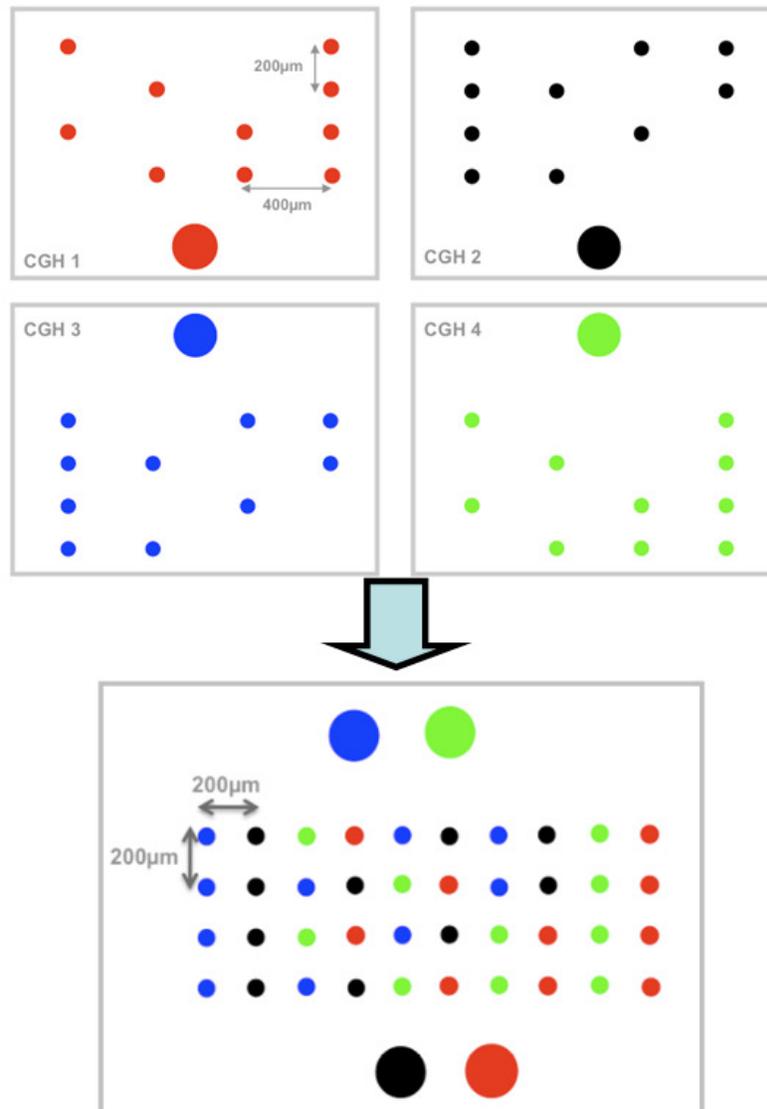


*Fig. 6.3.3 (a): The design of a 10x4 hole array pattern formed by four asymmetric patterns.*

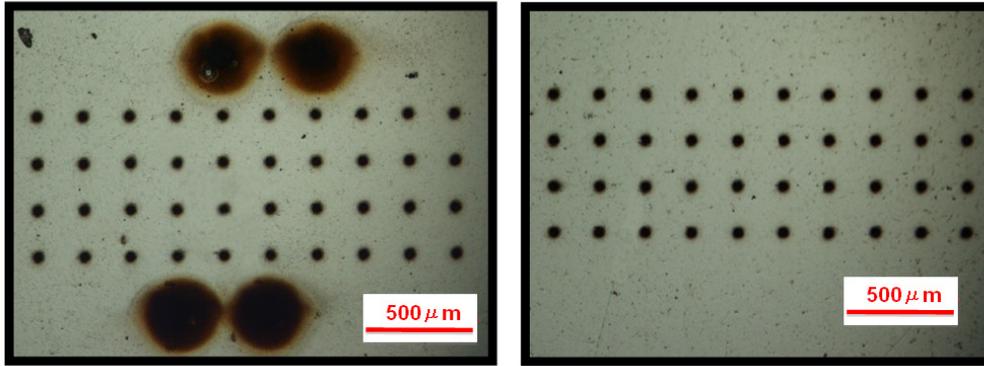


**Fig. 6.3.3 (b):** The processing results of 10×4 holes array pattern with (left) and without (right) zero order holes.

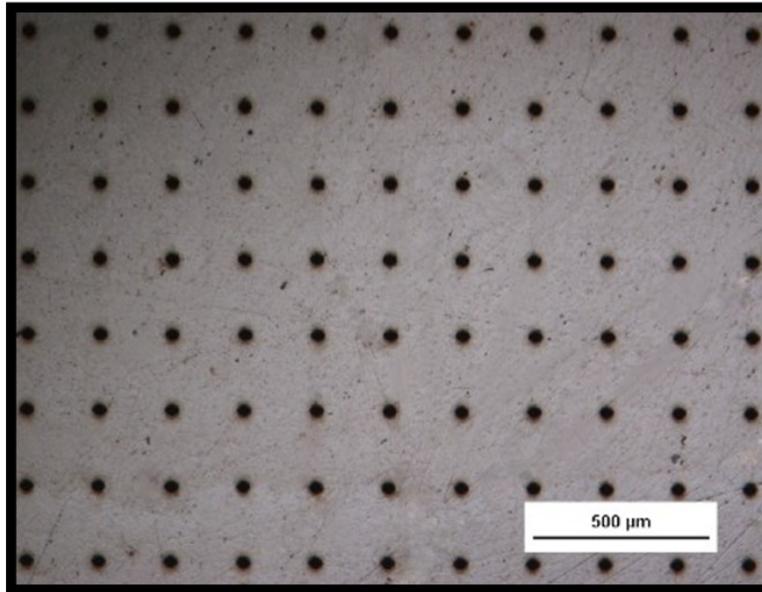


**Fig. 6.3.3 (c):** The result produced by repeating the patterns with the galvanometer system to create large area processing.

Figure 6.3.3 (a) illustrates the design of a 10×4 hole array pattern formed by four asymmetric parts ensuring good uniformity of the desired beams. Figure 6.3.3 (b) shows the processing results on a polished Ti6Al4V substrate with incident pulse energy,  $E_p \sim 100\mu\text{J}$ , on the SLM. As shown, the machined holes were reasonably uniform ( $\Phi = 25.3 \pm 1.6\mu\text{m}$ ) and round (maximum eccentricity  $a/b < 1.5$ ). Figure 6.3.3

(c) shows this pattern repeated using the scanning galvanometer hence increasing the processing area.

By using the patterns created by the offset holograms of figure 6.3.3 (a), while scanning with the galvanometer, a 3D chessboard type structure was created in real time by scanning  $200\mu\text{m} \times 200\mu\text{m}$  squares ( $10\mu\text{m}$  offsets,  $10\text{mm/s}$ ) and varying numbers of overscans ( $n$ ). Here, CGH1 and 2 were applied with  $n_1 = 50$ , generating a  $5\mu\text{m}$  deep structure ( $d_1$ ), while, CGH3 and 5 were applied with  $n_2 = 10$ , creating shallower structures with  $d_2 \sim 1\mu\text{m}$ . (figures 6.3.3 (d) and (e)).

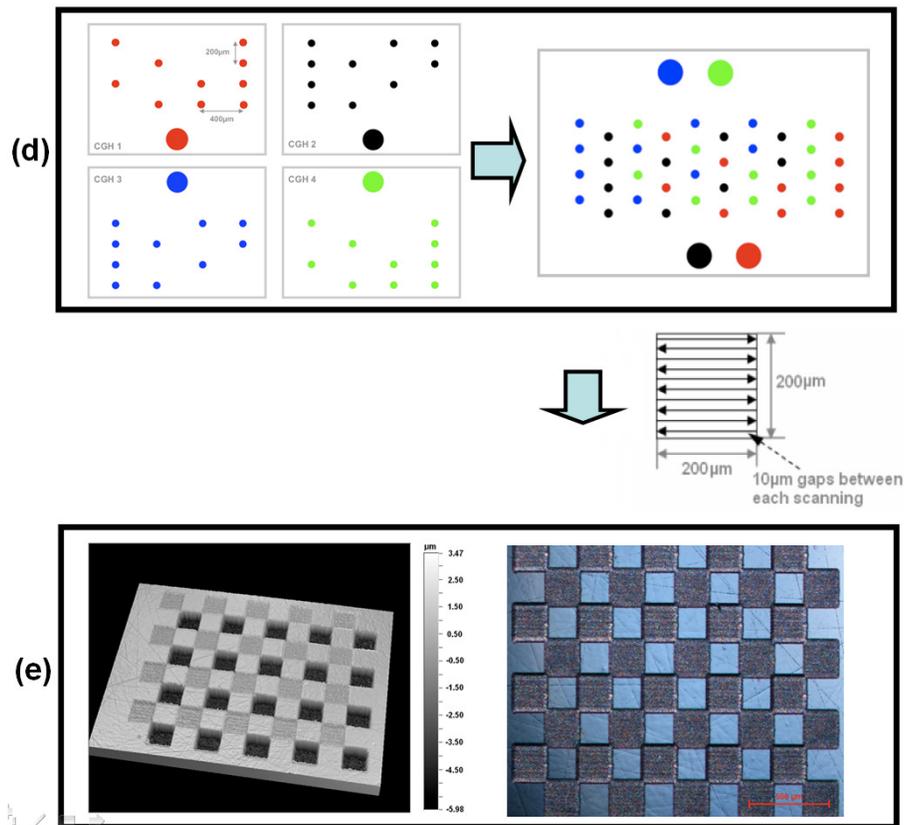


**Fig. 6.3.3 (d) and (e):** Schematic showing the combination of the four asymmetric patterns used to generate a 3D chessboard-like structure (d), and the micro-machined 3D chessboard structure (e).

## 6.4 Discussion

### 6.4.1 The degeneracy of the design pattern

Unwanted diffractive intensity peaks may be generated with the desired multiple beams. These peaks are sometimes called ‘ghosts’ in the literature [118]. A simple example of ghosts is the higher-order diffraction peaks produced by a phase grating. This grating, equivalent to a prism, deflects a +1 order beam to a position  $(\rho_x, \rho_y)$  by imposing the phase  $\varphi \propto \boldsymbol{\rho} \cdot \mathbf{r}$ , where  $\mathbf{r}$  is the hologram coordinate. The weaker higher-order beams also appear in predictable positions, as shown in figure 6.4.1

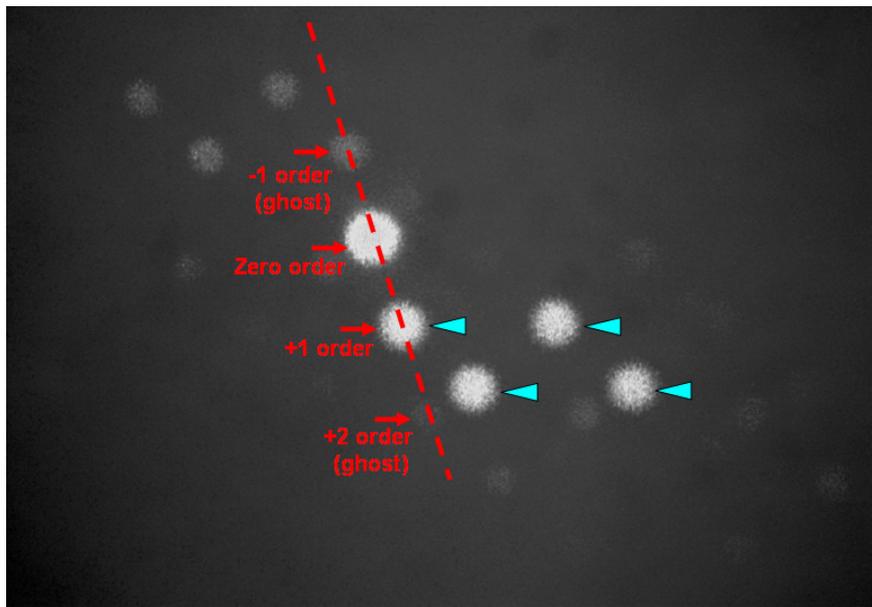


*Fig. 6.4.1: A digital camera photograph showing a diffractive pattern reconstructed on a paper screen: Only the four brighter spots marked by a blue triangle are the desired diffractive orders, all the other weaker spots appearing on the dark background are the ghosts. The red dashed line marks a series spots generated by a phase grating, where only the +1 order is desired.*

With the Lenses and Gratings (LG) algorithm, a CGH, which can generate a  $N \times M$  beam array, as shown in figure 6.4.2, is presented as:

$$\varphi_h = \sum_{i,j}^{n,m} \varphi_{i,j} \quad (6.4.1)$$

where,  $\varphi_{i,j}$  is a phase of prism which can deflect a +1 order beam to the desired position,  $(\rho_i, \rho_j)$ .

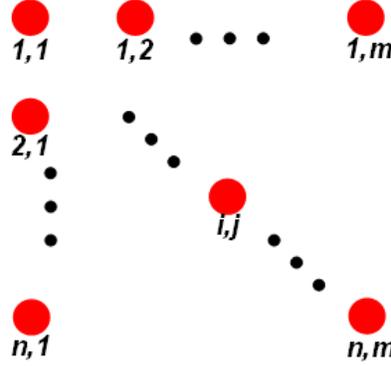


*Fig. 6.4.2:  $N \times M$  beams array.*

Without giving a sufficient extra freedom to avoid the degeneracy caused by the ghosts overlapping and interfering with the desired orders [118], the highly symmetric patterns can show a high degree of non-uniformity and poor diffraction efficiency, explaining the results in figures 6.3.1 and 6.3.2 when  $R < 10$  with the LG algorithm.

#### 6.4.2 Degeneracy avoided by adding a random phase

On applying a freedom of asymmetry,  $R$ , the position of each designed +1 order beams was no longer fixed, but randomly located within a circle area (centre:  $(\rho_i, \rho_j)$ ; Radius =  $R$ ), as shown in figure 6.2.2. In this way, a random phase,  $\varphi_{i,j(R)}$ , is added to the individual prism phase  $\varphi_{i,j}' = \varphi_{i,j} + \varphi_{i,j(R)}$ . The phase CGH for the pattern with  $R$  can then be represented as:

$$\varphi_h' = \sum_{i,j}^{n,m} \varphi_{i,j}' = \sum_{i,j}^{n,m} (\varphi_{i,j} + \varphi_{i,j(R)}) \quad (6.4.2)$$

$R$  is equivalent to adding an extra phase ( $\phi_{i,j}(R)$ ), which gave the extra freedom to improve the uniformity of the diffractive pattern by decreasing the possibility of degeneracy. The larger the value of  $R$ , the more freedom of phase was delivered to each of the desired +1 order beams, hence further avoiding the degeneracy, which explains the results shown in figure 6.3.1.

## 6.5 Summary

The results described in this chapter show that, to ensure a good uniformity of the diffracted pattern, a highly degree of symmetry in the pattern design should be avoided, although the time-consuming iterative GS algorithm may generate a symmetric diffractive pattern ( $R < 20 \mu\text{m}$ ) with a slightly better uniformity.

The simple and computationally fast non-iterative LG algorithm can generate asymmetric patterns with excellent uniformity and high diffractive efficiency ( $R > 20 \mu\text{m}$ ,  $V < 6\%$  and  $\eta > 50\%$ ); hence it can be an ideal algorithm of CGH calculation for diffractive multi-beam ultrafast laser processing.

## **Chapter 7**

# **Investigations into potential applications of diffractive multiple beam laser microprocessing**

## **7.1 Introduction**

Since the laser energy available from commercial laser sources exceeds the single beam laser ablation process requirements, parallel processing with multiple beams could provide an easy route for up-scaling processing speed and reduce manufacturing costs. The following sections describe methods studied for parallel processing of materials with high speed, dynamic control and great flexibility, for a number of material types and potential applications.

## **7.2 High throughput surface micro-structuring of silicon**

Surface micro-structuring of silicon has been reported to change the surface wetting properties and opens up a large range of applications, such as self-cleaning surfaces, microfluidics, lab-on-chip devices, low friction coatings, water proof and anti-rain textiles [132-135]. The wetting properties of materials can be modified by altering either the morphology or the chemistry of a surface [136-140]. Ultrashort pulse laser micro-structuring of silicon has demonstrated a unique advantage, that is producing a morphology which exhibits two length scales via a simple one step process, without the need of a clean room facility or high-vacuum equipment requirements [141, 142]. However, the low processing throughput might be a main issue preventing ultrashort pulse lasers from finding applications in surface micro-structuring for industry. With this limitation in mind, an SLM, Holoeye LC-R 2500, was employed here to generate multi-beam patterns for a high throughput surface micro-structuring of silicon using a Clark-MXR CPA2010 femtosecond laser.

### 7.2.1 Diffractive multi-beam pattern design

The multi-beam pattern for surface micro-structuring of silicon was a  $10 \times 4$  beam array, formed by four asymmetric parts to keep a good uniformity of the desired beams, as discussed in chapter 6. The pattern was scanned in six concentric circles. The diameter of each concentric circle was 300, 250, 200, 150, 100 and  $50\mu\text{m}$  and the gap between two neighbouring circles was  $25\mu\text{m}$  as shown in figure 7.2.1. The distance between two neighbouring diffractive beams ( $d$ ) was designed to be 300, 200 and  $150\mu\text{m}$ . There was no interference among the scanned circles when  $d = 300\mu\text{m}$ ; however, the circles partially and totally interfered when  $d = 200\mu\text{m}$  and  $d = 100\mu\text{m}$  respectively, as shown in figure 7.2.2.

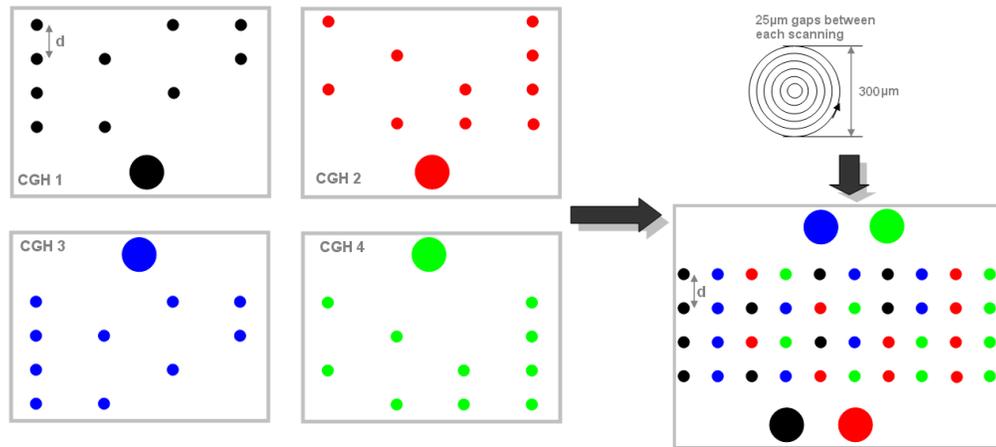


**Fig. 7.2.1:** Multi-beam pattern design for surface micro-structuring of silicon – generating a  $10 \times 4$  beam array.

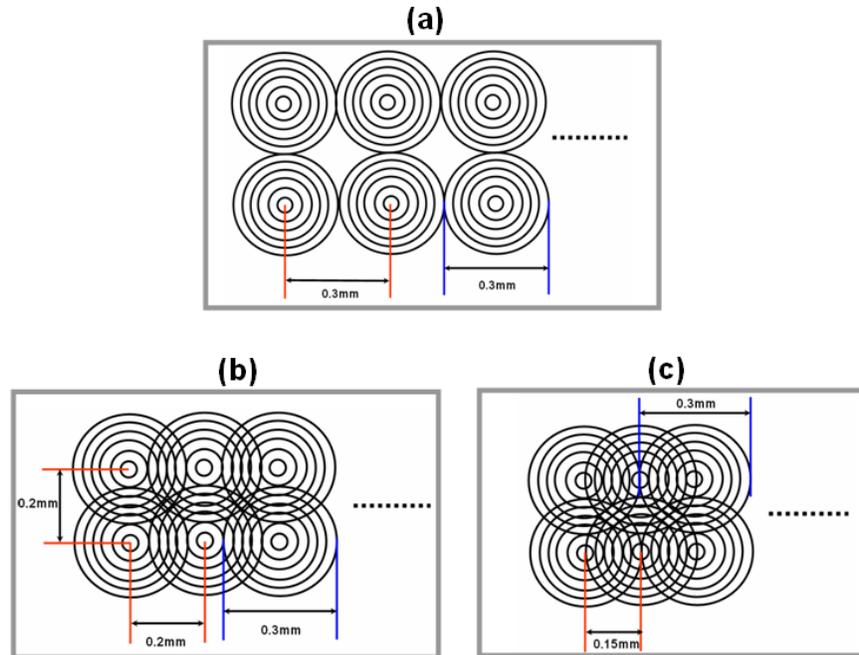


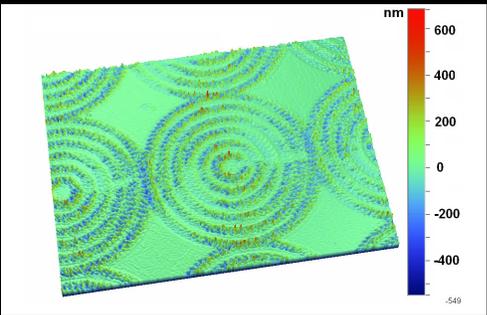
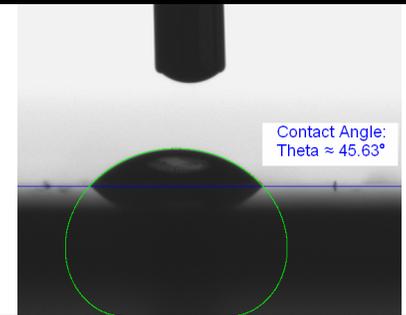
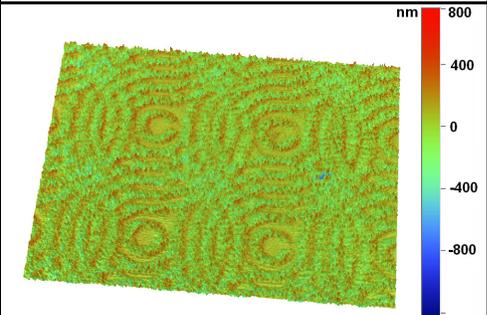
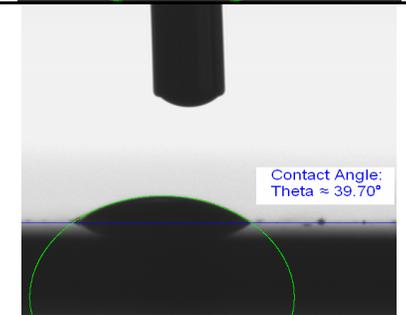
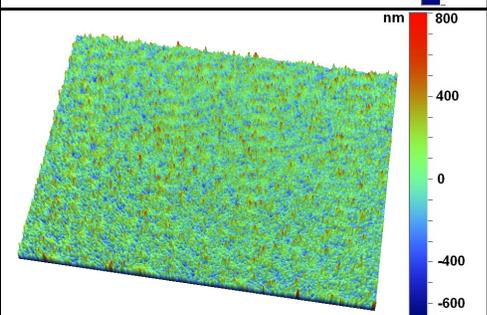
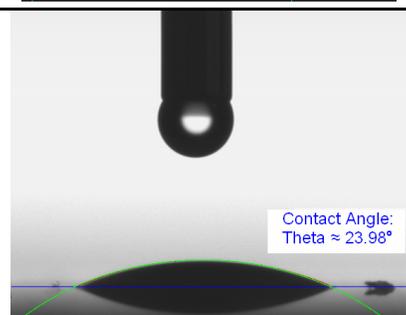
**Fig. 7.2.2:** Scanning patterns for six concentric circles. (a)  $d = 0.3\text{mm}$ ; no interference among the scanned circles, (b)  $d = 0.2\text{mm}$ ; partial interference among the scanned circles, (c)  $d = 0.15$ , total interference among the scanned circles.

### 7.2.2 Results of micro-structuring of silicon using the diffracted patterns

An ultrashort pulse laser beam ( $\tau_p \approx 180\text{fs}$ ) with pulse energy,  $E_p \approx 200\mu\text{J}$ , was applied to the SLM, and after diffraction each of the desired multiple beams with  $E_p \approx 10\mu\text{J}$  was scanned at a speed of  $20\text{mm/s}$  across the silicon sample surface. The machining speed was ten times faster than single beam processing. The results are compiled in table 7.1. The surface morphology was controlled by  $d$ , the distance between two neighbouring diffractive beams. When  $d$  was smaller, the more scanned circles that interfered generated a surface with greater roughness. The measured contact angle decreased by increasing the surface roughness and hence the silicon surface became more hydrophilic as a result of the structuring process.

The chemistry of the machined silicon surface was investigated by a Raman spectrometer. The results indicated that a part of the material was oxidised and probably formed a SiO<sub>2</sub> layer after processing. After removing the oxidised layer by immersing in a 10% HF solution, the contact angle of the silicon sample was measured again. The results demonstrated that the contact angle increased with the oxidised layer removed and the silicon surface became hydrophobic.

**Table 7.1:** The results of micro-structuring of silicon using the diffracted multi-beam patterns.

d (mm)	3D profile of the machined silicon surface (by Wyko NT1100 optical surface profiler)	Measured contact angle of water droplet*
0.3		
0.2		
0.15		

\* The water droplet contact angle of the original silicon surface was measured at 50.57°

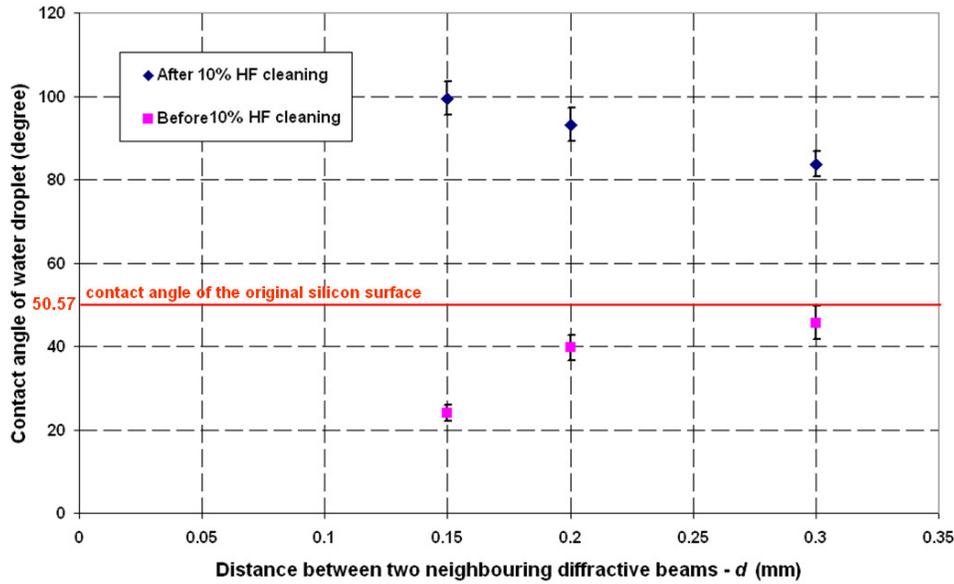


*Fig. 7.2.3: Change of the contact angle versus the surface morphology (controlled by  $d$ ) and chemistry (before and after the oxidised layer removed).*

Figure 7.2.3 shows the change of the contact angle against the surface morphology (controlled by  $d$ , the distance between two neighbouring diffractive beams) and the chemistry (before and after the oxidised layer was removed) of the silicon sample processed by the diffracted multi-beam patterns. The red line indicates the contact angle of the original silicon surface, measured as  $50.57^\circ$ .

### **7.3 Laser patterning of organic light emitting diode (OLED) materials**

Laser patterning of OLED materials is a key industrial process in the manufacturing of OLED displays or solid-state lighting foils [143]. Ultrashort pulse lasers are of particular interest for this application, as they enable selective ablative removal of OLED layers with very low energy density requirements on the target. Since the laser output from current commercial laser sources exceeds single beam ablative process

requirements, parallel processing with multiple beams could provide a novel route for up-scaling processing speed and reduce manufacturing costs. Hence SLMs could be employed for high throughput precision patterning of OLED materials (metal cathode and Indium Tin Oxide (ITO) anode) on flexible and glass substrates. The following describes an experimental study to explore this process application.

### 7.3.1 Diffractive multi-beam patterning of cathode layers

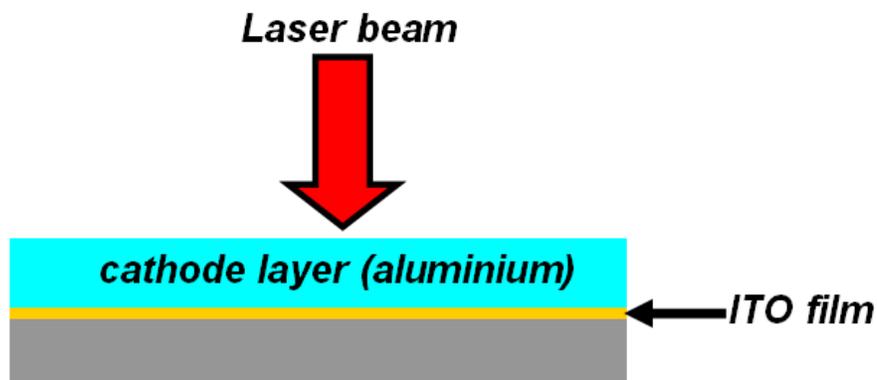


*Fig. 7.3.1: The layered structure of OLED material.*

As shown in figure 7.3.1, OLEDs are multi-layer materials, with each layer having its own ablation threshold, (for example, the top cathode layer, aluminium, has lower ablation threshold than the underlying anode layer, ITO film [144]). Hence, by controlling the laser fluence, selective removal of the aluminium can be achieved. Cross hatch patterning of an OLED using 15 parallel beams produced by a Hamamatsu X10468-04 SLM at 532 nm wavelength was applied, as shown in figure 7.3.2. A picosecond laser, High-Q IC-355-800ps, with 532nm wavelength was used. The laser pulse energy, the repetition rate and the scanning speed were 12  $\mu$ J, 5 kHz and 30 mm/s, respectively. Only a single scan was conducted, resulting in multiple scribe lines with a pitch of 86  $\mu$ m, a line width of  $\sim$ 10  $\mu$ m and a depth of  $\sim$  290 nm.

The depth profile of the scribe line shown in figure 7.3.2 (bottom), revealed a flat bottom channel in which the cathode and organic layers were removed, while the underlying anode (ITO film) remained unaffected.

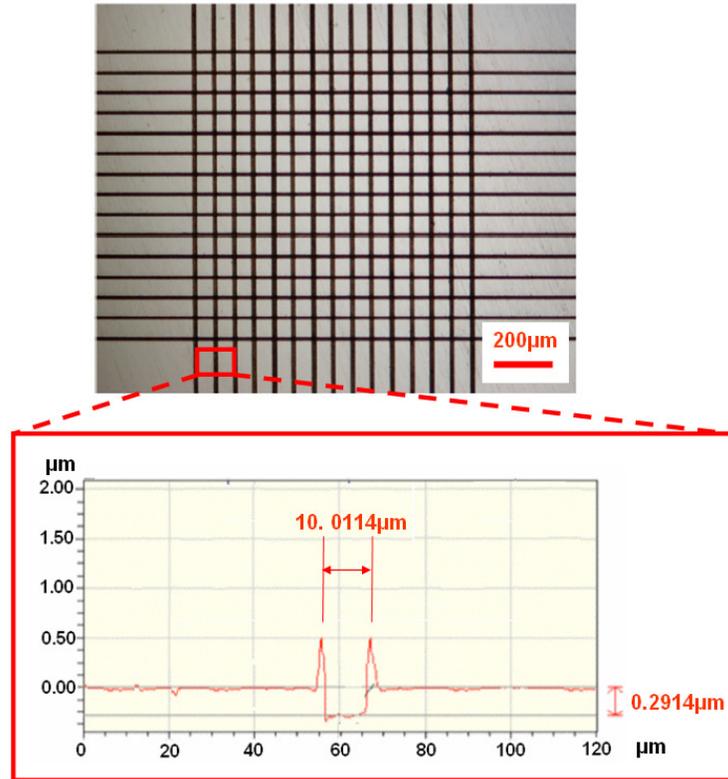


*Fig. 7.3.2: Parallel processing of OLED. Optical micrographs (Upper), cross-sectional profile of a single line (bottom).*

### 7.3.2 Diffractive multi-beam patterning of Anode (ITO)

Since the absorption of ITO material in the NIR region is stronger than that in the visible region, a picosecond laser, High-Q IC-355-800ps, with 1064nm wavelength was used for patterning of ITO on glass samples. Figure 7.3.3 demonstrates a microscopic image and surface profile of the ITO sample that was ablated using 15 beams generated by the Hamamatsu X10468-03 SLM with 1064 nm laser wavelength. The incident pulse energy on the sample was 16  $\mu$ J with 5 kHz repetition rate, and 15

mm/s scanning speed. Only a single scan was performed. The grating period,  $\Lambda$ , was 65  $\mu\text{m}$ . As illustrated, the scribing line had a depth of  $\sim 60$  nm and a width of 14  $\mu\text{m}$ , and showed a flat bottom area that indicated complete removal of the ITO film. Placing the spots closer and using lower laser pulse energies reduced the pitch and the scribing width, respectively. There was no significant thermal damage to the surrounding area observed.

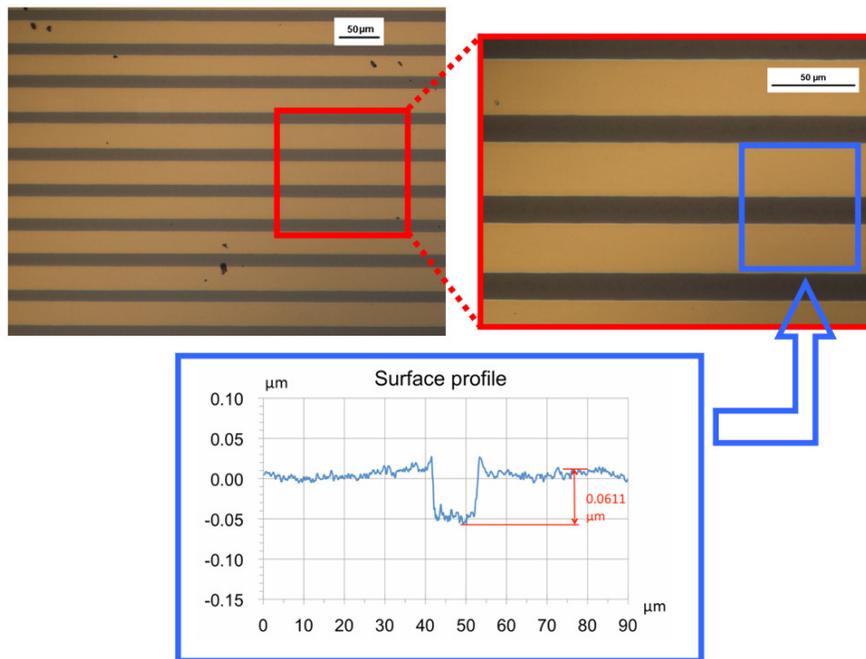


*Fig. 7.3.3: Parallel processing of ITO thin film sample using a diffractive multi-beam. Top: Optical micrographs; Bottom: Cross-sectional profile of a single scribe.*

## 7.4 Selective ablation of surface material (silicon wafer) by diffractive multi-beams

### 7.4.1 Selective ablation by modulating the focal height

As the focal position of each diffractive order beam can be three dimensionally modulated by a CGH calculated algorithm, a diffractive beam pattern, NWDA, with 39 multiple beams focused at two different planes was modulated. Here, a 3D

Gershberg-Saxton algorithm was adopted to calculate the CGH, as shown in figure 7.4.1 (a). The distance between the two focal planes was  $\Delta d \approx 0.5\text{mm}$ , as shown in figure 7.4.1(b). The machining result using ultrashort laser pulses ( $\tau_p \approx 10\text{ps}$ ,  $\lambda \approx 1064\text{nm}$ ) is demonstrated in figure 7.4.2, where 1000 pulses was input with total pulse energy,  $E_p \approx 220\mu\text{J}$ , measured before the SLM. The upper surface of the sample (a silicon wafer) was positioned on the focal plane of the beams composing ‘N’ and ‘D’, which fabricated holes  $\Phi_1 \approx 24 \pm 0.8\mu\text{m}$ . Clearly, the size of the holes composing ‘W’ and ‘A’, which were fabricated by the beams modulated slightly out of focus at the sample surface, was smaller ( $\Phi_2 \approx 15 \pm 0.5\mu\text{m}$ ) due to the decrease of Gaussian distributed hot spot on the sample surface where the fluence was higher than the well defined ablation threshold (see figure 7.4.3). Accordingly, the fluence of each diffractive +1 order could be adjusted by precisely modulating the focal height.

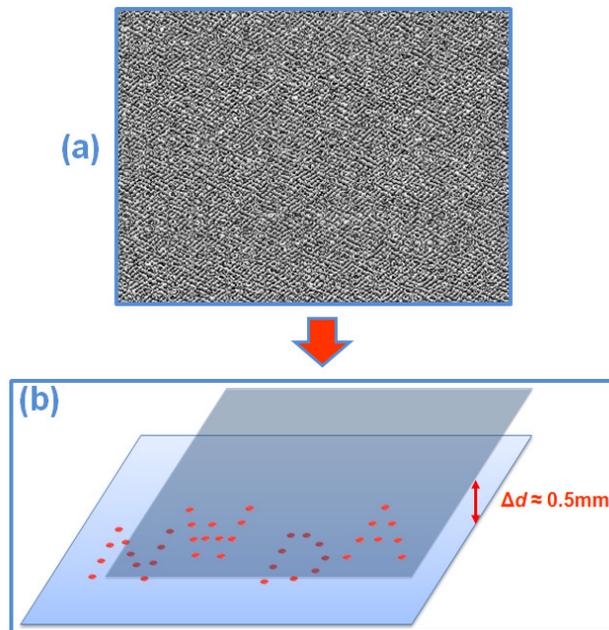


**Fig. 7.4.1:** (a) The CGH, calculated by 3D Gershberg-Saxton algorithm, which can create a ‘NWDA’ diffracted beam pattern with 39 multiple beams focused at two different planes. (b) Schematic showing the computationally reconstructed ‘NWDA’ pattern.

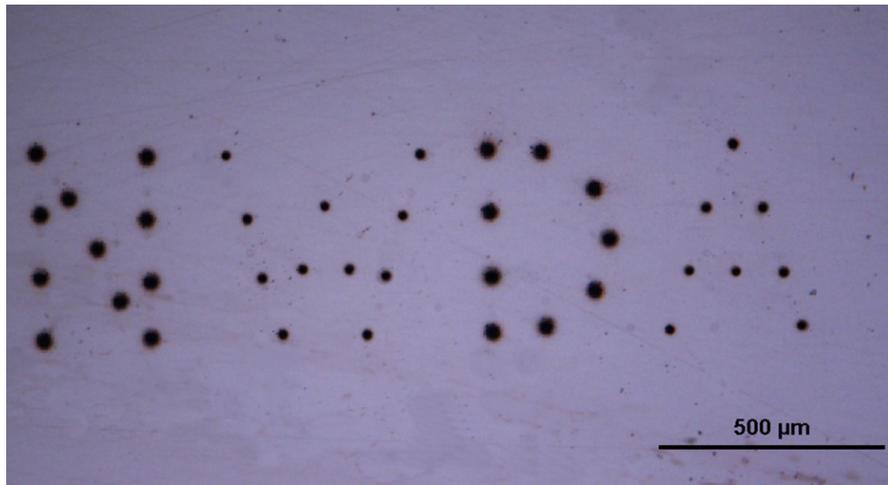


*Fig. 7.4.2: Processing result for the 'NWDA' pattern applied to a polished Ti6Al4V sample.*

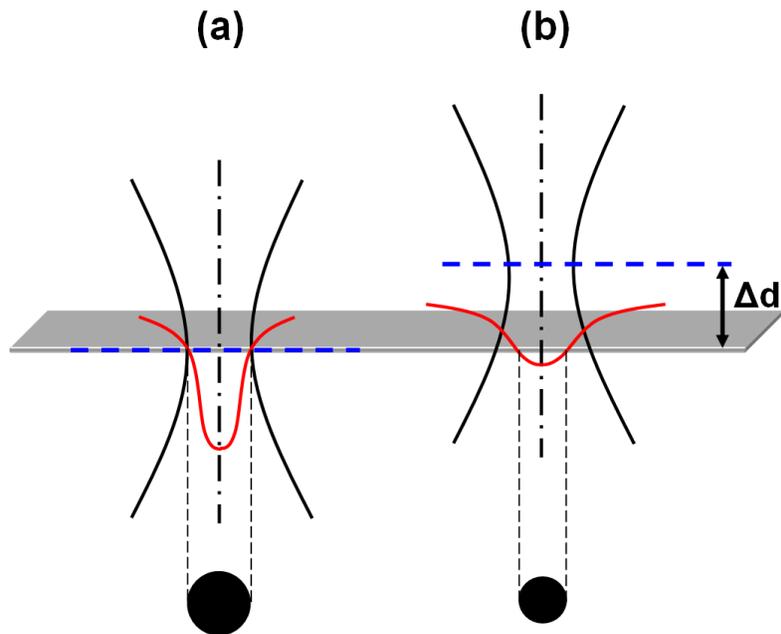


*Fig. 7.4.3: Schematic demonstrating the size of hole adjusted by precisely modulating the focal height difference of each diffractive order,  $\Delta d$ . (a) The diffractive beam is precisely focused on the sample surface hence fabricating a larger sized hole; (b) the*

*diffractive beam is slightly out of focus by a distance ( $\Delta d$ ), hence fabricating smaller sized hole.*

### 7.4.2 Multi-beam scanning with different number of spots per line

Beam scanning with a different number of spots per line mimics a variable spot overlap and can produce variable controlled ablation depth [91]. As shown in Figure 7.4.4 (a), 10 beams were arranged in a pyramid-shaped pattern (4-3-2-1) so as to achieve selective ablation with a single scan at different positions. The small red circles in Figure 7.4.4 (b) denote the 10-beam pattern used for silicon scribing. The total pulse energy incident on the sample was 18  $\mu\text{J}$ , giving  $\sim 1.8 \mu\text{J}$  per beam. With a wavelength of 532 nm, a repetition rate of 5 kHz and a scan speed of 1 mm/s, different ablation depths were obtained, and 4, 3, 2 and 1 beams produced scribe lines with depth of  $\sim 2.82$ , 1.81, 1.33 and 0.82  $\mu\text{m}$  respectively, as shown in Figure 7.4.4 (c).

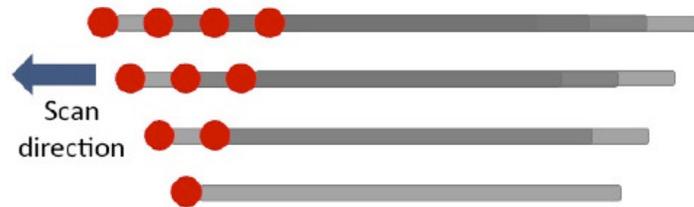


**Fig. 7.4.4 (a):** Schematic of selective ablation using different number of spots per line to produce different ablation depth. [91]

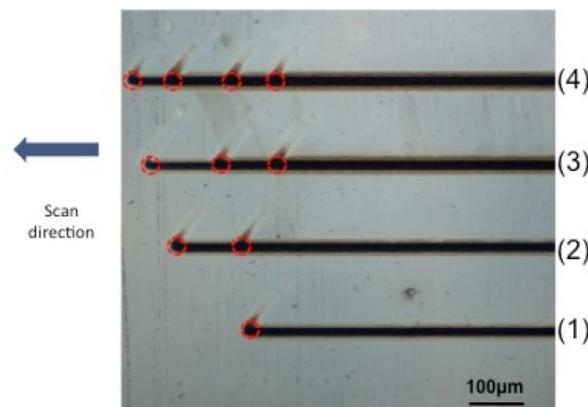


**Fig. 7.4.4 (b):** Micrograph of 10 beams selective ablation on silicon. The red circles represent the positions of the 10 beams. [91]

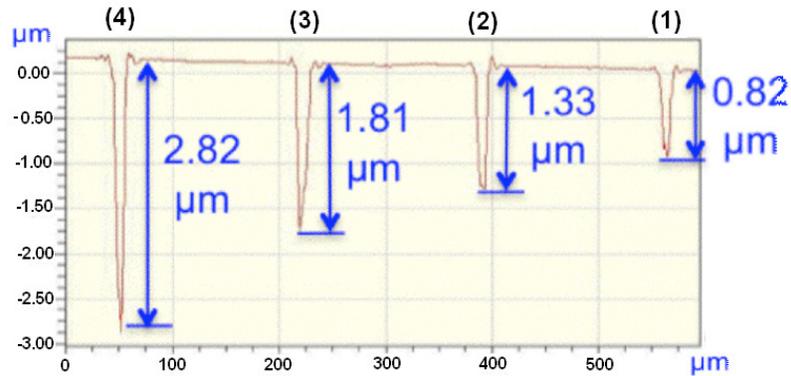


**Fig. 7.4.4 (c):** Cross-sectional surface profile of the 10 beams selective ablation on silicon. The scribe line 1, 2, 3 and 4 are consistent with those labelled in Fig. 7.2.4 (b). [91]

## 7.5 Diffractive multi-beam internal structuring of volume gratings

Using appropriate objectives, the laser beam can be precisely focused inside transparent materials, such as PMMA, with a tiny beam size,  $d < 10\mu\text{m}$ . The internal material properties can be modified to achieve a controllable refractive index change ( $\Delta n$ ), due to the highly focused laser energy, as a result of multi-photon absorption [145-147]. Accordingly, this method has been adopted to fabricate a wide range of internal optical components including waveguides, couplers, gratings and Fresnel lenses. The pulse energy,  $E_p$ , needed for  $\Delta n$  modulation is material-dependant and usually less than  $1\mu\text{J}$ . Applying greater energies would damage the material. Thus, the speed of internal material structuring is very slow with single beam processing. An unprecedented processing speed has been demonstrated for the fabrication of the internal volume gratings by applying parallel processing [149], where the desired diffracted beams were focused inside the material, as illustrated in figure 7.5.1.

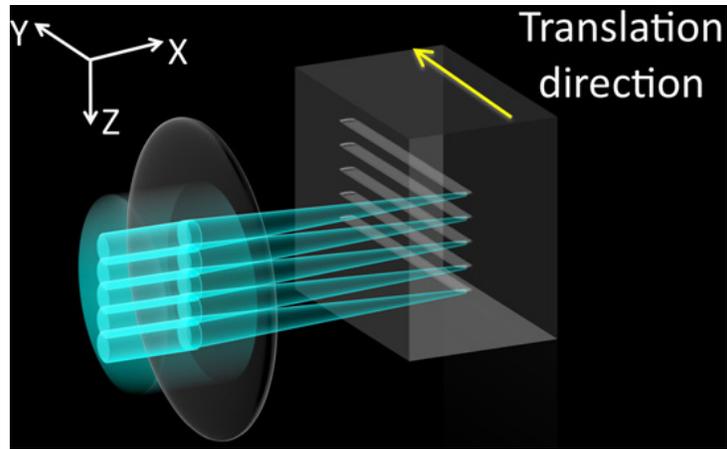


**Figure 7.5.1:** Schematic showing the internal volume grating fabrication by applying parallel processing of diffractive multi-beam.

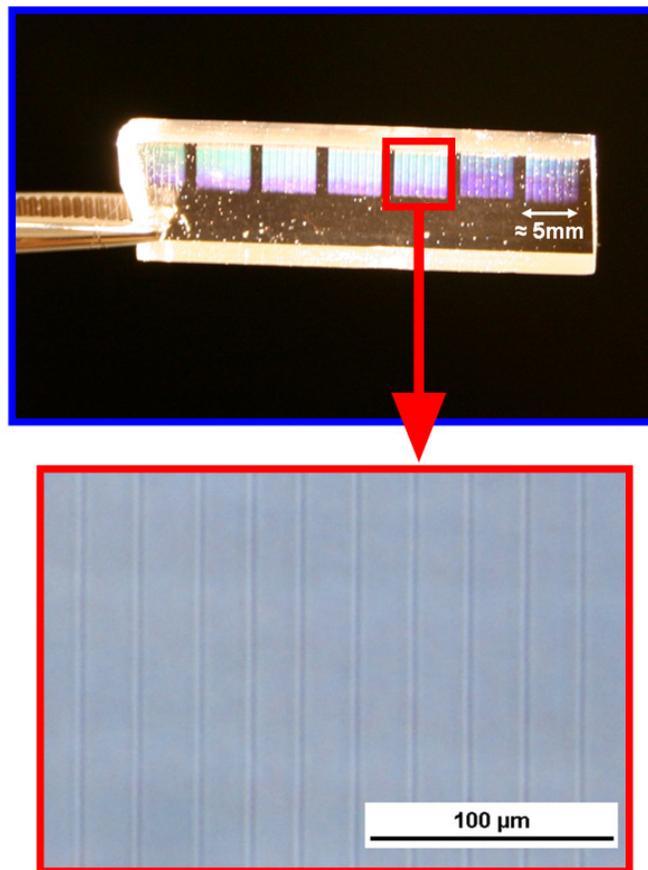


**Fig. 7.5.2:** Top: digital camera picture showing a series of volume gratings written inside a PMMA slab. Bottom: high magnification micrograph showing the fabricated grating with period,  $T \approx 19\mu\text{m}$ .

As shown figure 7.5.2, a series of 5 mm × 5 mm × 1mm volume gratings were written inside a PMMA sample using 160fs laser pulses at repetition rate  $f = 1\text{kHz}$  (Clark-MXR CPA2010). A diffracted pattern of 21 desired beams, as shown in figure 7.5.3, was used for the parallel processing to greatly increase the processing speed. Each of the gratings was completed within 10 minutes. The fabricated gratings had a measured diffraction efficiency  $\sim 68\%$  at the Bragg angle, giving a refractive index modification  $\Delta n \sim 1.64 \times 10^{-4}$  according to Kogelnik's coupled wave theory [148].

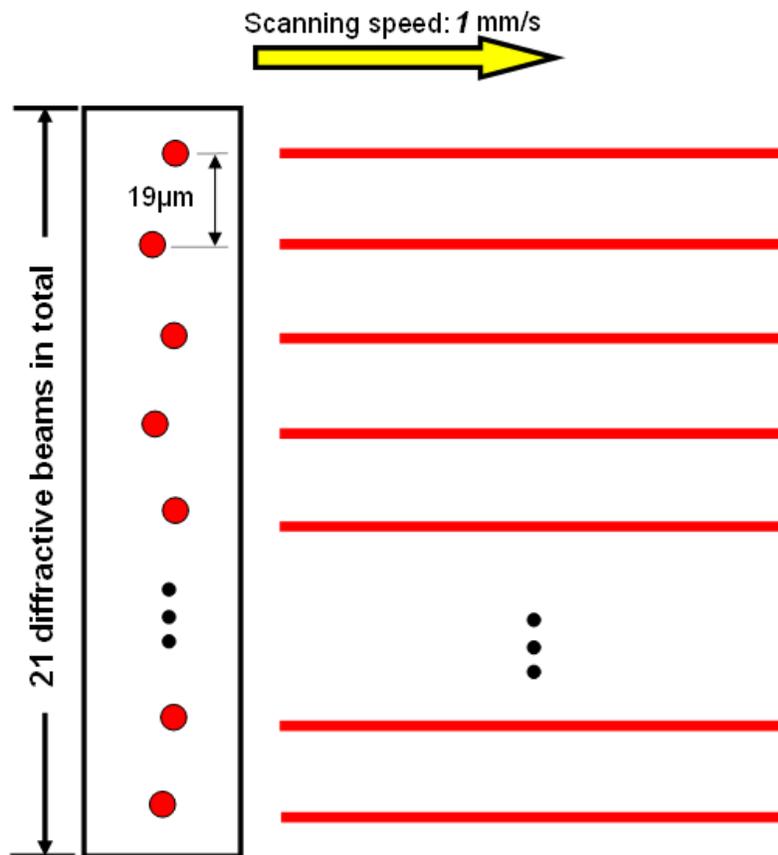


*Figure 7.5.3: Schematic showing the diffracted pattern of 21 desired beams, as applied to fabricate a volume grating at a scanning at a speed of 1mm/s.*

The gain in writing speed had an effect of multiplying the effective laser repetition rate by a gain factor,  $G > 20$ , equivalent to the single beam processing with  $f > 20\text{kHz}$ , but without the drawbacks of higher frequencies such as increased thermal accumulation effects and the necessity of increased scan speeds of the substrate, which would ultimately hit inertial limits of the motion control stages.

## **7.5 Summary**

In this chapter, ultrashort pulse laser parallel processing using diffracted multiple beams has demonstrated several potential applications. Firstly, high throughput surface micro-structuring of a silicon sample has been accomplished. The wetting properties of the silicon surface were controllably changed by the diffractive multi-beam processing with a throughput gain factor,  $G = 10$ , comparing to the single beam processing. Secondly, materials with a multi-layer structure (OLED) were structured on a specific top layer, while leaving the substrate layer unaffected. Thirdly, the selective ablation of surface material was demonstrated on a silicon sample by both adjusting the focal height of each of the beams and controlling the number of spots traversing each scanning line. Finally, diffractive multi-beam internal structuring results demonstrated that a significant gain in writing speed could be achieved.

## **Chapter 8**

# **Conclusions and recommendation for future work**

## 8.1 Conclusions

The conclusions drawn from each of the investigations described in this thesis are given in the following sections. These highlight the key findings and original aspects of the research undertaken.

### 8.1.1 Flexible high throughput short pulse laser processing

The results obtained demonstrated that precision diffractive multi-beam ultrashort pulse laser micro-structuring using a Spatial Light Modulator (SLM) is a novel method to increase processing throughput. Millijoule ( $10^{-3}\text{J}$ ) level output from the ultrashort pulse laser systems has been successfully diffracted into  $> 30$  arbitrary multiple spots with reasonably good uniformity. The diffractive multi-beam patterns are generated by Computer Generate Holograms (CGHs) calculated by appropriate algorithms and displayed on the SLM. By applying CGHs in real time while synchronising the scanning galvanometer, the results have demonstrated additional flexibility for surface micro-structuring, e.g. the multiple micro-channels fabricated on a silicon wafer and a true 3D chessboard type structure micro-machined on a polished Ti6Al4V sample. This work has been published in peer reviewed journals [88, 89].

### 8.1.2 Methods to remove the zero order beam

The zero order beam, always containing approximately 50% of the original energy input, should be removed before processing using the multi-beam patterns to avoid any unwanted damage to the sample. This undesired damage by the zero order beam can be avoided by either installing a 4f-imaging optical system to block the zero order at the Fourier plane, or adding a Fresnel zone lens on the CGH to defocus the zero

order at the processing plane (3.3, Chapter 3), as first reported by the current author and published in a peer reviewed journal [90].

### **8.1.3 The elongation of hole shape caused by chromatic distortion**

The finite laser bandwidth is shown to significantly alter the intensity distribution of the diffracted beam at higher angles resulting in elongated hole shapes and confirmed by a simple calculation using the grating equation (4.2.2, Chapter 4). This limitation can be neglected by using picosecond temporal pulselength with narrow spectral bandwidth, where the machined holes are almost perfectly round, independent of angle of diffraction and hence showing the advantage of parallel processing (5.3 Chapter 5). This work has been published in a peer reviewed journal [89].

### **8.1.4 Improving the uniformity of the diffracted multi-beam pattern**

The uniformity of the diffracted beam pattern is not only affected by the methods of CGH calculation, but also the geometric design of the diffractive pattern. A slight spatial disordering of periodic and symmetric patterns was found to significantly reduce intensity variations between each of the desired diffracted peaks.

The results in chapter 6 showed that, to ensure a good uniformity of the diffracted beam pattern, a high degree of symmetry geometric design should be avoided, although the time-consuming iterative Gerchberg-Saxton (GS) algorithm may generate a symmetric diffractive pattern ( $R < 20\mu\text{m}$ ) with a slightly better uniformity.

It was shown that the simple and computationally fast Lenses and Gratings (LG) non-iterative algorithms, could generate asymmetric patterns with excellent uniformity and

high diffraction efficiency ( $R > 20\mu\text{m}$ ,  $V < 6\%$  and  $\eta > 50\%$ ) and so could be an ideal algorithm of CGH calculation for diffractive multi-beam ultrashort pulse laser processing. This work is going to be published in conference or journal.

## **8.2 Recommendation for future work**

The following recommendations for further research have arisen from the work in this thesis:

### **8.2.1 High power laser beam tests on SLMs**

High power tests should be carried out to explore the maximum power handling of the SLMs, hence knowing the viable energy diffracted to the desired multiple beams, which is a significant step of transferring the laboratory work to industrial applications.

### **8.2.2 Further study of the multi-beam uniformity affected by the geometric pattern design**

As demonstrated in 6.3.2, uniform periodic arrays of diffractive spots can be generated by suitable sets of partial patterns with an asymmetric geometry design. Further study should be focused on the development of mathematical models which can be used to predict the optimum design of partial patterns.

### **8.2.3 Selective ablation of materials in multi-layer structures**

Laser patterning of Organic Light Emitting Diodes (OLEDs) is a key industrial process in the manufacturing of OLED displays or solid-state lighting foil. Ultrashort pulse lasers are of particular interest for this application as they enable selective ablative removal of OLED layers with very low energy density requirements on target.

Since sufficient laser output from commercial laser sources is currently exceeding single beam process requirements, parallel processing with multiple beams could provide a novel route for up-scaling processing speed and reduce manufacturing costs.

In the thesis, the removal of single layer, metal cathode and ITO anode, and selective ablation on a silicon wafer using the diffractive multi-beam patterns have been demonstrated (7.2 and 7.3, Chapter 7). In the future, selective ablation of the material with a multi-layer structure, e.g. OLED, should be attempted. The layers are coatings of different materials, e.g. organic semiconductor, metals and ITO, on a substrate, maybe glass, and hence have different ablation thresholds for the ultrashort pulses. Accordingly, selectively ablating the layers using a diffractive multi-beam pattern with precisely controlled pulse energy in each spot is possible, as shown in figure 8.2.1.

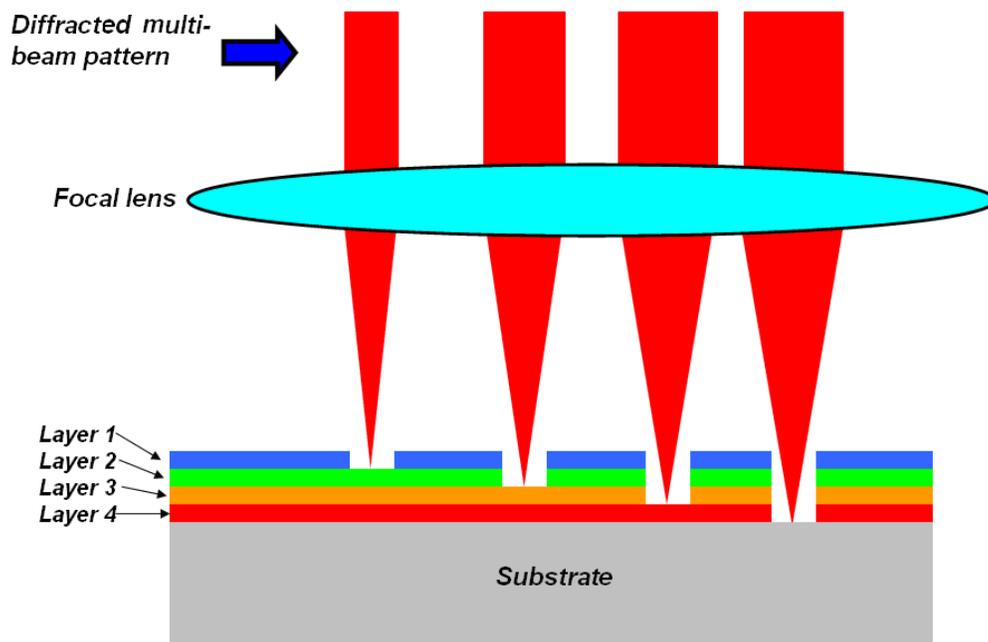


**Fig. 8.2.1:** Selective ablation of multi-layer structured material using a diffractive multi-beam pattern.

#### **8.2.4 Diffractive multi-beam internal structuring of transparent material**

Using suitable objectives, the ultrashort pulse laser beams could be precisely focused inside transparent materials, e.g. PMMA, with beam ‘spot’ size,  $d < 10\mu\text{m}$ . The internal material could thus be modulated to have a controllable refractive index change,  $\Delta n$ , by these highly focused intense beams due to the multi-photon absorption. Accordingly, this method could be adopted to fabricate a wide range of internal optical components including waveguides, couplers, gratings and Fresnel lenses. The pulse energy,  $E_p$ , required for  $\Delta n$  modulation is material-dependant and usually less than  $1\mu\text{J}$ . Applying  $E_p$  over that required will damage the material. Thus, the speed of the internal material structuring is very slow with single beam processing.

Studies carried out with co-workers in the Liverpool research group have shown that an unprecedented process speed could be demonstrated to modulate the internal material and a series of volume gratings has been successfully fabricated inside PMMA. In the future, more materials, such as fused silica, could be attempted for the diffractive multi-beam internal structuring with dynamic CGH control to make the processing more flexible.

## References

- [1] D. Du, X. Liu, G. Korn, J. Squier and G. Mourou, *Laser-induced breakdown by impact ionization in SiO<sub>2</sub> with pulse widths from 7 ns to 150 fs*, Applied Physic Letter, **64** (1994), p. 3071–3073.
- [2] X. Liu, D. Du and G. Mourou, *Laser ablation and micromachining with ultrashort laser pulses*, IEEE Journal of Quantum Electronics, **33**, 1997, p. 1706–1716.
- [3] C. Rullière, *Femtosecond laser pulses: principles and experiments*, Chapter three, Second Edition, Springer, 2003, p. 60-65.
- [4] A. E. Siegman, *Lasers*, Mill Valley, CA: University Science, 1986.
- [5] D. E. Spence, P. N. Kean, and W. Sibbet, *60-fsec pulse generation from a self-mode-locked Ti:Sapphire laser*, Optics Letters, **16**, 1991, p. 42–44.
- [6] E. P. Ippen, H. A. Haus, and L. Y. Liu, *Additive pulse modelocking*, Journal of the Optical Society of America B, **6**, 1989, p. 1736–1745.
- [7] U. Keller, D. A. B. Miller, G. D. Boyd, T. H. Chiu, J. F. Ferguson, and M. T. Asom, *Solid-state low-loss intracavity saturable absorber for Nd:YLF lasers: An antiresonant semiconductor Fabry–Perot saturable absorber*, Optics Letters, **17**, 1992, p. 505–507.
- [8] D. Kopf, F. X. Kartner, U. Keller, and K. J. Weingarten, *Diode-pumped mode-locked Nd:glass lasers with an antiresonant Fabry–Perot saturable absorber*, Optics Letters, **20**, 1995 p. 1169–1171.
- [9] R. L. Fork, O. E. Martinez, and J. P. Gordon, *Negative dispersion using pairs of prisms*, Optics Letters, **9**, 1984, p. 150–152.
- [10] O. E. Martinez, J. P. Gordon, and R. L. Fork, *Negative group-velocity*

- dispersion using refraction*, Journal of the Optical Society of America A, **1**, 1984, p. 1003–1006.
- [11] Ch. Spielmann, M. Lenzner, F. Krausz, R. Szipocs, and K. Ferencz, *Chirped dielectric mirrors improve Ti:sapphire lasers*, Laser Focus World, 31, Dec. 1995.
- [12] Ch. Spielmann, A. Stingl, F. Krausz, and R. Szipocs, *Chirped multilayer mirrors for dispersion control of femtosecond pulses*, in Proceeding of Conference. Lasers and Electro-Optics Europe—Tech. Dig. 1994, p. 30.
- [13] D. Strickland and G. Mourou, *Compression of amplified chirped optical pulses*, Optics Communications, **56**, 1985, pp. 219–221.
- [14] E. B. Treacy, *Optical pulse compression with diffraction gratings*, IEEE Journal of Quantum Electronics, 1969, **QE-5**, p. 454–458.
- [15] O. E. Martinez, *Design of high-power ultrashort pulse amplifiers by expansion and recompression*, IEEE Journal of Quantum Electronics, **QE-23**, 1987, p. 1385–1387.
- [16] M. Perry, *Multilayer dielectric gratings: Increasing the power of light*, Sci. & Tech. Review, Sept. 1995, p. 24-32.
- [17] D.E. Spence, P.N. Kean, W. Sibbett, *60-femtosecond pulse generation from a self-mode-locked Ti-sapphire laser*, Optics Letters. **16**, 1991, p.42-44.
- [18] J. Squier, F. Salin, G. Mourou, D. Harter, *100 femtosecond pulse generation and amplification in Ti-sapphire*, Optics Letters. **16**, 1991, p.324-326
- [19] U. Keller, G.W. 'tHooft, W.H. Knox, J.E. Cunningham, *Femtosecond pulses from a continuously self-starting mode- locked Ti:sapphire laser* Optics Letters, **16**, 1991, 1022-1024
- [20] H.A. Haus, J.G. Fujimoto, E.P. Ippen, *Analytic theory of additive pulse and*

- Kerr lens mode locking*, IEEE Journal of Quantum Electronics, **QE-28**, 1992, p. 2086-2096.
- [21] T. Brabec, C. Spielmann, P.F. Curley, F. Krausz, *Kerr lens mode locking*, Optics Letters, **17**, 1992, p. 1292
- [22] D. Strickland, G. Mourou, *Compression of amplified chirped optical pulses*, Optics Communications, **56**, 1985, p. 219-221.
- [23] P. Maine, D. Strickland, P. Bado, M. Pessot, G. Mourou, *Generation of Ultrahigh. Peak Power Pulses by Chirped Pulse Amplification*, IEEE Journal of Quantum Electronics. **QE-24**, 1988, p. 398-408.
- [24] G. Vaillancourt, T.B. Norris, J.S. Coe, P. Bado, G.A. Mourou, *Operation of a 1-kHz pulse-pumped Ti:sapphire regenerative amplifier*, Optics Letters, **15**, 1990, p. 317-319.
- [25] A. Sullivan, H. Hamster, H.C. Kapteyn, S. Gordon, W. White, H. Nathel, R.J. Blair, R.W. Falcone, *Multiterawatt, 100-fs laser*, Optics Letters. **16**, 1991, p. 1406-1408.
- [26] F. Dausinger, H. Hügel, V. Konov, *Micro-machining with Ultra-short Laser Pulses, from Basic Understanding to Technical Application*. In: International Conference of Advanced Laser Technologies 2002, Adelboden, Switzerland, 15–20 September 2002, ALT-02
- [27] F. Dausinger, *Machining of Metals with Ultrashort Laser Pulses: Fundamental Aspects and Their Consequences*, International Conference of Lasers and Electrooptics/Europe 2003, Munich, Germany, 22–27 June 2003, CK5-1-FRI.
- [28] J.E. Murray, W.H. Lowdermilk, *Nd:YAG regenerative amplifier*, Journal of Applied Physics. **51**, 1980, p. 3548-3555

- [29] L. H. Lin, B. Ouyang, S. Y. Li, W. Ge, Y. Y. Kang and S. S. Chen, *A compact subnanosecond high power Nd:YAG laser system*, *Optical and Quantum Electronics*, **23**, 1991, p. 433-438.
- [30] A.J. Ruggiero, N.F. Scherer, G.M. Mitchell, G.R. Fleming, J.N. Hogan, *Regenerative amplification of picosecond pulses in Nd:YAG at repetition rates in the 100-kHz range*, *Journal of the Optical Society of America B*, **8**, 1991, p. 2061-2067.
- [31] D.R. Walker, C.J. Flood, H.M. van Driel, U.J. Greiner, H.H. Klingenberg, *High power diode-pumped Nd:YAG regenerative amplifier for picosecond pulses*, *Applied Physics Letters*, **65**, 1994, p.1992-1994
- [32] M.J.P. Dymott, K.J.Weingarten, *Picosecond diode-pumped laser system with 9.3-W average power and 2.3-mJ pulse energy*, *Applied Optics*, **40**, 2001, p. 3042-3045.
- [33] J. Kleinbauer, R. Knappe, R. Wallenstein, *A powerful diode-pumper laser source for micro-machining with ps pulses in the infrared, the visible and the ultraviolet*, *Applied physic B*, **80**, 2005, p. 315-320.
- [34] Nd:VAN regenerative laser amplifier, *Manual of High-Q IC-355-800ps Photonics Solutions Laser*, 2007
- [35] Fianium ultrafast fiber lasers, Official webpage of Fianium laser [cited Oct. 2009; Available at: <http://www.fianium.com/>]
- [36] Claude Phipps, *Laser Ablation and its Applications*, 2007 Springer Science + Business Media LLC.
- [37] B. N. Chichkov, C. Momma, S. Nolte, F. von Alvensleben and A. Tunnermann, *Femtosecond, picosecond and nanosecond laser ablation of solids*, *Applied. Physic A*, **63**, 1996, p. 109–115.

- [38] Martin E. Fermann, Almantas Galvanauskas, and Gregg Sucha, *Ultrafast lasers technology and applications*, Marcel Dekker, Inc. 2001
- [39] P. Pronko, S. Dutta, J. Squier, J. Rudd, D. Du, and G. Mourou, *Machining of sub-micron holes using a femtosecond laser at 800 nm*, Optics Communications. **114**, 1996, pp. 106–110.
- [40] J. R. Bettis, R. A. House, II, and A. H. Guenther, *Spot size and pulse duration dependence of laser-induced damage*, in Laser Induced Damage in Optical Materials: 1976, NBS Spec. Pub., **462**, 1976, p. 338–345.
- [41] P. Babo, W. Clark, A. Said, *Ultrafast laser micromachining hand book*, Clark-MXR. Inc. Official Webpage [cited Oct. 2009; Available from: <http://www.cmxr.com/industrial/handbook/introduction.htm>]
- [42] F. Dausinger, *Machining of metals with ultrashort laser pulses: from fundamental investigations to industrial applications*, Proceeding of SPIE **5777**, 2005, p. 840 – 845.
- [43] G. Račiukaitis, M. Brikas, *Micro-machining of silicon and glass with picosecond lasers*, Proceeding of SPIE **5662**, 2004, p. 717 – 721.
- [44] A. Ostendorf, G. Kamlage, U. Klug, F. Korte, B.N. Chichkov, *Femtosecond versus picosecond laser ablation (Keynote Address)*, Proceeding of SPIE **5713**, 2005, p. 1-8
- [45] D. Karnakis, G. Rutterford, M. Knowles, T. Dobrev, P. Petkov, S. Dimov, *High quality laser milling of ceramics, dielectrics and metals using nanosecond and picosecond lasers*, Proceeding of SPIE **6106**, 2006, p. 610604
- [46] J. Cheng, W. Perrie, M. Sharpe, S.P. Edwardson, N.G. Semaltianos, G. Dearden and K.G. Watkins, *Single-pulse drilling study on Au, Al and Ti*

- alloy by using a picosecond laser*, Applied Physics A **95**, 2009, p. 739–746.
- [47] J. Cheng, W. Perrie, B. Wu, S. Tao, S.P. Edwardson, G. Dearden and K.G. Watkins, *Ablation mechanism study on metallic materials with a 10ps laser under high fluence*, Applied Surface Science, **255**, 2009, p. 8171-8175.
- [48] S. Nolte, C. Momma, H. Jacobs, A. Tunnermann, B.N. Chichkov, B. Wellegehausen, H. Welling, *Ablation of metals by ultrashort laser pulses*, Journal of the Optical Society of America B, **14**, 1997, p. 2716-2722.
- [49] B. Le Drogoff, F. Vidal, Y. Von Kaenel, M. Chaker, T.W. Johnston, S. Laville, *Ablation of aluminum thin films by ultrashort laser pulses*, Journal of Applied Physics, **89**, 2001, p. 8247-8252.
- [50] P. Mannion, J. Magee, E. Coyne and G.M. O'Connor, *Ablation thresholds in ultrafast laser micro-machining of common metals in air*, Proceedings of SPIE, **4876**, 2003, p. 470-478.
- [51] R.Le. Harzic, D. Breitlung, M. Weikert, S. Sommer, C. Fohl, S. Valette, C. Donnet, E. Audouard and F. Dausinger, *Pulse width and energy influence on laser micromachining of metals in a range of 100 fs to 5 ps*, Applied Surface Science, **249**, 2005, p. 322–331.
- [52] W. Perrie, M. Gill, G. Robinson, P. Fox and W. O'Neill, *Femtosecond laser micro-structuring of aluminium under helium*, Applied Surface Science, **230**, 2004, p. 50–59.
- [53] A. Luft, U. Franz, A. Emsemann and J. Kasper, *A study of thermal and mechanical effects on materials induced by pulsed laser drilling*, Applied Physics A, **63**, 1996, pp. 93–101.
- [54] K. Kawamura, T. Ogawa, N. Sarukura, M. Hirao, and H. Hosono, *Fabrication of surface relief gratings on transparent dielectric materials by*

- two-beam holographic method using infrared femtosecond laser pulses*, Applied Physics B, **71**, 2000, p. 119-121.
- [55] T. Kondo, S. Matsuo, S. Juodkazis, and H. Misawa, *A novel femtosecond laser interference technique with diffractive beam splitter for fabrication of three-dimensional photonic crystals*, Applied Physics Letters. **79**, 2001, p. 725-727.
- [56] T. Kondo, S. Matsuo, S. Juodkazis, V. Mizeikis, and H. Misawa, *Multiphoton fabrication of periodic structures by multibeam interference of femtosecond pulses*, Applied Physics Letters, **82**, 2003, p. 2758-2760.
- [57] S. Yang, M. Megens, J. Aizenberg, P. Wiltzius, P. M. Chaikin, and W. B. Russel, *Creating periodic three-dimensional structures by multibeam interference of visible laser*, Chemistry of Materials, **14**, 2002, p. 2831-2833.
- [58] Hiroaki Misawa, Toshiaki Kondo, Saulius Juodkazis, Vygantas Mizeikis, and Shigeki Matsuo, *Holographic lithography of periodic two- and three-dimensional microstructures in photoresist SU-8*, Optics Express, **14**, 2006, p. 7943-7953.
- [59] Satoru Shoji, Remo Zaccaria, Hong-Bo Sun, and Satoshi Kawata, *Multi-step multi-beam laser interference patterning of three-dimensional photonic lattices*, Optics Express, **14**, pp. 2309-2316.
- [60] S. Shoji and S. Kawata, *Photofabrication of three-dimensional photonic crystals by multibeam laser interference into a photopolymerizable resin*, Applied Physics Letters. **76**, 2000, p. 2668-2670.
- [61] S. Shoji, H.-B. Sun, and S. Kawata, *Photofabrication of wood-pile three-dimensional photonic crystals using four-beam laser interference*, Applied

- Physics Letters, **83**, 2003, p. 608-610.
- [62] M. Campbell, D. N. Sharp, M. T. Harrison, R. G. Denning, and A. Turberfield, *Fabrication of photonic crystals for the visible spectrum by holographic lithography*, Nature, **404**, 2000, p. 53 - 56.
- [63] Y. Li, W. Watanabe, K. Yamada, T. Shinagawa, K. Itoh, J. Nishii, and Y. Jiang, *Holographic fabrication of multiple layers of grating inside soda-lime glass with femtosecond laser pulses*, Applied Physics Letters, **80**, 2002, p. 1508-1510.
- [64] K. Venkatakrishnan, N. R. Sivakumar, C. W. Hee, B. Tan, W. L. Liang, and G. K. Gan, *Direct fabrication of surface-relief grating by interferometric technique using femtosecond laser*, Applied Physics A, **77**, 2003. p. 959-963.
- [65] Yoshiki Nakata, Tatsuo Okada and Mitsuo Maeda, *Nano-Sized Hollow Bump Array Generated by Single Femtosecond Laser Pulse*, Japanese Journal of Applied Physics, **42**, 2003, p. L1452-L1454.
- [66] Y. Nakata, T. Okada and M. Maeda, *Fabrication of dot matrix, comb, and nanowire structures using laser ablation by interfered femtosecond laser beams*, Applied Physics Letters, **81**, 2002, p. 4239-4241.
- [67] Y. Nakata, T. Okada and M. Maeda, *Formation of Periodic Structure Inside Silica Glass and Acryl by Interfering Femtosecond Laser*, Japanese Journal of Applied Physics, **42**, 2003, p. L379-L380.
- [68] Y. Nakata, T. Okada and M. Maeda, *Lines of periodic hole structures produced by laser ablation using interfering femtosecond lasers split by a transmission grating*, Applied Physics A, **77**, 2003, p. 399-401.
- [69] S. M. Kirkpatrick, J. W. Baur, C. M. Clark, L. R. Denny, D. W. Tomlin, B.

- R. Reinhardt, R. Kannan, and M. O. Stone, *Holographic recording using two-photon-induced photopolymerization*, Applied Physics A, **69**, 1999, p. 461 – 464.
- [70] L. L. Brott, R. R. Naik, D. J. Pikas, S. M. Kirkpatrick, D. W. Tomlin, P. W. Whitlock, S. J. Clarson, and M. O. Stone, *Ultrafast holographic nanopatterning of biocatalytically formed silica*, Nature (London) **413**, 2001, p. 291 – 293.
- [71] K. Kawamura, M. Hirano, T. Kamiya, and H. Hosono, *Holographic writing of volume-type microgratings in silica glass by a single chirped laser pulse*, Applied Physics Letter **81**, 2002, 1137 – 1139.
- [72] S. Matsuo, T. Kondo, S. Juodkazis, V. Mizeikis, and H. Misawa, *Fabrication of three-dimensional photonic crystals by femtosecond laser interference*, Proceeding of SPIE **4655**, 2002, p. 327 – 334.
- [73] Shigeki Matsuo, Takashi Miyamoto, Takuro Tomita, and Shuichi Hashimoto, *Applications of a microlens array and a photomask to the laser microfabrication of a periodic photopolymer rod array*, Applied Optics, **46**, 2007, pp. 8264-8267.
- [74] M. Oikawa and K. Iga, *Distributed-index planar microiensi*, Applied Optics, **21**, 1982, p. 1052-1056.
- [75] S. Matsuo, S. Juodkazis, and H. Misawa, *Femtosecond laser microfabrication of periodic structures using a microlens array*, Applied Physics A, **80**, 2005, p. 683-685.
- [76] J. Kato, N. Takeyasu, Y. Adachi, H.-B. Sun, and S. Kawata, *Multiple-spot parallel processing for laser micronanofabrication*, Applied Physics Letters, **86**, 2005, p. 044102-044104.

- [77] Multi-beam optical system using lens array, US Patent 4428647.
- [78] C.H. Sow, A.A. Bettioli, Y.Y.G. Lee, F.C. Cheong, C.T. Lim and F. Watt, *Multiple-spot optical tweezers created with microlens arrays fabricated by proton beam writing*, Applied Physics B, **78**, 2004, p. 705-710.
- [79] Z. B. Wang, Wei Guo, A. Pena, D. J. Whitehead, B. S. Luk'yanchuk, Lin. Li, Z. Liu, Y. Zhou, and M. H. Hong, *Laser micro/nano fabrication in glass with tunable-focus particle lens array*, Optics Express, **16**, 2008, pp. 19706-19711.
- [80] Y. Hayasaki, T. Sugimoto, A. Takita and N. Nishida, *Variable holographic femtosecond laser processing by use of a spatial light modulator*, Applied Physics Letters, **87**, 2005, p. 031101-031103.
- [81] S. Hasegawa, Y. Hayasaki and N. Nishida, *Holographic femtosecond laser processing with multiplexed phase Fresnel lenses*, Optics Letters **31**, 2006, p. 1705–1707.
- [82] Y. Kuroiwa, N. Takeshima, Y. Narita, S. Tanaka and K. Hirao, *Arbitrary micropatterning method in femtosecond laser microprocessing using diffractive optical elements*, Optics Express, **12**, 2004, p. 1908–1915.
- [83] H. Takahashi, S. Hasegawa and Y. Hayasaki, *Holographic femtosecond laser processing using optimal-rotation-angle method with compensation of spatial frequency response of liquid crystal spatial light modulator*, Applied Optics, **46**, 2007, p. 5917–5923.
- [84] H. Takahashi, S. Hasegawa, A. Takita and Y. Hayasaki, *Sparse-exposure technique in holographic two-photon polymerization*, Optics Express, **16**, 2008, p. 16592–16599.
- [85] Y. Hayasaki, *Holographic femtosecond laser processing and three-*

- dimensional recording in biological tissues*, Progress In Electromagnetics Research Letters, **2**, 2008, p.115–123.
- [86] S. Hasegawa and Y. Hayasaki, *Holographic femtosecond laser processing with multiplexed phase fresnel lenses displayed on the liquid crystal spatial light modulator*, Optical Review, **14**, 2007, p. 208–213.
- [87] Chaen, K., H. Takahashi, S. Hasegawa, and Y. Hayasaki, “Display method with compensation of the spatial frequency response of a liquid crystal spatial light modulator for holographic femtosecond laser processing, Optics Communications, **280**, 2007, p. 165–172.
- [88] Z. Kuang, W. Perrie, J. Leach, M. Sharp, S. P. Edwardson, M. Padgett, G. Dearden and K. G. Watkins, *High throughput diffractive multi-beam femtosecond laser processing using a spatial light modulator*, Applied Surface Science, **255**, 2008, p. 2284–2289.
- [89] Z. Kuang, D. Liu, W. Perrie, S. P. Edwardson, M. Sharp, E. Fearon, G. Dearden and K. G. Watkins, *Fast parallel diffractive multi-beam femtosecond laser surface micro-structuring*, Applied Surface Science, **255**, 2009, p. 6582-6588.
- [90] Z. Kuang, W. Perrie, D. Liu, S. P. Edwardson, J.Cheng, G. Dearden, K. G. Watkins, *Diffractive multi-beam surface micro-processing using 10 ps laser pulses*, Appl. Surface Science, **255**, 2009, p. 9040-9044.
- [91] D. Liu, Z. Kuang, S. Shang, W. Perrie, D. Karnakis, A. Kearsley, M. Knowles, S. Edwardson, G. Dearden, and K. Watkins, *Ultrafast parallel laser processing of materials for high throughput manufacturing*, Proceedings of LAMP2009 - the 5th International Congress on Laser Advanced Materials Processing, June 29th-July 2009, Kobe, Japan.

- [92] Holoeye LC-R 2500 spatial light modulator (SLM), Official Webpage of Holoeye Company [cited Oct. 2009, Available from: [http://www.holoeye.com/spatial\\_light\\_modulator\\_lc\\_r\\_2500.html](http://www.holoeye.com/spatial_light_modulator_lc_r_2500.html)]
- [93] Hamamatsu X10468 series spatial light modulator (SLM), Official Webpage of Hamamatsu Photonics [cited Oct 2009; Available from: [http://jp.hamamatsu.com/products/other/1013/1010/X10468/index\\_en.html](http://jp.hamamatsu.com/products/other/1013/1010/X10468/index_en.html)]
- [94] Uzi Efron, *Spatial light modulator technology: materials, devices, and applications*, Marcel Dekker, New York, 1995, ISBN 0-8247-9108-8
- [95] Iam-Choon Khoo, *Liquid crystals*, John Wiley & Sons. Inc. 2nd edition, 2007, ISBN 978-0-471-75153-3
- [96] J. B. Chen, and X. Y. Su, *The principles and applications of optical information technology (in Chinese)*, Higher Education Press, 2001.
- [97] *Phase and amplitude modulation properties of the LC-R 2500*, Manual of Holoeye SLM (LC-2500), 2006
- [98] J. Leach, G. Sinclair, P. Jordan, J. Courtial, M.J. Padgett, J. Cooper and Z.J. Laczik, *3D manipulation of particles into crystal structures using holographic optical tweezers*, Optics Express, **12**, 2004, p. 220–226
- [99] G. Sinclair, J. Leach, P. Jordan, G. Gibson, E. Yao, Z. Laczik, M. Padgett and J. Courtial, *Interactive application in holographic optical tweezers of a multi-plane Gerchberg–Saxton algorithm for three-dimensional light shaping*, Optics Express, **12**, 2004, p. 1665–1670.
- [100] G. Whyte, G. Gibson, J. Leach and M. Padgett, *An optical trapped microhand for manipulating micron-sized objects*, Optics Express **14**, 2006, p. 12497–12502.
- [101] M. Reicherter, S. Zwick, T. Haist, C. Kohler, H. Tiziani and W. Osten, *Fast*

- digital hologram generation and adaptive force measurement in liquid-crystal-display-based holographic tweezers*, *Applied Optics*, **45**, 2006, p. 888–896.
- [102] J. Leach, K. Wulff, G. Sinclair, P. Jordan, J. Courtial, L. Thomson, G. Gibson, K. Karunwi, J. Cooper, Z.J. Laczik and M. Padgett, *Interactive approach to optical tweezers control*, *Applied Optics*, **45**, 2006, p. 897–903.
- [103] J. Liesener, M. Reicherter, T. Haist and H.J. Tiziani, *Multi-functional optical tweezers using computer-generated holograms*, *Optics Communications*, **185**, 2000, p. 77–82.
- [104] G. Gibson, D. M. Carberry, G. Whyte, J. Leach, J. Courtial, J. C. Jackson, D. Robert, M. Miles and M. Padgett, *Holographic assembly workstation for optical manipulation*, *Journal of Optics A: Pure and Applied Optics*, **10**, 2008, 044009
- [105] J. A. Grieve, A. Ulcinas, S. Subramanian, G. M. Gibson, M. J. Padgett, D. M. Carberry, and M. J. Miles, *Hands-on with optical tweezers: a multitouch interface for holographic optical trapping*, *Optics Express*, **17**, 2009, pp. 3595-3602.
- [106] P. Jordan, J. Leach, M. Padgett, P. Blackburn, N. Isaacs, M. Goksor, D. Hanstorp, A. Wright, J. Girkin, and J. Cooper, *Creating permanent 3D arrangements of isolated cells using holographic optical tweezers*, *Lab on a Chip*, **5**, 2005, p. 1224-1228.
- [107] M. Reicherter, T. Haist, E. U. Wagemann, and H. J. Tiziani, *Optical particle trapping with computer-generated holograms written on a liquid-crystal display*, *Optics Letters*, **24**, 1999, p. 608-610
- [108] Astrid van der Horst and Nancy R. Forde, *Calibration of dynamic*

- holographic optical tweezers for force measurements on biomaterials*, Optics Express, **16**, 2008, p. 20987-21003
- [109] P. C. Mogensen and J. Glückstad, *Dynamic array generation and pattern formation for optical tweezers*, Optics Communications, **175**, 2000, p. 75-81
- [110] G. Sinclair, P. Jordan, J. Leach, M. J. Padgett and J. Cooper, Defining the trapping limits of holographical optical tweezers, Journal of Modern Optics, **51**, 2002, p. 409-414
- [111] H. Melville, G. Milne, G. Spalding, W. Sibbett, K. Dholakia, and D. McGloin, Optical trapping of three-dimensional structures using dynamic holograms, Optics Express, **11**, 2003, p. 3562-3567.
- [112] J. E. Curtis, B. A. Koss and D. G. Grier, *Dynamic holographic optical tweezers*, Optics Communications, **207**, 2002, p. 169-175.
- [113] David G. Grier, *A revolution in optical manipulation*, Nature, **424**, 2003, p. 810-816
- [114] Ota Samek, Vanja Hommes, Roland Hergenröder, and Sergei V. Kukhlevsky, *Femtosecond pulse shaping using a liquid-crystal display: Applications to depth profiling analysis*, Review of scientific instruments, **76**, 2005, p. 086104
- [115] A. M. Weiner, *Femtosecond pulse shaping using spatial light modulators*, Review of Scientific Instrument. 71, 2000, p. 1929-1960
- [116] T. Haist, E. U. Wagemann, H. J. Tiziani, *Pulsed-laser ablation using dynamic computer-generated holograms written into a liquid crystal display*, Journal of Optics A: Pure and Applied Optics, **1** (3), 1999, p. 428-430

- [117] R. W. Gerchberg and W. O. Saxton, *A practical algorithm for the determination of the phase from image and diffraction plane pictures*, *Optik*, **35**, 1972, p. 237-246.
- [118] J.E. Curtis, C.H.J. Schmitz and J.P. Spatz, *Symmetry dependence of holograms for optical trapping*, *Optics Letters*, **30**, 2005, p. 2086–2088
- [119] Figure 2.5.1 was modified from a picture file named GS-diagram.png. The file was available at: <http://upload.wikimedia.org/wikipedia/en/c/c2/GS-diagram.png>, Oct. 2009
- [120] T. Haist, M. Schönleber and H. J. Tiziani, *Computer-generated holograms from 3D-objects written on twisted*
- [121] *CPA-2010 user manual*, Version 1.2, Clark-MXR, Inc, 2001
- [122] K. R. Tamura, *Additive pulse mode locking erbium doped fiber lasers*, Massachusetts: MIT, PhD thesis, 1994
- [123] *X10468 series SLM technical information*, Hamamatsu photonics, 2008
- [124] ZEMAX: software for optical system design, Official webpage of ZEMAX [cited Oct. 2009; Available at: <http://www.zemax.com/>]
- [125] GSI scanning galvanometer systems, Official webpage of GSI Group [cited Oct. 2009; Available at: <http://www.gsig.com/scanners/>]
- [126] NUTFIELD scanning galvanometer systems, Official webpage of NUTFIELD TECHNOLOGY [cited Oct. 2009; Available at: <http://www.nutfieldtech.com/nutfield/scanheads.asp>]
- [127] SCAPS scanner application software, Official webpage of SCAPS [cited Oct. 2009; Available at: <http://www.scaps.com/products/samlight.php>]
- [128] WINLASE Professional Laser Marking Software, Official webpage of LANMARK CONTROLS [cited Oct. 2009; Available at:

[http://www.lanmarkcontrols.com/software\\_pro.htm](http://www.lanmarkcontrols.com/software_pro.htm)]

- [129] AEROTECH motion control system, Official webpage of AEROTECH [cited Oct. 2009: Available at <http://www.aerotech.com/>]
- [130] VEECO, Official webpage of VEECO: [cited Oct. 2009: Available at <http://www.veeco.com/> ]
- [131] J. Amako, K. Nagasaka, K. Nishida, *Chromatic-distortion compensation in splitting and focusing of femtosecond pulses by use of pair of diffractive optical elements*, Optics Letter 27, 2002, p. 969-971.
- [132] M. Barberoglou, V. Zorba, E. Stratakis, E. Spanakis, P. Tzanetakis, S.H. Anastasiadis, and C. Fotakis, *Bio-inspired water repellent surfaces produced by ultrafast laser structuring of silicon*, Applied Surface Science, **255**, 2009, p. 5425-5429
- [133] Ralf Blossey, *Self-cleaning surfaces - virtual realities*, Nature Materials, **2**, 2003, p. 301-306
- [134] M. Callies and D. Quere, *On water repellency*, Soft Matter, **1**, 2005, p. 55-61
- [135] A. Nakajima, A. Fujishima, K. Hashimoto and T. Watanabe, *Preparation of Transparent Superhydrophobic Boehmite and Silica Films by Sublimation of Aluminum Acetylacetonate*, Advanced Materials. **11** (1999), p. 1365
- [136] J.-Y. Shiu, C.-W. Kuo, P. Chen and C.-Y. Mou, *Fabrication of Tunable Superhydrophobic Surfaces by Nanosphere Lithography*, Chemistry of Materials, **16** (2004), p. 561-564
- [137] P.N. Bartlett, J.J. Baumberg, P.R. Birkin, M.A. Ghanem and M.C. Netti, *Highly Ordered Macroporous Gold and Platinum Films Formed by Electrochemical Deposition through Templates Assembled from Submicron*

- Diameter Monodisperse Polystyrene Spheres*, Chemistry of Materials, **14** (2002), p. 2199-2208
- [138] I. Woodward, W.C.E. Schofield, V. Roucoules and J.P.S. Badyal, *Superhydrophobic Surfaces Produced by Plasma Fluorination of Polybutadiene Films*, Langmuir, **19** (2003), p. 3432-3438
- [139] E. Martines, K. Seunarine, H. Morgan, N. Gadegaard, C.D.W. Wilkinson and M.O. Riehle, *Superhydrophobicity and Superhydrophilicity of Regular Nanopatterns*, Nano Letters. **5** (2005), p. 2097-3103
- [140] K.K.S. Lau, J. Bico, K.B.K. Teo, M. Chhowalla, G.A.J. Amaratunga, W.I. Milne, G.H. McKinley and K.K. Gleason, *Superhydrophobic Carbon Nanotube Forests*, Nano Letters. **3** (2003), p. 1701-1705
- [141] V. Zorba, P. Tzanetakis, C. Fotakis, E. Spanakis, E. Stratakis, D.G. Papazoglou and I. Zergioti, *Silicon electron emitters fabricated by ultraviolet laser pulses*, Applied Physics Letters, **88** (2006), p. 081103-081105
- [142] T.-H. Her, R.J. Finlay, C. Wu, S. Deliwala and E. Mazur, *Microstructuring of silicon with femtosecond laser pulses*, Applied Physics Letters, **73** (1998), p. 1673-1675
- [143] S. R. Forrest, *The path to ubiquitous and low-cost organic electronic appliances on plastic*, Nature, **428**, 2004, p. 911-918.
- [144] C. Liu, G. Zhu, D. Liu, *Patterning cathode for organic light-emitting diode by pulsed laser ablation*, Displays, **29**, 2008, p. 536-540.
- [145] P. J. Scully, D. Jones and D. A. Jaroszynski, *Femtosecond laser irradiation of polymethyl methacrylate for refractive index gratings*, Journal of Optics A, **5**, 2003, p. S92-S96.

- [146] A. Baum, P. J. Scully, W. Perrie, D. Jones, R. Issac, and D. A. Jaroszynski, *Pulse-duration dependency of femtosecond laser refractive index modification in poly(methyl methacrylate)*, Optics Letters, **33**, 2008, p. 651-653.
- [147] A. Baum, P. J. Scully, M. Basanta, C. L. Paul Thomas, P. R. Fielden, N. J. Goddard, W. Perrie, and P. R. Chalker, *Photochemistry of refractive index structures in poly(methyl methacrylate) by femtosecond laser irradiation*, Optics Letters, **32**, 2007, p. 190-692.
- [148] H. Kogelnik, *Coupled wave theory for thick hologram grating*, Bell System Technical Journal, **48**, 1969, p. 2909.
- [149] Z. Kuang, D. Liu, W. Perrie, J. Cheng, S. Shang, S. P. Edwardson, E. Fearon, G. Dearden, K. G. Watkins, *Diffractive Multi-beam Ultra-fast Laser Micro-processing Using a Spatial Light Modulator* (Invited Paper), Chinese Journal of Lasers, 2009, Vol. 36, No. 12, pp. 3093 – 3115.